Time-lapse monitoring with virtual seismology

Applications of the Marchenko method for observing time-lapse changes in subsurface reservoirs

van IJsseldijk, J.E.

DOI
10.4233/uuid:98b24420-219b-438e-a28c-4b12e5f450e6

Publication date
2023

Document Version
Final published version

Citation (APA)
van IJsseldijk, J. E. (2023). *Time-lapse monitoring with virtual seismology: Applications of the Marchenko method for observing time-lapse changes in subsurface reservoirs*. [Dissertation (TU Delft), Delft University of Technology]. https://doi.org/10.4233/uuid:98b24420-219b-438e-a28c-4b12e5f450e6

TIME-LAPSE MONITORING WITH VIRTUAL SEISMOLOGY

APPLICATIONS OF THE MARCHENKO METHOD FOR OBSERVING TIME-LAPSE CHANGES IN SUBSURFACE RESERVOIRS

TIME-LAPSE MONITORING WITH VIRTUAL SEISMOLOGY

APPLICATIONS OF THE MARCHENKO METHOD FOR OBSERVING TIME-LAPSE CHANGES IN SUBSURFACE RESERVOIRS

Proefschrift

ter verkrijging van de graad van doctor
aan de Technische Universiteit Delft,
op gezag van de Rector Magnificus Prof. Dr. Ir. T.H.J.J. van der Hagen,
voorzitter van het College voor Promoties,
in het openbaar te verdedigen op
28 September 2023 om 10:00 uur

door

Johno Egbart VAN IJSSELDIJK

Master of Science in Toegepaste Geofysica,
Technische Universiteit Delft, Delft, Nederland,
geboren te Weert, the Netherlands.

Dit proefschrift is goedgekeurd door de promotoren.

Samenstelling promotiecommissie:

Rector Magnificus,	voorzitter
Prof. dr. ir. C.P.A. Wapenaar,	Technische Universiteit Delft, promotor
Prof. dr. ir. E.C. Slob,	Technische Universiteit Delft, promotor
Onafhankelijke leden:	
Prof. dr. A. Curtis,	University of Edinburgh
Dr. H. Douma,	Quantairra R&D Services B.V.
Prof. dr. S. Geiger,	Technische Universiteit Delft
Prof. dr. W.A. Mulder,	Technische Universiteit Delft
Overig lid:	
Dr. H. Hajibeygi,	Technische Universiteit Delft

Dit werk heeft financiële steun gekregen van de European Research Council (ERC) onder het Horizon 2020 onderzoeks en innovatie programma van de Europese Unie (toelage nummer: 742703).

TU Delft
Delft
University of
Technology

erc
European Research Council
Established by the European Commission

Keywords: Marchenko, multiples, time-lapse seismics, reservoir simulation

Front & back: Seismic wavefield focusing after flow in a porous medium

Printed by: Gildeprint

ISBN 978-94-6366-698-5

An electronic version of this dissertation is available at: http://repository.tudelft.nl/.

Voor mijn grootouders, opdat jullie trots op me zijn.
Voor Victor, opdat je je rust gevonden hebt.

CONTENTS

SUMMARY

Monitoring time-lapse changes inside the subsurface is of great significance to many geotechnical applications, such as storage of gasses in underground geological formations. Minute differences in the seismic wavefield between an initial baseline and a subsequent monitor survey have to be detected in order to observe fluid flow inside subsurface reservoirs. This problem becomes even more challenging when the reservoir is situated underneath a series of complex, highly reflective layers. Such an overburden will generate strong multiple reflections that will interfere with the reflections of the target zone. Ideally, a methodology is designed in order to remove these internal multiples to allow a clear view of the reservoir response for time-lapse analysis. The Marchenko method can redatum the seismic wavefield to arbitrary depth levels or points in the subsurface, while accounting for all orders of internal multiple reflections. This method, therefore, has great potential to solve some of the time-lapse issues, as it is able to closely examine specific zones of interest in the subsurface without distortions from surrounding layers.

Time-lapse studies are often hampered by irregular or imperfect sampling, whereas the Marchenko method relies on densely sampled, co-located sources and receivers. It is, therefore, important that the Marchenko method is able to handle more complex acquisition geometries. This can either be achieved by interpolating the reflection data as a pre-processing step or by correcting for errors inside the Marchenko scheme. Here, point-spread functions are introduced that describe the imperfections in the reflection data. These imperfections distort the focusing and Green's functions retrieved from the Marchenko method. Next, each iteration of the Marchenko scheme is extended to deblur the imperfect focusing and Green's functions by multidimensional deconvolution with these point-spread functions. Additionally, a slight modification is required to ensure stability of the new scheme. This new iterative Marchenko scheme is computationally more expensive, but removes all sampling artifacts. Finally, the migrated images of the target zone show significant improvements, when using either the new scheme or interpolation as pre-processing step.

Next, a methodology for the isolation of the reservoir response from the entire seismic response is proposed. This is achieved by applying Marchenko twice, to first remove the overburden reflections followed by removal of the underburden. Consequently, a reflection response that solely consists of the primaries and multiples related to the reservoir is acquired. The isolation can then be applied to both a baseline as well as a monitor study, however the time-lapse traveltime differences still contain the effects of the overburden time-lapse changes. In order to remove these effects a reference reflection above the reservoir can be selected, which is correlated with an event below the reservoir to acquire the timelag between the reflection above and the event below the reservoir. These time-lags are first computed for both time-lapse studies, and then correlated with each other to find reservoir specific time-lapse traveltime changes. Traveltime differences can be calculated both for primary reflections as well as for multiples. The advantage of the latter is that they probe the reservoir multiple times, and are, therefore, more sensitive to the changes in velocity. On the contrary, a disadvantage is that they are weaker in amplitude, thus harder to observe. However, their amplitudes can be artificially enhanced by manipulating the focusing functions used in the final step of the Marchenko-based target-zone isolation. Finally, it is concluded that the Marchenko-based isolation leads to improved time-lapse interpretation, and that the internal multiples provide additional, complementary information.

Next, it is important to relate the time-lapse changes of the seismic responses to changes of reservoir parameters (such as porosity and fluid saturation), in order to test the method on realistic scenarios. For this purpose, a multiphase poromechanical reservoir simulator is designed and connected to the seismic modeler. This simulator computes the pressure, saturation and displacement in the subsurface. The changes in the dynamic reservoir properties are then translated to seismic velocity and density via fluid substitution, to provide more realistic, synthetic models, which are used to test the isolation and subsequent traveltime extraction methodology once more. Again, the difference between the results with and without overburden removal is notably significant, highlighting the importance of the isolation for time-lapse analysis.

Finally, the proposed methodology is tested on a marine dataset. The application of the Marchenko method to field data is somewhat complicated. Especially, the strict requirement on the amplitude scaling of the reflection response tends to be a tough barrier to overcome. Scaling factors can be found by minimizing the energy of the internal multiples in the retrieved Green's functions, while still ensuring convergence of the Marchenko scheme. Furthermore, an approximate velocity model is used to calculate the two-way traveltimes between the surface and the focal depths. After all requirements are met, the reservoir response is isolated from the reflection response of the baseline and monitor surveys. Initially, only traveltime differences from a primary are extracted, because the multiples appear outside the recording time. However, the internal multiples can be reconstructed with the focusing functions by carefully selecting the focal depth. Once more, the retrieved traveltime differences from the primary event below the reservoir are confirmed and complemented by the reconstructed multiples.

This work shows that time-lapse analysis can benefit from the Marchenko method. The methodology devised in this thesis is not only able to clarify the response of a specific target, it also shows the added value that internal multiples can provide. Ultimately, this opens the door for more time-lapse applications of the Marchenko method, and improved interpretation of time-lapse changes in the subsurface.

SAMENVATTING

Het monitoren van veranderingen in de ondergrond over tijd is van groot belang voor veel geotechnische toepassingen, zoals het ondergronds opslaan van gassen in geologische formaties. Minieme verschillen in het seismisch golfveld tussen een initiële basislijn- en een daaropvolgende monitor studie, moeten gedetecteerd worden om vloeistofstroming in ondergrondse reservoirs waar te nemen. Dit probleem is nog uitdagender wanneer het reservoir zich onder een serie van complexe, sterk reflecterende lagen bevindt. Dergelijke bovenlagen zullen sterke reflecties veroorzaken, die met de reflecties uit de doellaag interfereren. Idealiter wordt een methode ontworpen om deze interne meervoudige reflecties te verwijderen, zodat een duidelijk beeld van de respons van het reservoir ontstaat voor de analyse van het tijdsafhankelijk gedrag. De Marchenko-methode kan het seismische golfveld verplaatsen naar willekeurge diepteniveaus of punten in de ondergrond, rekeninghoudende met alle orden van meervoudige reflecties. Hierdoor is er grote potentie om met deze methode sommige problemen met betrekking tot het seismisch meten van verandering over een bepaald tijdsverloop op te lossen. Immers, de methode is in staat om specifieke lagen van interesse nauwkeurig te onderzoeken zonder verstoringen van de omringende lagen.

Seismische tijdsafhankelijke onderzoeken worden vaak gehinderd door onregelmatige of imperfecte locaties van de meetpunten, terwijl de Marchenko-methode berust op een dichte bemonstering van, op dezelfde locatie geplaatste, bronnen en ontvangers. Daarom is het belangrijk dat de Marchenko-methode in staat is om complexere acquisitiegeometrieën te gebruiken. Dit kan zowel bereikt worden door de data te interpoleren voor toepassing van de Marchenko-methode of door de fouten van de onregelmatige geometrie te corrigeren binnen het Marchenko-schema. Hier introduceren we puntverspreidings-functies, die deze geometrische imperfecties in de reflectie data beschrijven. Deze imperfecties verstoren de, uit het Marchenko-schema verkregen, focuserings en Greense functies. Vervolgens wordt iedere iteratie uit het Marchenko-schema uitgebreid om voor de imperfecties in de focuserings en Greense functies te corrigeren door te deconvolueren met de puntverspreidings-functies. Daarnaast, is een kleine aanpassing nodig om de stabiliteit van het nieuwe schema te waarborgen. Dit nieuwe, iteratieve Marchenko-schema is computationeel duurder, maar verwijdert alle bemonsteringsartefacten. Ten slotte laten de gemigreerde afbeeldingen van het doelgebied aanzienlijke verbeteringen zien, zowel wanneer het nieuwe schema gebruikt wordt als ook wanneer de reflectie data eerst geïnterpoleerd wordt.

Hierna wordt een methodologie voorgesteld om de respons van het reservoir te isoleren van de gehele seismische respons. Dit wordt bereikt door de Marchenko-methode twee keer toe te passen, eerst om de bovenliggende lagen te verwijderen, gevolgd door een verwijdering van de onderliggende lagen. De resultererende reflectie respons bestaat alleen maar uit de primaire en meervoudige reflecties van het reservoir. De isolatie kan toegepast worden zowel op een basislijn- als op de monitor studies, maar de verkregen tijdverschillen bevatten nog altijd de tijdseffecten van de bovenliggende lagen. Om deze effecten te verwijderen wordt een referentie reflectie boven het reservoir geselecteerd. Deze reflectie wordt dan gecorreleerd met een aankomst van onder het reservoir om de reistijd tussen de twee reflecties onder en boven het reservoir te verkrijgen. Deze reistijden worden eerst berekend voor beide tijdsafhankelijke studies en vervolgens met elkaar gecorreleerd om de specificieke tijdverschillen in het reservoir te vinden. Deze tijdverschillen kunnen berekend worden voor zowel de primaire als meervoudige reflecties. Het voordeel van laatstgenoemde is dat ze het reservoir meerdere keren bemonsteren en dus gevoeliger zijn voor snelheidsverschillen. Een nadeel is daarentegen dat ze een zwakkere amplitude hebben en dus moeilijker waarneembaar zijn. Hun amplitudes kunnen echter kunstmatig versterkt worden door de focuserings functies te manipuleren in de laatste stap van de voorgestelde isolatie van het reservoir. Tot slot, wordt er geconcludeerd dat de op Marchenko-methode gebaseerde isolatie leidt tot verbeterde tijdsafhankelijke interpretatie van het reservoir en dat de meervoudige interne reflecties aanvullende, complementaire informatie verschaffen.

Vervolgens is het belangrijk om de tijdsafhankelijke veranderingen in de seismische respons te relateren aan veranderingen van de reservoir eigenschappen (zoals porositeit en vloeistof saturatie), om zo meer realistische scenarios te testen met de methode. Hiervoor wordt een meerdere-fase, poromechanische simulator ontworpen en gekoppeld aan een seismische simulator. Deze simulator berekent de druk, saturatie en verplaatsing in de ondergrond. De veranderingen in de dynamische reservoir eigenschappen worden dan vertaald naar seismische snelheden en dichtheden via vloeistofvervanging, om meer realistische, seismische modellen te verschaffen, die gebruikt kunnen worden om de isolatie en daaropvolgende extractie methodologie van het tijdsafhankelijke gedrag nogmaals te testen. Opnieuw is het verschil tussen de resultaten met en zonder verwijdering van de bovenliggende lagen bijzonder significant, wat het belang van de isolatie voor de analyse van het tijdsafhankelijke gedrag nogmaals benadrukt.

Ten slotte wordt de voorgestelde methodologie getest op een mariene dataset. De toepassing van de Marchenko-methode op velddata is enigszins gecompliceerd. In het bijzonder, is de strikte eis aan de amplitude schaling van de reflectie respons een ingewikkelde horde om te nemen. Schalingsfactoren kunnen gevonden worden door de energie van de interne meervoudige reflecties in de verkregen Greense functies te minimalizeren, ervoor zorgende dat het Marchenko-schema nog steeds convergeert. Verder wordt een benadering van het snelheidsmodel gebruikt om de twee-weg tijden tussen het aardoppervlak en de focale diepte te berekenen. Nadat aan alle vereisten is voldaan, is de reservoir respons geïsoleerd in de seismische respons voor zowel de basislijn- als monitor studies. In eerste instantie worden alleen tijdsverschillen uit een primaire reflectie gehaald, omdat de meervoudige reflecties buiten de opgenomen tijd vallen. De interne meervoudige reflecties kunnen echter gereconstueerd worden met focuserings functies door de focale diepte zorgvuldig te selecteren. Wederom worden de gevonden tijdsverschillen van de primaire reflectie onder het reservoir bevestigd en aangevuld met de gereconstueerde meervoudige reflecties.

Dit werk laat zien dat seismische tijdsafhankelijke analyse kan profiteren van de Marchenko-methode. De methodologie die in dit proefschrift is ontworpen, is niet alleen in staat de respons van een specifieke doellaag te verduidelijken, maar het toont ook de toegevoegde waarde van de interne meervoudige reflecties. Hierdoor wordt uiteindelijk de deur geopend naar meer toepassingen van de Marchenko-methode voor studies naar tijdsafhankelijk gedrag en een betere interpretatie van veranderingen over tijd in de ondergrond.

1

INTRODUCTION

Combatting climate change is becoming increasingly important and urgent as nations world-wide are shifting from fossil fuels towards renewable energy sources, and aim for a carbon-neutral economy in the near future. The subsurface plays an essential role in this energy transition and the mitigation of climate change (IPCC, 2014); not only does it contain crucial mineral and thermal resources, but it also allows for storage of gasses in the pore space of geological formations. These underground reservoirs can be used for sequestration of CO_2 (Bui et al., 2018), or temporary, large-scale storage of green gasses such as hydrogen (Krevor et al., 2023). In order to ensure the efficiency and safety of these developments, it is imperative to have a good understanding of the properties as well as fluid flow inside subsurface reservoirs. For this purpose, geophysical methods can be used to derive and monitor the structure and properties of the subsurface.

These geophysical methods rely on the fact that different geological layers have different physical properties, hence these layers will respond differently to signals that are emitted into the subsurface. Next, these responses are measured and inverted to find the parameters and structure related to the various layers of the subsurface. One example of a geophysical method that is widely used to examine the earth is reflection seismology, which depends on sound waves to delineate the boundaries between geological layers. Active seismic surveys use a source, such as airguns, dynamite or specialized vibrators, to emit waves into the earth. These waves propagate until a boundary between two layers is encountered, where part of the waves will be reflected back to the surface and another part transmitted into the next layer. Once the reflected waves reach the earth's surface, they can be detected using geophones, which measure vibrations akin to how a microphone records sound. Finally, the data, recorded by the geophones, are inverted to resolve the geological structure of the subsurface.

Such experiments, however, only provide information at a single moment in time, whereas the situation in the reservoir will change over time due to fluid injection or production. To predict the fluid flow, simulators are designed that forecast the dynamic reservoir properties, like pressure and saturation (Peaceman, 2000). The dynamic changes in the reservoir can only be detected when multiple seismic surveys are acquired at different times over the same target. A so-called baseline survey can then be used as a reference, and be compared to monitor surveys at later times (Landrø, 2001; Lumley, 2001). Detecting time-lapse changes from two surveys is challenging, as minute changes have to be observed against the background noise of the seismic surveys. This is known as the issue of 4D repeatability, which asserts that deviations in the geometry of the seismic surveys will decrease the signal-to-noise ratio (SNR) of the time-lapse results (Smit et al., 2005).

Another reason why monitoring subsurface fluid flow can be complicated is that reservoirs are oftentimes overlain with a salt layer. On the one hand, such layers provide great sealing qualities, which effectively prevent the fluids to escape the reservoir below. On the other hand, the salt structures are usually complex and characterized by high seismic velocities (Jackson & Hudec, 2017). This high contrast in velocity with the surrounding layers can trap the seismic wavefield inside the salt layer, which then generates strong internal multiples. Internal multiples are seismic reflections that were reflected in the surface more than once. Most seismic methods use a single-scattering approximation that will interpret these multiples as primary reflections, in other words they assume that they belong to a unique layer in the subsurface. Consequently, the target response of a reservoir can be obstructed by the existence of internal multiples originating from the overlaying layers.

1.1. THE MARCHENKO METHOD

Recently, the Marchenko equations were developed into a data-driven seismic method that accounts for all orders of multiples (Broggini et al., 2012; Slob et al., 2014; Wapenaar et al., 2014). The method can be used for seismic imaging (Wapenaar et al., 2014), multiple elimination (Zhang & Staring, 2018), homogeneous Green's function retrieval (Brackenhoff et al., 2019), and wavefield redatuming (Staring et al., 2018). Figure 1.1 displays the principle of this method. At the base of the method are the focusing functions, defined in a truncated medium (or subsurface) that is the same as the actual medium above the focal depth, but homogeneous below this depth. When the downgoing focusing function is injected into this truncated medium, only the upgoing focusing function is retrieved at the surface (1.1A). This is due to the fact that no reflections are created below the focal depth. Next, the downgoing focusing function is injected into the actual medium. Again, the first part of the retrieved response is the upgoing focusing functions, but this time there is also the upgoing response from a downward radiating virtual source at the focal depth (1.1B). This response is known as the Green's function, which is the impulse response due to a virtual source at the focal point of the medium. Finally, injecting a time-reversed version of the upgoing focusing functions into the medium yields the responses of the (time-reversed) downgoing focusing function and the upgoing Green's function due to an upward radiating virtual source (1.1C).

Figure 1.1A and B can be combined into "equation form" to find the coupled Marchenko equations. In order to solve these equations no prior knowledge of the subsurface is required, except for an estimation of the traveltime of the direct arrival between the focal point and the surface. Such an estimation can, for example, be computed inside a smooth version of the medium, and is used as an initial approximation for the downgoing focusing function. The focusing functions can then be updated either iteratively

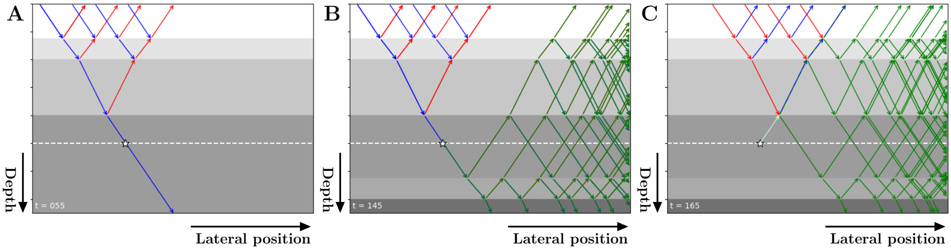

Figure 1.1: In A the downgoing focusing function (blue) is injected into the truncated medium, with a focal depth indicated with the dashed white line. The reflected rays (red) are the upgoing focusing function. B and C shows the injection of the downgoing and time-reversed upgoing focusing function in the actual medium, respectively, which create a virtual source at the focal depth. The resulting Green's functions (green) are separable in time from the focusing functions. An animated version of this figure is available online: https://tinyurl.com/VirtualSeismology.

(Thorbecke et al., 2017) or by direct inversion (van der Neut et al., 2015). Lastly, the focusing functions are used to find the decomposed Green's functions, which effectively represent how the physical sources at the earth's surface have been redatumed to an arbitrary focal depth. Subsequently, the retrieved Green's functions can be used to also redatum the receivers at the surface to the focal depth (Wapenaar, 1996). The ability to redatum the wavefield inside the subsurface opens the door for more detailed imaging and analysis of specific targets (Ravasi et al., 2016; Shoja et al., 2022; Wapenaar & Staring, 2018).

1.2. AIM AND OUTLINE OF THE THESIS

An increasing demand for subsurface storage of gasses, combined with an added complexity due to cyclic processes induced by temporary storage calls for a better understanding and monitoring of underground reservoirs. The seismic response of such reservoirs can often be hidden behind a convoluted wavefield of multiples generated by interbeds or salt layers in the overburden. Recent advancements to the Marchenko method have shown promise to remove or suppress these multiple interactions on field data (Brackenhoff et al., 2019; Ravasi et al., 2016; Staring et al., 2018). This raises the question of whether the Marchenko method can be used to improve time-lapse seismic surveys, especially in cases where strong internal multiples are present in the data. This thesis aims to answer this question and find possible time-lapse applications for the Marchenko method. The outline of this thesis is as follows:

- Chapter 2: Adaptation of the iterative Marchenko scheme for imperfectly sampled data.

  One of the limitations of the Marchenko scheme is that it requires data on a regular grid of collocated sources and receivers, whereas repeatability of time-lapse surveys is inherently difficult. Hence, this chapter considers a modified version of the iterative Marchenko scheme that is able to utilize irregularly sampled reflection data. This new methodology uses point-spread functions to deblur the focusing and Green's function. However, it can lead to unstable solutions in the even iterations of the Marchenko scheme. In order to avoid these instabilities a full wavefield scheme is introduced that guarantees convergence, but is computationally more expensive. The results of applying the newly developed scheme are then compared to results where reconstruction is realized with a pre-processing step.

- Chapter 3: Extracting small time-lapse traveltime changes in a reservoir after Marchenko-based isolation.
  While the Chapter 2 shows how the Marchenko scheme can be adapted to be more widely used in time-lapse surveys, the question on how to extract time-lapse information from the data remains. For this reason, a method to observe minute time-lapse traveltime changes in a reservoir is presented here. First, the reservoir response is isolated from the full reflection response by means of Marchenko redatuming. This two-fold strategy removes first the overburden and then the underburden in both a baseline and monitor survey. Time-lags between reflections below the reservoir and a reference reflection above are computed. Subsequently, the traveltime differences inside the reservoir are extracted by correlating time-lags between the baseline and monitor study. Improved resolution can be achieved by including internal multiples that traverse the reservoir more than once.

- Chapter 4: A framework for subsurface monitoring by integrating reservoir simulation with time-lapse seismic surveys.
  To assess whether the methodology in Chapter 3 is able to realistically resolve underground flow in reservoirs, the actual time-lapse changes in the subsurface need to be predicted from reservoir simulations. In this chapter, a multi-phase poromechanics simulator is designed, and integrated with the time-lapse methodology. Not only are the time-lapse variations inside the reservoir simulated, but also changes in the over- and underburden due to geomechanical processes. The framework is then tested on a simple model with relatively low scattering as well as a more complex model with higher heterogeneity and impedance contrasts.

- Chapter 5: Time-lapse applications of the Marchenko method on the Troll field.
  While the time-lapse methodology introduced in chapter 3 has been shown to work on synthetic data, application of the Marchenko method to field data tends to be more complicated. This chapter, therefore, evaluates the new methodology on a marine time-lapse dataset of the Troll field in Norway. In addition to clarifying the primary reflections of the reservoir, the method is also able to recreate multiple reflections that arrive after the seismic recording time.

- Chapter 6: Conclusions and recommendations.
  The final chapter will summarize the results, and provide general conclusions about the research presented in this thesis. Additionally, the recommended direction of future research is discussed by having a closer look at the remaining limitations and shortcomings of the method.

- Appendix A: Application of virtual seismology to DAS and geophone data in Groningen.
  In this appendix, the application of virtual seismology is investigated on a seismic survey that use optical fibers with a laser interrogator to record the seismic response. In particular, it analyses the challenging issues of surface-waves removal in land data and scaling corrections of the reflection data.

- Appendix B: Derivation of key equations from reciprocity theorems.
  The final appendix derives some of the fundamental equations of the thesis. By starting from the one-way reciprocity theorems the regular Marchenko representations are derived, which can then be used to find the extrapolated representations. The same reciprocity theorems are then used to deduce how to retrieve reflections responses free from over- or underburden interactions with the newly acquired focusing- and Green's functions.

REFERENCES

Brackenhoff, J., Thorbecke, J., & Wapenaar, K. (2019). Virtual sources and receivers in the real earth: Considerations for practical applications. *Journal of Geophysical Research: Solid Earth*, *124*(11), 11802–11821. https://doi.org/10.1029/2019JB018485

Broggini, F., Snieder, R., & Wapenaar, K. (2012). Focusing the wavefield inside an unknown 1D medium: Beyond seismic interferometry. *Geophysics*, *77*(5), A25–A28. https://doi.org/10.1190/geo2012-0060.1

Bui, M., Adjiman, C. S., Bardow, A., Anthony, E. J., Boston, A., Brown, S., Fennell, P. S., Fuss, S., Galindo, A., Hackett, L. A., Hallett, J. P., Herzog, H. J., Jackson, G., Kemper, J., Krevor, S., Maitland, G. C., Matuszewski, M., Metcalfe, I. S., Petit, C., … Mac Dowell, N. (2018). Carbon capture and storage (CCS): The way forward. *Energy & Environmental Science*, *11*, 1062–1176. https://doi.org/10.1039/C7EE02342A

IPCC. (2014). Mitigation of climate change. Contribution of working group III to the fifth assessment report of the intergovernmental panel on climate change. *Cambridge University Press, Cambridge, United Kingdom and New York, NY, USA*. https://doi.org/10.1017/CBO9781107415416

Jackson, M. P. A., & Hudec, M. R. (2017). Seismic interpretation of salt structures. In *Salt tectonics: Principles and practice* (pp. 364–398). Cambridge University Press. https://doi.org/10.1017/9781139003988.018

Krevor, S., de Coninck, H., Gasda, S. E., Ghaleigh, N. S., de Gooyert, V., Hajibeygi, H., Juanes, R., Neufeld, J., Roberts, J. J., & Swennenhuis, F. (2023). Subsurface carbon dioxide and hydrogen storage for a sustainable energy future. *Nature Reviews Earth & Environment*, 1–17. https://doi.org/10.1038/s43017-022-00376-8

Landrø, M. (2001). Discrimination between pressure and fluid saturation changes from time-lapse seismic data. *Geophysics*, *66*(3), 836–844. https://doi.org/10.1190/1.1444973

Lumley, D. E. (2001). Time-lapse seismic reservoir monitoring. *Geophysics*, *66*(1), 50–53. https://doi.org/10.1190/1.1444921

Peaceman, D. W. (2000). *Fundamentals of numerical reservoir simulation*. Elsevier.

Ravasi, M., Vasconcelos, I., Kritski, A., Curtis, A., da Costa Filho, C. A., & Meles, G. A. (2016). Target-oriented Marchenko imaging of a North Sea field. *Geophysical Journal International*, *205*(1), 99–104. https://doi.org/10.1093/gji/ggv528

Shoja, A., van der Neut, J., & Wapenaar, K. (2022). Target-oriented least-squares reverse-time migration using Marchenko double-focusing: reducing the artefacts caused by overburden multiples. *Geophysical Journal International*, *233*(1), 13–32. https://doi.org/10.1093/gji/ggac438

Slob, E., Wapenaar, K., Broggini, F., & Snieder, R. (2014). Seismic reflector imaging using internal multiples with Marchenko-type equations. *Geophysics*, *79*(2), S63–S76. https://doi.org/10.1190/geo2013-0095.1

Smit, F., Brain, J., & Watt, K. (2005). Repeatability monitoring during marine 4D streamer acquisition. *67th EAGE Conference and Exhibition 2005*. https://doi.org/10.3997/2214-4609-pdb.1.C015

Staring, M., Pereira, R., Douma, H., van der Neut, J., & Wapenaar, K. (2018). Source-receiver Marchenko redatuming on field data using an adaptive double-focusing method. *Geophysics*, *83*(6), S579–S590. https://doi.org/10.1190/geo2017-0796.1

Thorbecke, J., Slob, E., Brackenhoff, J., van der Neut, J., & Wapenaar, K. (2017). Implementation of the Marchenko method. *Geophysics*, *82*(6), WB29–WB45. https://doi.org/10.1190/GEO2017-0108.1

van der Neut, J., Thorbecke, J., Wapenaar, K., & Slob, E. (2015). Inversion of the multidimensional Marchenko equation. *77th EAGE Conference and Exhibition 2015, 2015*. https://doi.org/10.3997/2214-4609.201412939

Wapenaar, C. P. A. (1996). One-way representations of seismic data. *Geophysical Journal International*, *127*(1), 178–188. https://doi.org/10.1111/j.1365-246X.1996.tb01543.x

Wapenaar, K., & Staring, M. (2018). Marchenko-based target replacement, accounting for all orders of multiple reflections. *Journal of Geophysical Research: Solid Earth*, *123*(6), 4942–4964. https://doi.org/10.1029/2017JB015208

Wapenaar, K., Thorbecke, J., van der Neut, J., Broggini, F., Slob, E., & Snieder, R. (2014). Marchenko imaging. *Geophysics*, *79*(3), WA39–WA57. https://doi.org/10.1190/geo2013-0302.1

Zhang, L., & Staring, M. (2018). Marchenko scheme based internal multiple reflection elimination in acoustic wavefield. *Journal of Applied Geophysics*, *159*, 429–433. https://doi.org/10.1016/j.jappgeo.2018.09.024

2

ADAPTATION OF THE ITERATIVE MARCHENKO SCHEME FOR IMPERFECTLY SAMPLED DATA

The Marchenko method retrieves the responses to virtual sources in the Earth's subsurface from reflection data at the surface, accounting for all orders of multiple reflections. The method is based on two integral representations for focusing- and Green's functions. In discretized form, these integrals are represented by finite summations over the acquisition geometry. Consequently, the method requires ideal geometries of regularly sampled and co-located sources and receivers. Recently new representations were derived, which handle imperfectly sampled data. These new representations use point-spread functions (PSFs) that reconstruct results as if they were acquired using a perfect geometry. Here, the iterative Marchenko scheme is adapted, using these new representations, to account for imperfect sampling. This new methodology is tested on a 2D numerical data example. The results show clear improvement of the proposed scheme over the standard iterative scheme. By removing the requirement for perfect geometries, the Marchenko method can be more widely applied to field data.

This chapter was published as van IJsseldijk, J., & Wapenaar, K. (2021). Adaptation of the iterative Marchenko scheme for imperfectly sampled data. *Geophysical Journal International*, *224*(1), 326–336. https://doi.org/10.1093/gji/ggaa463

Minor modifications have been applied to keep consistency within this thesis.

2.1. INTRODUCTION

Seismic surveys are generally concerned with targets in the Earth's subsurface. However, structures in the overburden can distort the response of deeper targets. Ideally, all overburden structures and their multiple reflections should entirely be removed from the data, leaving only the response of the desired deeper targets. This can be achieved by redatuming the reflection response measured at the surface to a new datum plane below the overburden. The data-driven Marchenko method allows for the placement of virtual sources anywhere inside the subsurface, while accounting for all orders of multiples of the overburden (Broggini et al., 2012; Slob et al., 2014; Wapenaar et al., 2014). Thereafter, the receivers can be moved to the same datum plane by a multidimensional deconvolution. Thus, Marchenko redatuming effectively shifts the response from the surface to a new datum inside the medium, and fully removes all interactions with the shallower structures.

Although the method has been successfully applied to real data (e.g. Ravasi et al., 2016; Staring et al., 2018), several constraints still limit the usefulness of the method. Marchenko redatuming is based on two integral representations. These coupled equations can be solved by direct inversion (van der Neut et al., 2015) or by iterative substitution (Thorbecke et al., 2017). In practice, the infinite integrals are replaced by summations over the finite acquisition geometry. This requires regularly sampled and co-located sources and receivers in order to retrieve proper, uncontaminated responses. On the contrary, non-perfect geometries can have a significant effect on the Marchenko results (Peng et al., 2019; Staring & Wapenaar, 2020). Most authors, therefore, assume ideal acquisition geometries when using the Marchenko method, thus avoiding the limitations arising from imperfect sampling. However, this restriction should ideally be relaxed or even removed, allowing for broader application of the method on field data.

Peng and Vasconcelos (2019) consider the effects of different sub-sampling and integration scenarios. Two main effects are identified. First, when the sub-sampling and integration occur over the same dimension, the focusing- and Green's functions get distorted but remain well-sampled. Second, in the situation of sub-sampling and integration over different dimensions, the focusing- and Green's functions are accurate for the non-zero traces but contain spatial gaps. In the case of irregular sampling, the second effect can partly be removed by using a sparse inversion of the Marchenko equations, outputting well-sampled focus functions and sub-sampled Green's functions (Haindl et al., 2018; Ravasi, 2017). On the other hand, Wapenaar and van IJsseldijk (2020) introduce new representations for focusing- and Green's functions, that are distorted by imperfect sampling and integration over the same dimension. Inverting these representations involves a multidimensional deconvolution with novel point-spread functions (PSFs) to deblur the distorted focusing- and Green's functions. These representations are then verified on analytically modeled focusing functions, that have been derived from decomposed wave-field propagators and scattering coefficients. However, in real scenarios these functions are unavailable and have to be derived from the coupled Marchenko equations.

In this chapter we explore how we can integrate the new representations for irregularly sampled data into the iterative Marchenko scheme. First, the theory of deblurring the Marchenko equations with PSFs is reviewed. Next, the chapter discusses the required changes to apply PSFs in the iterative scheme. Then, we present an altered version of the iterative scheme, that allows for imperfectly sampled data. The performance of the newly developed scheme is then tested on numerical examples. Although the results are promising, the stability of the scheme is uncertain and only assured for certain subsurface models. The last part of the chapter, therefore, presents a modified scheme with greater stability, which is less susceptible to subsurface conditions.

2.2. GREEN'S FUNCTION REPRESENTATIONS

This section reviews briefly the theory of the Green's function representations that are the basis for the Marchenko method. For a more elaborate derivation the reader is referred to Wapenaar et al. (2014) and Slob et al. (2014). As starting point, imagine an inhomogeneous lossless subsurface bounded by transparent acquisition surface $\mathbb{S}_0$. The reflection response at this surface is given by $R(\mathbf{x}_R,\mathbf{x}_S,t)$, with $\mathbf{x}_S$ a dipole source, $\mathbf{x}_R$ monopole receivers, and t denoting the time. In this chapter we investigate how to account for irregularly sampled sources. Via reciprocity, $\mathbf{x}_R$ can be interpreted as a monopole source and $\mathbf{x}_S$ as a dipole receiver. Hence, the method developed in this chapter can also be used to account for irregularly sampled receivers. We define the focal depth at surface $\mathbb{S}_A$, on which the virtual receivers are located. These virtual receivers are used to observe the up- and down-going Green's functions: $G^-(\mathbf{x}_A,\mathbf{x}_R,t)$ and $G^+(\mathbf{x}_A,\mathbf{x}_R,t)$, respectively. Here, $\mathbf{x}_A$ is the location of the virtual receivers at the focal depth. For the definition of the focusing functions, the medium is truncated below the focal depth, resulting in a medium that is inhomogeneous between $\mathbb{S}_0$ and $\mathbb{S}_A$, and homogeneous above and below these surfaces. In this medium we define a downgoing focusing function $f_1^+(\mathbf{x}_S,\mathbf{x}_A,t)$, which, when injected from the surface, focuses at the focal depth $\mathbb{S}_A$ at $\mathbf{x}_A$. Moreover, $f_1^-(\mathbf{x}_R,\mathbf{x}_A,t)$ is the upgoing response of the truncated medium as measured at the surface, known as the upgoing focusing function. These ideas can be combined in two integral equations, as follows (Slob et al., 2014; Wapenaar et al., 2014, and Appendix B):

$$G^-(\mathbf{x}_A,\mathbf{x}_R,t)+f_1^-(\mathbf{x}_R,\mathbf{x}_A,t)=\int_{\mathbb{S}_0} R(\mathbf{x}_R,\mathbf{x}_S,t)*f_1^+(\mathbf{x}_S,\mathbf{x}_A,t)d\mathbf{x}_S, \tag{2.1}$$

$$G^+(\mathbf{x}_A,\mathbf{x}_R,t)-f_1^+(\mathbf{x}_R,\mathbf{x}_A,-t)=-\int_{\mathbb{S}_0} R(\mathbf{x}_R,\mathbf{x}_S,t)*f_1^-(\mathbf{x}_S,\mathbf{x}_A,-t)d\mathbf{x}_S. \tag{2.2}$$

The asterisk in these equations denotes a temporal convolution. For acoustic media, the focusing- and Green's functions on the left-hand side are separable in time by a windowing function. In practice, the infinite integrals on the right-hand side are approximated by finite sums over the available sources. For the right-hand side (RHS) of Equation 2.1 this yields:

$$\sum_i R(\mathbf{x}_R,\mathbf{x}_S^{(i)},t)*f_1^+(\mathbf{x}_S^{(i)},\mathbf{x}_A,t)*S(t), \tag{2.3}$$

and for the RHS of Equation 2.2:

$$-\sum_i R(\mathbf{x}_R,\mathbf{x}_S^{(i)},t)*f_1^-(\mathbf{x}_S^{(i)},\mathbf{x}_A,-t)*S(t), \tag{2.4}$$

where i denotes the source position and $S(t)$ the source signature. When the reflection response is not well sampled, these summations cause distortions in the responses on the left-hand sides of Equations 2.1 and 2.2.

2.3. POINT-SPREAD FUNCTIONS

Wapenaar and van IJsseldijk (2020) introduce point-spread functions (PSFs) to correct for imperfect sampling. These PSFs exploit the fact that the ideal downgoing focusing function is the inverse of the transmission response. A convolution of the focusing function with the transmission response T should, therefore, give a bandlimited delta pulse in space and time:

$$\delta(\mathbf{x}'_{H,A}-\mathbf{x}_{H,A})\delta(t)=\int_{\mathbb{S}_0} T(\mathbf{x}'_A,\mathbf{x}_S,t)*f_1^+(\mathbf{x}_S,\mathbf{x}_A,t)\,d\mathbf{x}_S. \tag{2.5}$$

An alternative form with integration over the focal depth is given by:

$$\delta(\mathbf{x}_{H,S}-\mathbf{x}'_{H,S})\delta(t)=\int_{\mathbb{S}_A} f_1^+(\mathbf{x}_S,\mathbf{x}_A,t)*T(\mathbf{x}_A,\mathbf{x}'_S,t)\,d\mathbf{x}_A. \tag{2.6}$$

However, for imperfectly sampled data this delta pulse gets blurred. This blurring quantifies the imperfect sampling, as follows:

$$\Gamma_1^+(\mathbf{x}'_A,\mathbf{x}_A,t)=\sum_i T(\mathbf{x}'_A,\mathbf{x}_S^{(i)},t)*f_1^+(\mathbf{x}_S^{(i)},\mathbf{x}_A,t)*S(t). \tag{2.7}$$

Here Γ_1^+ is the downgoing PSF. Similarly, a quantity Y_1 is defined as the inverse of the time-reversed, upgoing focusing function:

$$\delta(\mathbf{x}'_{H,A}-\mathbf{x}_{H,A})\delta(t)=\int_{\mathbb{S}_0} Y_1(\mathbf{x}'_A,\mathbf{x}_S,t)*f_1^-(\mathbf{x}_S,\mathbf{x}_A,-t)\,d\mathbf{x}_S, \tag{2.8}$$

or alternatively:

$$\delta(\mathbf{x}_{H,S}-\mathbf{x}'_{H,S})\delta(t)=\int_{\mathbb{S}_A} f_1^-(\mathbf{x}_S,\mathbf{x}_A,-t)*Y_1(\mathbf{x}_A,\mathbf{x}'_S,t)\,d\mathbf{x}_A, \tag{2.9}$$

Again, the irregular sampling will result in a blurring of the delta pulse on the left-hand side (LHS) of Equation 2.8. The convolution to quantify the upgoing PSF (Γ_1^-) then becomes:

$$\Gamma_1^-(\mathbf{x}'_A,\mathbf{x}_A,t)=\sum_i Y_1(\mathbf{x}'_A,\mathbf{x}_S^{(i)},t)*f_1^-(\mathbf{x}_S^{(i)},\mathbf{x}_A,-t)*S(t). \tag{2.10}$$

Once again, in the case of perfect sampling this PSF would be equal to a bandlimited delta pulse in space and time. Note that this inverse (Y_1) is not necessarily stable, because f_1^- is a reflection response. On the contrary, f_1^+ is more stable and more likely to be invertible (i.e. in the limiting case of a 1D medium it is a minimum-phase function, which is always invertible). This will be elaborated upon in the discussion section.
Next, Wapenaar and van IJsseldijk (2020) apply these newly acquired PSFs to Equations 2.1 and 2.2, respectively. For both sides of Equation 2.1 we employ the operator

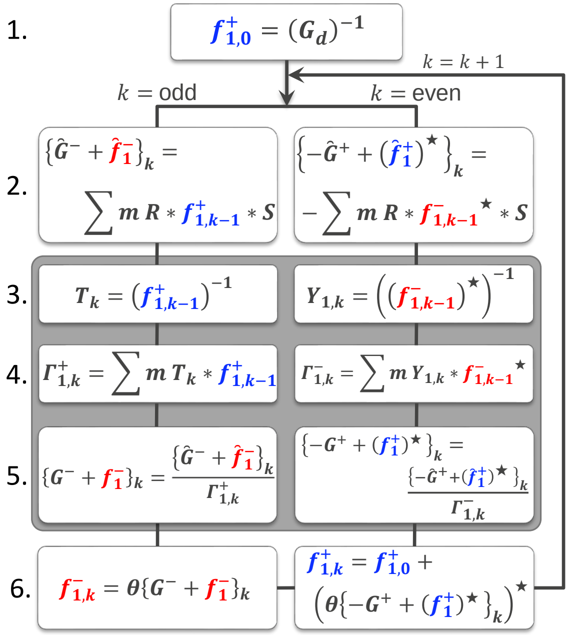

Figure 2.1: Flowchart with the proposed iterative Marchenko scheme, steps 3 to 5 account for imperfectly sampled data. Here f and G represent the focusing- and Green's functions, respectively, S is the source signature. m is a masking operator, that kills all the traces with missing sources. k denotes the iteration number. The arch over a symbol denotes that the response is contaminated by the imperfect sampling, the superscript star denotes time-reversal. The inline asterisks denote convolutions or correlations, which are then summed over the imperfectly sampled sources. Finally, θ is the time-windowing operator.

$\int_{\mathbb{S}_A}\{\cdot\} * \Gamma_1^+(\mathbf{x}'_A,\mathbf{x}_A,t)\,d\mathbf{x}'_A$, whereas both sides of Equation 2.2 require the use of the operator $\int_{\mathbb{S}_A}\{\cdot\} * \Gamma_1^-(\mathbf{x}'_A,\mathbf{x}_A,t)\,d\mathbf{x}'_A$. The resulting equations can be further simplified using Equation 2.6, 2.7, 2.9 and 2.10 to derive two new representations for irregularly sampled data:

$$\hat{G}^-(\mathbf{x}_A,\mathbf{x}_R,t) + \hat{f}_1^-(\mathbf{x}_R,\mathbf{x}_A,t) = \sum_i R(\mathbf{x}_R,\mathbf{x}_S^{(i)},t) * f_1^+(\mathbf{x}_S^{(i)},\mathbf{x}_A,t) * S(t), \tag{2.11}$$

$$\hat{G}^+(\mathbf{x}_A,\mathbf{x}_R,t) - \hat{f}_1^+(\mathbf{x}_R,\mathbf{x}_A,-t) = -\sum_i R(\mathbf{x}_R,\mathbf{x}_S^{(i)},t) * f_1^-(\mathbf{x}_S^{(i)},\mathbf{x}_A,-t) * S(t), \tag{2.12}$$

with:

$$\hat{G}^\pm(\mathbf{x}_A,\mathbf{x}_R,t) = \int_{\mathbb{S}_A} G^\pm(\mathbf{x}'_A,\mathbf{x}_R,t) * \Gamma_1^\mp(\mathbf{x}'_A,\mathbf{x}_A,t)\,d\mathbf{x}'_A, \tag{2.13}$$

and

$$\hat{f}_1^\pm(\mathbf{x}_R,\mathbf{x}_A,\mp t) = \int_{\mathbb{S}_A} f_1^\pm(\mathbf{x}_R,\mathbf{x}'_A,\mp t) * \Gamma_1^\mp(\mathbf{x}'_A,\mathbf{x}_A,t)\,d\mathbf{x}'_A. \tag{2.14}$$

Equations 2.11 and 2.12 have two interesting features. First, the right-hand sides are now the same as Equations 2.3 and 2.4. Second, the responses on the left-hand sides now contain the PSFs, which apply a blurring effect to each response. Note that the

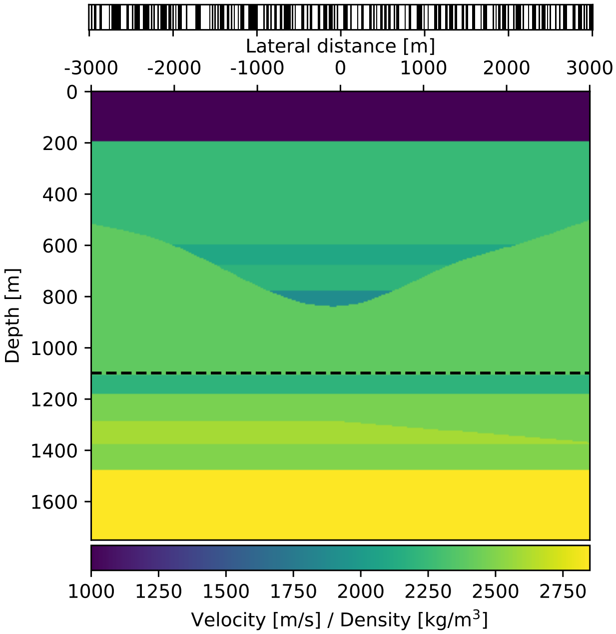

Figure 2.2: Model used in the numerical irregular sampling experiment, the dashed line shows the focal level. The barcode shows the irregular sampling, with the white spaces denoting the excluded sources.

imperfectly sampled data can now be deblurred by a multidimensional deconvolution (MDD) with the PSFs, assuming these PSFs are known.

2.4. ITERATIVE MARCHENKO SCHEME

Wapenaar and van IJsseldijk (2020) verify the representations in Equations 2.11 and 2.12, using analytically modelled focusing functions (i.e. both the reflection response and focusing functions on the RHS of the equations are known). In practice, these focusing functions are unknown, and have to be retrieved from the Marchenko equations. This can be achieved iteratively or by inversion of the Marchenko equations. Here, we aim to integrate the representations for imperfectly sampled data with the iterative approach (Thorbecke et al., 2017).

Figure 2.1 shows the proposed iterative Marchenko scheme, which corrects for imperfect sampling in each iteration k. The first step is to estimate the initial downgoing focusing function ($f^+_{1,0}$). Traditionally, this is approximated by the time-reversal of the direct arrival of the Green's function. However, to ensure that the convolution of the transmission response and downgoing focusing function gives a delta pulse in space and time with the correct amplitudes, the proposed scheme inverts the direct arrival in step 1:

$$f^+_{1,0}(\mathbf{x}_S, \mathbf{x}_A, t) \approx G_d^{inv}(\mathbf{x}_S, \mathbf{x}_A, t). \tag{2.15}$$

In practice this inversion is achieved by a least-squares-based inversion in the frequency domain, where for each frequency slice a band-limited identity matrix (delta pulse) is divided by G_d to find $f^+_{1,0}$. Note that this approach requires a matrix with a size equal to the number of shots multiplied with the number of focal points, and can, therefore, not be done for a single focusing point.

The next step computes the focusing- and Green's functions by a convolution or correlation for the odd or even iterations, respectively. The odd iterations are computed according to Equation 2.11, where the downgoing focusing function on the RHS is retrieved from the initial condition for the first iteration or from the previous iteration for subsequent iterations. Similarly, the even iterations use the upgoing focusing functions from the previous iteration in the correlation with the reflection response, as shown in Equation 2.12. Note, for well-sampled data the computed focusing- and Green's functions in this step are free of distortions, therefore the resulting focusing- and Green's functions are equal to these functions in the standard scheme:

$$\{\hat{G}^{\pm}(\mathbf{x}_A,\mathbf{x}_R,t) \mp \hat{f}_1^{\pm}(\mathbf{x}_R,\mathbf{x}_A,\mp t)\}_k = \{G^{\pm}(\mathbf{x}_A,\mathbf{x}_R,t) \mp f_1^{\pm}(\mathbf{x}_R,\mathbf{x}_A,\mp t)\}_k. \tag{2.16}$$

In this case steps 3 to 5 are redundant and can be omitted, this indeed reduces the proposed scheme to the standard iterative Marchenko scheme.

For irregularly sampled reflection data, steps 3 to 5 are introduced. The first objective is to find an estimate of the transmission response and quantity Y_1 for odd and even iterations, respectively. Since these responses are defined as the inverse of the focusing functions, they can be obtained by inversion of the following equations:

$$\delta(\mathbf{x}'_{H,A}-\mathbf{x}_{H,A})\delta(t) = \int_{\mathbb{S}_0} T_k(\mathbf{x}'_A,\mathbf{x}_S,t) * f^+_{1,k-1}(\mathbf{x}_S,\mathbf{x}_A,t)\,d\mathbf{x}_S, \tag{2.17}$$

and

$$\delta(\mathbf{x}'_{H,A}-\mathbf{x}_{H,A})\delta(t) = \int_{\mathbb{S}_0} Y_{1,k}(\mathbf{x}'_A,\mathbf{x}_S,t) * f^-_{1,k-1}(\mathbf{x}_S,\mathbf{x}_A,-t)\,d\mathbf{x}_S. \tag{2.18}$$

T_k in Equation 2.17 denotes the estimated transmission response for each odd iteration k, and $f^+_{1,k-1}$ is the downgoing focusing function computed in the former iteration $k-1$. Equation 2.18 computes an approximation of the quantity $Y_{1,k}$ for each even iteration, based on the upgoing focusing function from the preceding iteration. Note that both the up- and downgoing focusing functions are deblurred, and free of distortions from the imperfect sampling. The two integral representations are, therefore, evaluated over a regular grid (i.e. as if no sources are missing). Next, the PSFs have to be computed, using the estimates of T and Y_1 (step 4 in Figure 2.1). Analogous to Equation 2.7, the downgoing PSF for each odd iteration is retrieved by evaluating the convolution of T_k and $f^+_{1,k-1}$ over the irregular sampled sources. For the even iterations we consider the correlation of $Y_{1,k}$ and $f^-_{1,k-1}$, as in Equation 2.10. Subsequently, in step 5 the distorted focusing- and Green's functions, from step 2 of the scheme, are deblurred by a multidimensional deconvoltion with the PSFs. Similar as in Equation 2.15, this is effectively accomplished by a least-squares-based inversion, and once again it is done for all focal points simultaneously. Consequently, our scheme can not operate on individual focusing points, but rather multiple points are considered simultaneously. This is in contrast to the standard Marchenko scheme, which can operate on a single focusing point. After the MDD, the resulting focusing- and Green's functions are reconstructed as if they were retrieved with well-sampled data. Finally, the last step separates the focusing function from the Green's function using a time-windowing operator (θ in Figure 2.1). This final step is identical to that in the standard Marchenko scheme.

Each iteration is initialized with a "clean" (i.e. deblurred) focusing function from the preceding iteration. This is required at the start of each iteration, otherwise the errors from the irregular sampled reflection data would accumulate. Therefore, steps 3 to 5 are enforced with every iteration.

2.5. NUMERICAL EXAMPLE

The performance of the proposed scheme is tested on synthetic data. The 2D model for this test is shown in Figure 2.2. For convenience, the density and velocity parameters are chosen to be the same in each layer, but this is not required for successful application of the scheme. The observant reader will note the strong contrast in acoustic impedance between the top two layers of the model, at a depth of 200 meters. This contrast ensures that the inversion of f_1^- for retrieving Y_1 is stable, because most of the energy gets concentrated at the early onsets of the reflection response. Note that this constraint on the subsurface model is significantly relaxed with a second scheme discussed later on in this chapter.

The reflection response of the medium is modeled using a wavelet with a flat spectrum between 5 and 80 Hz. In total 601 sources and receivers are used with an initial spacing of 10 meters. For the irregular sampling 50 % of the sources are removed at random, such that source-side aliasing is avoided, as can be seen in the barcode plot in Figure 2.2. In practice, these sources are killed (i.e. set to 0), as opposed to being entirely removed from the reflection response. Next, the direct arrival of the Green's function between the focal depth and the Earth's surface is estimated in a smooth velocity model. As previously stated, the inverse of this direct arrival is used for the initial estimate of the downgoing focusing function, as opposed to the time-reversed version that is traditionally used. The reflection response and this initial estimate together are all the required inputs for the standard Marchenko scheme. Finally, for the fourth step of our proposed scheme the location of the sources (e.g. the barcode in Figure 2.2) is required.

Figure 2.3 shows the results of the numerical experiment, each column in the figure represents the results after 12 iterations, that is six updates each to the down- and upgoing focusing functions, using one of the three schemes. The first column shows the results where the standard Marchenko scheme is used with the irregularly sampled reflection data. Next, the middle column shows the results of the proposed scheme, again with irregularly sampled data. Finally, the last column displays a reference result, that was obtained by using the standard Marchenko scheme on reflection data without removing any sources. The red dashed line in the figure denotes the separation in time of the Green's functions below, and focusing functions above. In the case of irregular sampling in the standard scheme (as presented in the first column), three main artifacts can be identified. Firstly, clear distortions of some reflectors are observed, especially around the strong events. These distortions are most noticeable of all artifacts, and obstruct later events in the downgoing Green's function ($\hat{G}^+$). The ellipses indicate some of these artifacts. Secondly, the amplitudes of some events are incorrect or the events are not reconstructed at all (as shown by the red arrows). For example, the downgoing focusing function ($\hat{f}^+$) is largely suppressed, as well as some events in the upgoing focusing

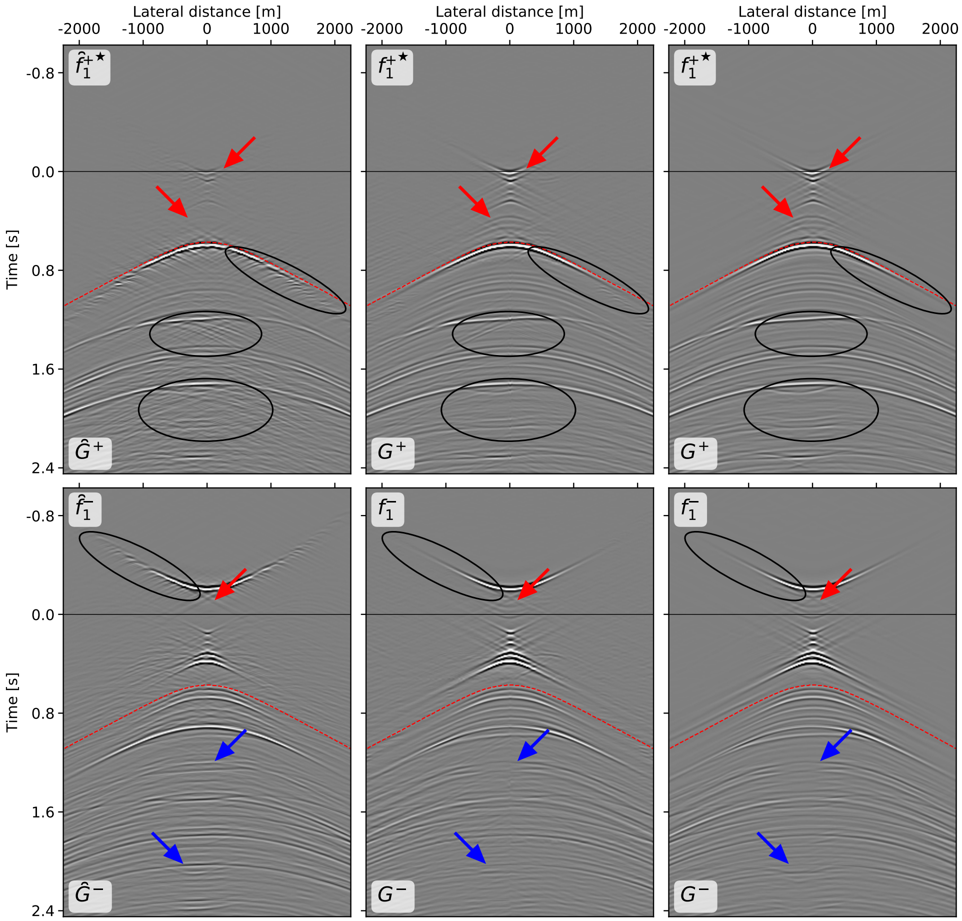

Figure 2.3: The top row shows the time-reversed downgoing focusing function ($\{f_1^+\}^\star$) and downgoing Green's function (G^+), and the bottom row shows the upgoing focusing function (f_1^-) and upgoing Green's function (G^-), the star superscript denotes time-reversal. The dashed, red lines indicate the separation between the focusing- and Green's functions. The left column shows the result of irregularly sampled data after 12 iterations of the standard Marchenko scheme. The middle column shows the results when using our scheme on the same data (Figure 2.1), again 12 iterations are used. Finally, the 3rd column shows the reference result, obtained after 12 iterations of the standard Marchenko scheme with well-sampled data. Each panel is scaled with its maximum value. The arrows and ellipses show artifacts arising from the irregular sampling. Distortions caused by the irregular sampling are indicated with the ellipses. The red arrows show events that deviate in amplitude or are missing altogether. Finally, the blue arrows mark erroneous reflectors.

function ($\hat{f}^-$). Lastly, some new and undesired reflectors are appearing in the results, especially at later times (> 1.2 s) many of the reflectors in the upgoing Green's function ($\hat{G}^-$) are deviating from the reference result in the third column. Examples of such undesired reflectors are marked with the blue arrows. All these three types of artifacts are mostly removed by using the proposed scheme (middle column), and the results of this scheme

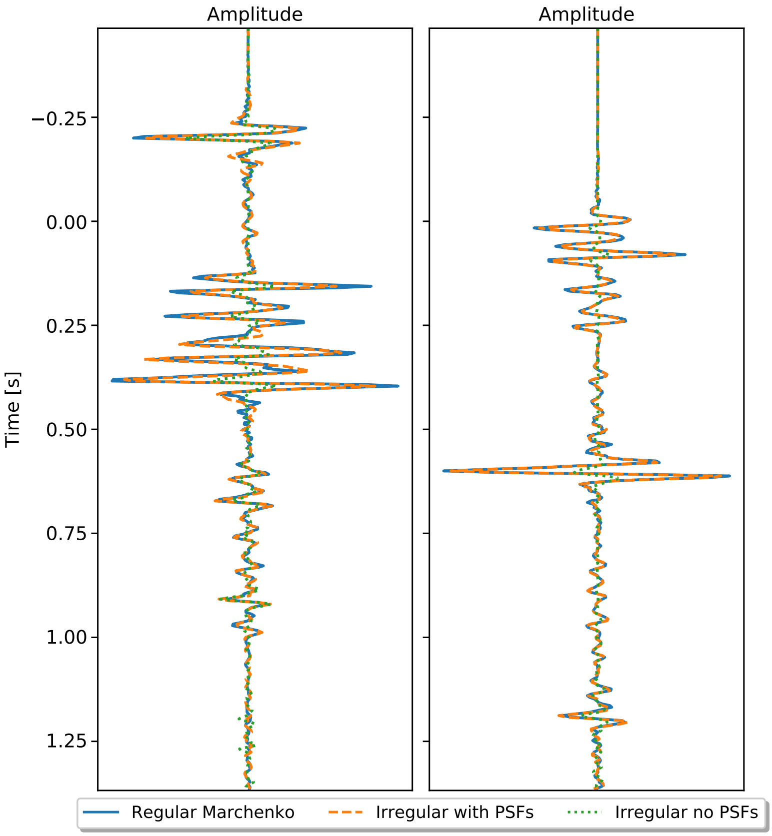

Figure 2.4: Comparison of the amplitudes in the middle trace (at offset 0 m) of each panel in Figure 2.3. On the left are the time-reversed downgoing focusing function ($\{f_1^+\}^\star$) and downgoing Green's function (G^+). The upgoing focusing function (f_1^-) and upgoing Green's function (G^-) are shown on the right.

show much more resemblance with the reference results. This implies that the proposed scheme both deblurs the results of irregular sampling effects, and also retrieves the amplitudes of the events more accurately. However, the method does introduce some of its own artifacts; as it introduces edge effects, especially at later times. These artifacts are introduced by the MDD of poorly sampled data with the PSFs, and they are suppressed by using directional FK-filters.

The amplitude reconstruction by the proposed scheme is further illustrated in Figure 2.4, where the middle trace of each panel from Figure 2.3 is plotted. In Figure 2.4 the results of the proposed scheme in orange quite closely match the reference results in blue, whereas the standard scheme fails to recover the correct amplitudes in the case of irregularly sampled reflection data (green line). This difference in amplitudes cannot simply be negated by scaling with a constant factor, because the error has a different magnitude at different times. However, this match can be improved by scaling individual traces with the source spacing, nevertheless the artifacts in Figure 2.3 will not be improved with such

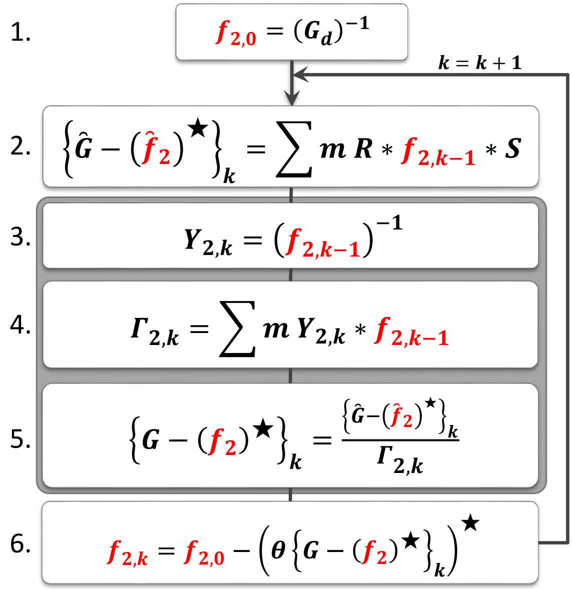

Figure 2.5: Flowchart displaying the full wavefield Marchenko scheme, where steps 3 to 5 account for imperfectly sampled data. f and G represent the focusing- and Green's functions, respectively, and the arch denotes contamination by the imperfect sampling. S is the source signature. m is a masking operator, that kills all the traces with missing sources. k is the iteration number, the superscript star denotes time-reversal, and the inline asterisks denotes a convolution. θ is the time-windowing operator.

scaling.

2.6. A MORE STABLE ALTERNATIVE

While the previous results show clear potential, the need for a stable inversion of f_1^- imposes a large constraint on the subsurface models that are suitable for the method. This section, therefore, explores how this unstable inversion can be avoided. In order to achieve this Equations 2.1 and 2.2 are combined into a single equation, that retrieves the full wavefield Green's functions between a focal point and surface, defined as follows:

$$G(\mathbf{x}_R,\mathbf{x}_A,t) = G^+(\mathbf{x}_A,\mathbf{x}_R,t) + G^-(\mathbf{x}_A,\mathbf{x}_R,t). \tag{2.19}$$

This gives a new representation for irregular sampling with the full wavefield Green's function:

$$\hat{G}(\mathbf{x}_R,\mathbf{x}_A,t) - \hat{f}_2(\mathbf{x}_A,\mathbf{x}_R,-t) = \sum_i R(\mathbf{x}_R,\mathbf{x}_S^{(i)},t) * f_2(\mathbf{x}_A,\mathbf{x}_S^{(i)},t) * S(t), \tag{2.20}$$

with:

$$f_2(\mathbf{x}_A,\mathbf{x}_R,t) = f_1^+(\mathbf{x}_R,\mathbf{x}_A,t) - f_1^-(\mathbf{x}_R,\mathbf{x}_A,-t). \tag{2.21}$$

The arches over the Green's and focusing functions in Equation 2.20 denote convolution with a new PSF Γ_2:

$$\Gamma_2(\mathbf{x}'_A, \mathbf{x}_A, t) = \sum_i Y_2(\mathbf{x}'_A, \mathbf{x}_S^{(i)}, t) * f_2(\mathbf{x}_A, \mathbf{x}_S^{(i)}, t) * S(t). \tag{2.22}$$

Here, Y_2 is the inverse of focusing function f_2. Note that this inverts a superposition of the downgoing and upgoing focusing functions, thereby avoiding the independent inversion of f_1^- (see Equation 2.18). A detailed derivation of Equations 2.20 to 2.22 is given in Appendix A.

Next, we integrate these full wavefield equations into an iterative scheme, analogous to the integration of the decomposed equations shown before. An overview of this new iterative scheme is shown in Figure 2.5. The scheme is initialized with an estimate for the first focusing function, which is again equal to the inverse of the direct arrival of the Green's function:

$$f_{2,0}(\mathbf{x}_A, \mathbf{x}_S, t) \approx G_d^{inv}(\mathbf{x}_S, \mathbf{x}_A, t). \tag{2.23}$$

This initial focusing function is convolved with the subsampled reflection response (step 2 in Figure 2.5). Note that f_2 appears on both the right- and left-hand side of Equation 2.20, thus we no longer need to differentiate between odd and even iterations. Instead, the individual equation iteratively finds the full wavefield Green's and focusing functions. However, these functions are contaminated by the imperfect sampling, which needs to be deblurred using a PSF with each iteration. The first step in finding this PSF is estimating quantity $Y_{2,k}$ as follows (Equation 2A4):

$$\delta(\mathbf{x}'_{H,A} - \mathbf{x}_{H,A})\delta(t) = \int_{\mathbb{S}_0} Y_{2,k}(\mathbf{x}'_A, \mathbf{x}_S, t) * f_{2,k-1}(\mathbf{x}_A, \mathbf{x}_S, t)\, d\mathbf{x}_S. \tag{2.24}$$

In this equation, $f_{2,k-1}$ is the deblurred version of the focusing function from the previous iteration. The focusing functions and its inverse are then used to approximate the PSF for the current iteration (Equation 2A6):

$$\Gamma_{2,k}(\mathbf{x}'_A, \mathbf{x}_A, t) = \sum_i Y_{2,k}(\mathbf{x}'_A, \mathbf{x}_S^{(i)}, t) * f_{2,k-1}(\mathbf{x}_A, \mathbf{x}_S^{(i)}, t). \tag{2.25}$$

Subsequently, this PSF is used to deblur both the Green's and focusing functions from the step 2 of Figure 2.5 (Equations 2A10 and 2A11). Finally, $-f_{2,k}^{\star}$ (the superscript $\star$ indicates time-reversal) is separated from the Green's function using a time-gate, reversed in time, and multiplied with -1 (step 6 in Figure 2.5). This updated focusing function is then used as input for the next iteration. This process can then be repeated until the results have sufficiently converged, meaning the updated focusing function does not change significantly compared to the preceding iteration.

This new scheme successfully avoids the inversion of f_1^-, and it is therefore more stable. However, the drawback of this scheme is that it does not return the Green's function decomposed into an up- and down-going part. These decomposed functions are required for redatuming the reflection response from the surface to the focal depth. This issue can be circumvented, if either the downgoing or upgoing focusing functions is available. Previously, we found that the odd iterations in the flowchart of Figure 2.1 are relatively

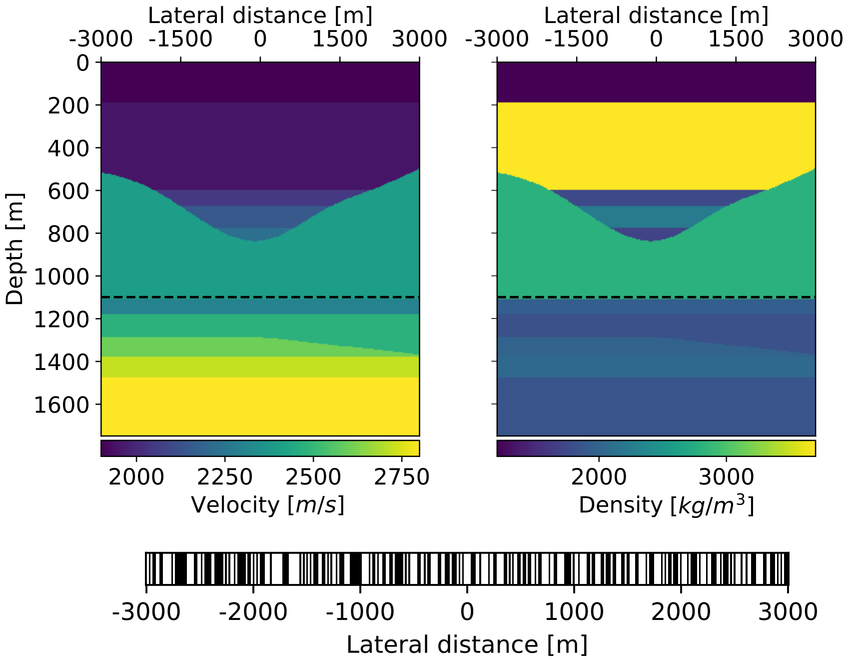

Figure 2.6: Model used in the numerical irregular sampling experiment, with the velocities on the left and densities on the right. The dashed line shows the focal level. The barcode shows the irregular sampling, with the white spaces denoting the excluded sources (50 %).

stable, thus this can be used to estimate $f^-_{1,k}$ and G^- for odd iterations. Note, that solving Equation 2.20 is numerically the same as solving the coupled equations (Thorbecke et al., 2017), the aforementioned drawback is, therefore, only an increase in complexity when the decomposed functions are desired (i.e. the computational time increases as 1.5 times as many equations need to be solved). The final step is now to find an approximation for $f^+_{1,k}$ in the even iterations, which can no longer use the even iterations of Figure 2.1, since these iterations introduce the unstable inverse Y_1. Instead the relation in Equation 2.21 is used to find the update for the downgoing focusing function, as follows:

$$f^+_{1,k}(\mathbf{x}_R,\mathbf{x}_A,t) = f_{2,k}(\mathbf{x}_A,\mathbf{x}_R,t) + f^-_{1,k-1}(\mathbf{x}_R,\mathbf{x}_A,-t) \tag{2.26}$$

Note that both $f^-_{1,k-1}$ as well as $f_{2,k}$ have already been deblurred, thus there are no sampling artifacts in $f^+_{1,k}$ (e.g. no PSF correction is required). Furthermore, Equation 2.15 is still valid to calculate $f^+_{1,0}$ for the initial iteration. Finally, the downgoing Green's function can be calculated after the last iteration using Equation 2.19:

$$G^+(\mathbf{x}_A,\mathbf{x}_R,t) = G(\mathbf{x}_R,\mathbf{x}_A,t) - G^-(\mathbf{x}_A,\mathbf{x}_R,t). \tag{2.27}$$

From now on, the scheme introduced in this section and the scheme introduced before (summarized in Figure 2.1) will be referred to as the full wavefield scheme and the decomposed scheme, respectively.

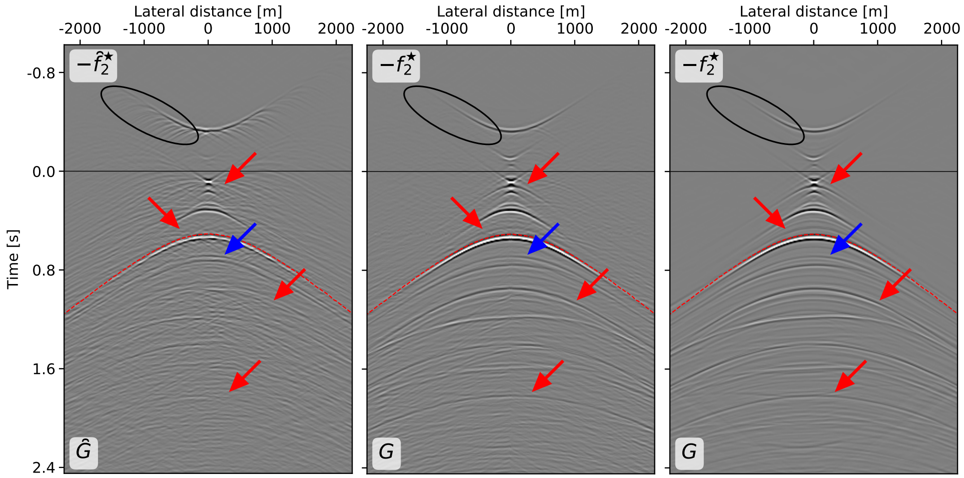

Figure 2.7: The left panel shows the result of irregularly sampled data after 10 iterations of the standard Marchenko scheme. The middle panel shows the results when using our scheme on the same data, again 10 iterations are used. Finally, the 3rd panel shows the reference result, obtained after 10 iterations of the standard Marchenko scheme with well-sampled data. Each panel is scaled with its maximum value. The arrows and ellipses show artifacts arising from the irregular sampling. Distortions caused by the irregular sampling are indicated with the ellipses. The red arrows show events that deviate in amplitude or are missing altogether. Finally, the blue arrow marks an erroneous reflector.

2.7. FULL WAVEFIELD SCHEME NUMERICAL EXAMPLE

Now, the full wavefield scheme will be tested with a numerical example. Figure 2.6 shows the new velocity and density models that are used for this example. Contrary to the previous numerical example, there is no requirement for a strong contrast in acoustic impedance between the top two layers. The direct arrival of the Green's function is calculated in a smooth version of this model. The other parameters for modeling the reflection response remain the same, meaning that the source wavelet has a flat spectrum, and that 601 co-located sources and receivers are placed with a 10 meters separation. For the imperfect sampling, again 50 % of sources are removed, as depicted by the barcode plot in Figure 2.6.

Figure 2.7 presents the resulting Green's and focusing functions after 10 iterations of the full wavefield scheme. The first panel shows the results when using imperfectly sampled data with the standard full wavefield scheme (i.e. using only steps 1,2 and 6 in Figure 2.5). Next, the middle panel shows the corrected Green's and focusing function obtained with the proposed full wavefield scheme (using all steps in Figure 2.5). Finally, the third panel contains the reference result that is acquired with regularly sampled data. There are a number of interesting artifacts visible in the figure. First, sampling artifacts are highlighted by the black ellipse. Furthermore, the red arrows denote events that are not retrieved when using imperfectly sampled data. Lastly, the blue arrow marks a reflector recovered when using the imperfectly sampled data, that differs from the reflectors in the corrected and reference result. While a clear improvement can be observed when

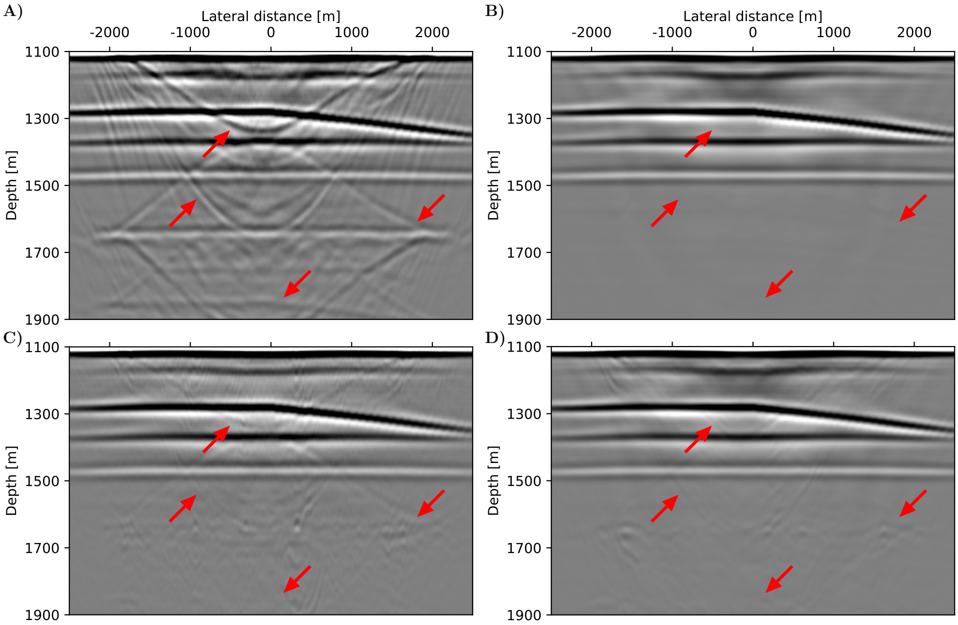

Figure 2.8: Images of the target zone (i.e. at depths below 1100 meters). A) shows the migration of the redatumed reflection response, retrieved from the irregularly sampled data after 10 iterations of the standard Marchenko scheme. B) displays the reference migration, obtained using the results after 10 iterations of the standard Marchenko scheme with well-sampled data.. C) is the migration after 10 iterations of the newly proposed scheme on the same data. Finally, D) shows the results of reconstructing the reflection data first, and then applying 10 iterations of the standard Marchenko scheme. Each panel is scaled with its maximum value. The arrows show overburden effects that are not completely eliminated due to the use of irregularly sampled data.

using the new full wavefield scheme, the PSF-corrected result still deviates considerably from the reference result. The match between the results especially deteriorates at larger times (i.e. at $t > 2$s). To further assess the performance of this method, the decomposed up- and down-going wavefields will now be considered, thus the full wavefield Green's function needs to be decomposed into the up- and down-going versions. As previously stated G^{-} can be iteratively acquired by using the odd iterations in Figure 2.1 with Equation 2.26 to update f^{+} for the even iterations. Subsequently, G^{+} can be calculated from Equation 2.27. Using the decomposed Green's functions, the redatumed reflection response at the focal level can now be found, by means of the following relation (Wapenaar et al., 2014):

$$G^{-}(\mathbf{x}_A, \mathbf{x}_R, t) = \int_{\mathbb{S}_0} R(\mathbf{x}_A, \mathbf{x}'_A, t) * G^{+}(\mathbf{x}'_A, \mathbf{x}_R, t)\, d\mathbf{x}'_A \tag{2.28}$$

The redatumed reflection response is acquired from this equation with a MDD. Next, this reflection response is migrated, to get an image of the target, free from multiples related to the overburden. Note that this requires a smooth version of the velocity model below the focal depth. The results of the migration are displayed in Figure 2.8. Panel A) and C) show the results using irregularly sampled data of the full wavefield scheme with and without PSF-correction, respectively. The panel in B) holds the reference Marchenko result obtained with regularly sampled data. Finally, D) shows a migration of results by the standard Marchenko scheme, where the irregularly sampled reflection data are reconstructed before applying the scheme. In order to achieve this reconstruction, a slight NMO correction is first applied to compress the range of ray parameters. Next, a sparse inversion using the Radon transform is used to restore the missing data. Lastly, the NMO correction is undone, and the originally available sources are combined with the reconstructed result to acquire the reconstructed reflection response. Even though the internal multiples are not perfectly suppressed using the PSF-corrections (2.8C), the result matches the reference image (2.8B) significantly better than the image without any corrections. The results with reconstructed reflection data (2.8D) realize an even better match with the reference.

2.8. DISCUSSION

The results show that the proposed schemes can successfully be used on irregularly sampled reflection data. However, there are some limitations and possible improvements that will now discussed.

First, we note that the discretizations in 2.3 and 2.4 should be multiplied with the irregular integration step $\Delta\mathbf{x}_S^{(i)}$. However, the current implementation with PSFs uses a regular integration step ($\Delta\mathbf{x}_S = 10$m) based on the regular grid of sources and receivers. This poses no issues for the schemes that apply the PSF-correction, as they implicitly correct for the irregular source distances. Nevertheless, one could argue that the irregular scheme without PSFs should include the irregular source distances instead of the regular distances. This approach was also tested, but did not significantly alter the results of the blurred images.

Second, the largest limitation when using the decomposed equations is the instability of quantity Y_1, which was introduced as the inverse of the upgoing focusing function. This was circumvented with the introduction of a full wavefield scheme that avoids this inverse. However, the full wavefield scheme appears to have decreased accuracy at later times, as observed when comparing the second and third columns of Figures 2.3 and 2.7.

Another important factor is the computational cost of the method. For every iteration, the decomposed scheme adds one convolution and two MDD steps to the standard Marchenko scheme, which only consists of a single convolution per iteration. Furthermore, additional operations are required to decompose the results of the full wavefield scheme into up- and down-going responses. Specifically, the upgoing Green's and focusing functions have to be computed, according to the odd iterations of the decomposed scheme. Therefore, the full wavefield scheme adds a convolution and two inversions to the computational load for each iteration of the method, thus increasing the computational costs and time of the method.

Alternatively to the full wavefield scheme, the inversion of f_1^- can also be avoided by utilizing a Marchenko scheme for data that include free-surface multiples (Singh et al., 2015). This scheme would have the same number of operations as the decomposed scheme, and thus would come at a lower computational cost than the full wavefield scheme. However, including free-surface multiples can lead to instabilities in the Marchenko series (e.g. Dukalski & de Vos, 2017; Staring et al., 2017), but these instabilities are expected to be less troublesome than the instability of quantity Y_1. Alternatively, a conjugate gradient scheme could be considered instead of the iterative scheme used here (Slob & Zhang, 2021). Nevertheless, further research is required to assess the viability of such schemes.

Although, the new formulation no longer requires collocation of the sources and receivers in the Marchenko scheme, it is important to note that sources and receivers are still required to be at the same depth. Traditionally, this is achieved by redatuming the sources down to the receiver level after applying surface related multiple elimination (SMRE, Verschuur et al., 1992). However, SRME will also suffer from irregular acquisition effects, so a different scheme for removing free-surface multiples is desirable, such as estimating primaries by sparse inversion (EPSI, van Groenestijn & Verschuur, 2009), which is less sensitive to the acquisition geometry.

While the inverse of the downgoing focusing function always exists, there is a different way to estimate the transmission response, which does not require any explicit inversions (Vasconcelos et al., 2018). This methodology was also tested to calculate the transmission response in step 3 of the proposed decomposed scheme. While this method achieved promising results in 1.5D media, we found that the results were unsatisfactory in the 2D model. Therefore, the transmission response was estimated by inversion instead.

The new methodology is unable to account for irregular sampling of both sources and receivers; the sampling can only be irregular in the same dimension as the integration in Equations 2.1 and 2.2. On the contrary, the method introduced by Haindl et al. (2018) assumes irregular sampling in the opposite dimension. A combination of these complementary methods is, therefore, envisioned to deal with irregular sampling in both the source and receiver dimensions simultaneously. However, further research into this topic is required.

Finally, we note that the reflection data can also be reconstructed before applying the Marchenko method. Subsequently, this interpolated reflection response can be used in the standard iterative scheme, as shown in Figure 2.8. Although previous studies found that the resulting Green's and focusing functions contained a relatively high level of noise Haindl (2016), we demonstrate that careful reconstruction of the data can allow for accurate images of the target area. Moreover, these results show less artifacts than the PSF-driven full wavefield Marchenko scheme. The additional pre-processing, however, had a larger computational costs than the proposed full wavefield scheme (e.g. the method with reconstruction beforehand took approximately 24 hours on a single CPU, compared to 3 hours for the full wavefield Marchenko scheme).

2.9. CONCLUSION

One of the restrictions of the Marchenko method is the need for well-sampled and co-located sources and receivers. Recent work introduced new representations for irregularly sampled data. These representations include point-spread functions (PSFs) that deblur distorted focusing- and Green's functions. Based on these representations, this chapter shows that the iterative Marchenko scheme can be adapted to handle irregularly sampled data. For this adaptation the location of the missing sources needs to be known, and an inverse version as opposed to the time-reversed version of the direct arrival of the

Green's function is required as initial estimate of both new schemes. In addition, each iteration of the standard Marchenko scheme is extended by three steps. First, an approximation of the transmission response or quantity Y_1 needs to be computed for the odd and even iterations, respectively. Quantity Y_1 is the inverse of the upgoing focusing function, similar as the transmission response is the inverse of the downgoing focusing function. Second, these approximations are irregularized in accordance with the missing sources. Subsequently, these irregular versions are used to calculate a PSF. Third, the well-sampled focusing- and Green's functions are reconstructed by a multidimensional deconvolution of the blurred original functions with these PSFs.
While the decomposed scheme shows promising initial results, it is established that quantity Y_1 is not necessarily stable. Therefore, a second full wavefield scheme is proposed, which does not rely on the unstable Y_1. This is achieved by combining the two decomposed equations into a single full wavefield equation. This also yields a new iterative full wavefield scheme, which analogous to the first decomposed scheme contains three additional steps compared to the classical Marchenko scheme. Again, these steps resolve and apply a PSF to correct for imperfect sampling in the retrieved responses. A numerical example shows that the full wavefield scheme succeeds in suppressing internal multiples in the final Marchenko image, whereas the classical approach fails to eliminate the internal multiples when imperfectly sampled data are used.
The newly proposed schemes alleviate the need for well-sampled sources when using the Marchenko method. Ideally, the need for well-sampled receivers should be removed as well. While this is subject to ongoing research, a new scheme involving a sparse inversion is envisioned. By relaxing the need for perfectly sampled data, the Marchenko method can be more widely applied to field data.

2.A. DERIVATION OF THE IRREGULAR FULL WAVEFIELD SCHEME

This appendix proposes new representations for irregular sampling in the full wavefield Marchenko scheme. This full wavefield scheme is used instead of the decomposed Marchenko equations, to avoid the use of the unstable inverse of f_1^-. First, Equations 2.1 and 2.2 are combined to get a single Marchenko representation for the full wavefield Green's function, giving (Wapenaar et al., 2014):

$$G(\mathbf{x}_R,\mathbf{x}_A,t) - f_2(\mathbf{x}_A,\mathbf{x}_R,-t) = \int_{\mathbb{S}_0} R(\mathbf{x}_R,\mathbf{x}_S,t) * f_2(\mathbf{x}_A,\mathbf{x}_S,t)\,d\mathbf{x}_S, \tag{2A1}$$

with:

$$f_2(\mathbf{x}_A,\mathbf{x}_R,t) = f_1^+(\mathbf{x}_R,\mathbf{x}_A,t) - f_1^-(\mathbf{x}_R,\mathbf{x}_A,-t). \tag{2A2}$$

Similarly as with the decomposed schemes, the right-hand side integral in Equation 2A1 is approximated by finite summations over the available sources:

$$\sum_i R(\mathbf{x}_R,\mathbf{x}_S^{(i)},t) * f_2(\mathbf{x}_A,\mathbf{x}_S^{(i)},t) * S(t). \tag{2A3}$$

The discretization in Equation 2A3 is the source of the distortions in the case of an imperfectly sampled reflection response.

The next objective is to find a new PSF, that will correct for these distortions. Again, we utilize the fact that a convolution of the focusing focusing with it's reverse produces a band-limited delta pulse. We define response Y_2 as the inverse of f_2 in Equation 2A2, as follows:

$$\delta(\mathbf{x}'_{H,A}-\mathbf{x}_{H,A})\delta(t)=\int_{\mathbb{S}_0} Y_2(\mathbf{x}'_A,\mathbf{x}_S,t)*f_2(\mathbf{x}_A,\mathbf{x}_S,t)d\mathbf{x}_S. \tag{2A4}$$

Alternatively we find:

$$\delta(\mathbf{x}_{H,S}-\mathbf{x}'_{H,S})\delta(t)=\int_{\mathbb{S}_A} f_2(\mathbf{x}_A,\mathbf{x}_S,t)*Y_2(\mathbf{x}_A,\mathbf{x}'_S,t)d\mathbf{x}_A. \tag{2A5}$$

We note that this inverse is more stable than inverse Y_1 of f_1^-, because of the presence of f_1^+ in the definition of f_2. Again the irregular sampling is applied to the integral, resulting in a summation over the irregular sources:

$$\Gamma_2(\mathbf{x}'_A,\mathbf{x}_A,t)=\sum_i Y_2(\mathbf{x}'_A,\mathbf{x}_S^{(i)},t)*f_2(\mathbf{x}_A,\mathbf{x}_S^{(i)},t)*S(t). \tag{2A6}$$

Equation 2A6 is the new PSF for the full wavefield Marchenko representations. This PSF is convolved with the right-hand side of Equation 2A1:

$$\int_{\mathbb{S}_A}\int_{\mathbb{S}_0} R(\mathbf{x}_R,\mathbf{x}_S,t)*f_2(\mathbf{x}'_A,\mathbf{x}_S,t)*\Gamma_2(\mathbf{x}'_A,\mathbf{x}_A,t)d\mathbf{x}_S d\mathbf{x}'_A. \tag{2A7}$$

Next, the order of integration and summation is reversed, and we find, using Equation 2A6, as well as Equation 2A5, and the sifting property of the delta function:

$$\begin{aligned}\sum_i\int_{\mathbb{S}_0} R(\mathbf{x}_R,\mathbf{x}_S,t)*\int_{\mathbb{S}_A} f_2(\mathbf{x}'_A,\mathbf{x}_S,t)*Y_2(\mathbf{x}'_A,\mathbf{x}_S^{(i)},t)d\mathbf{x}'_A*f_2(\mathbf{x}_A,\mathbf{x}_S^{(i)},t)*S(t)d\mathbf{x}_S=\\ \sum_i\int_{\mathbb{S}_0} R(\mathbf{x}_R,\mathbf{x}_S,t)*\delta(\mathbf{x}_{H,S}-\mathbf{x}_{H,S}^{(i)})\delta(t)d\mathbf{x}_S*f_2(\mathbf{x}_A,\mathbf{x}_S^{(i)},t)*S(t)=\\ \sum_i R(\mathbf{x}_R,\mathbf{x}_S^{(i)},t)*f_2(\mathbf{x}_A,\mathbf{x}_S^{(i)},t)*S(t).\end{aligned} \tag{2A8}$$

Note that this is identical to Equation 2A3. Finally, $\int_{\mathbb{S}_A}\{\cdot\}*\Gamma_2 d\mathbf{x}'_A$ is applied to both sides of Equation 2A1, giving:

$$\hat{G}(\mathbf{x}_R,\mathbf{x}_A,t)-\hat{f}_2(\mathbf{x}_A,\mathbf{x}_R,-t)=\sum_i R(\mathbf{x}_R,\mathbf{x}_S^{(i)},t)*f_2(\mathbf{x}_A,\mathbf{x}_S^{(i)},t)*S(t), \tag{2A9}$$

with:

$$\hat{G}(\mathbf{x}_R,\mathbf{x}_A,t)=\int_{\mathbb{S}_A} G(\mathbf{x}_R,\mathbf{x}'_A,t)*\Gamma_2(\mathbf{x}'_A,\mathbf{x}_A,t)d\mathbf{x}'_A, \tag{2A10}$$

and

$$\hat{f}_2(\mathbf{x}_A,\mathbf{x}_R,-t)=\int_{\mathbb{S}_A} f_2(\mathbf{x}'_A,\mathbf{x}_R,-t)*\Gamma_2(\mathbf{x}'_A,\mathbf{x}_A,t)d\mathbf{x}'_A. \tag{2A11}$$

REFERENCES

Broggini, F., Snieder, R., & Wapenaar, K. (2012). Focusing the wavefield inside an unknown 1D medium: Beyond seismic interferometry. *Geophysics*, *77*(5), A25–A28. https://doi.org/10.1190/geo2012-0060.1

Dukalski, M., & de Vos, K. (2017). Marchenko inversion in a strong scattering regime including surface-related multiples. *Geophysical Journal International*, *212*(2), 760–776. https://doi.org/10.1093/gji/ggx434

Haindl, C. (2016). Marchenko imaging of time-lapse seismic with non-repeated acquisition geometries using sparse reconstruction. *MSc. Thesis, ETH Zürich*.

Haindl, C., Broggini, F., Ravasi, M., & van Manen, D.-J. (2018). Using sparsity to improve the accuracy of Marchenko imaging of single and time-lapse seismic given imperfect acquisition. *80th EAGE Conference and Exhibition 2018*. https://doi.org/10.3997/2214-4609.201801660

Peng, H., Vasconcelos, I., Sripanich, Y., & Zhang, L. (2019). On the effects of acquisition sampling on Marchenko-based focusing and primary estimation. *81st EAGE Conference and Exhibition 2019*. https://doi.org/10.3997/2214-4609.201901570

Peng, H., & Vasconcelos, I. (2019). A study of acquisition-related sub-sampling and aperture effects on Marchenko focusing and redatuming. *SEG Technical Program Expanded Abstracts 2019*, 248–252. https://doi.org/10.1190/segam2019-3214965.1

Ravasi, M. (2017). Rayleigh-Marchenko redatuming for target-oriented, true-amplitude imaging. *Geophysics*, *82*(6), S439–S452. https://doi.org/10.1190/geo2017-0262.1

Ravasi, M., Vasconcelos, I., Kritski, A., Curtis, A., da Costa Filho, C. A., & Meles, G. A. (2016). Target-oriented Marchenko imaging of a North Sea field. *Geophysical Journal International*, *205*(1), 99–104. https://doi.org/10.1093/gji/ggv528

Singh, S., Snieder, R., Behura, J., van der Neut, J., Wapenaar, K., & Slob, E. (2015). Marchenko imaging: Imaging with primaries, internal multiples, and free-surface multiples. *Geophysics*, *80*(5), S165–S174. https://doi.org/10.1190/geo2014-0494.1

Slob, E., Wapenaar, K., Broggini, F., & Snieder, R. (2014). Seismic reflector imaging using internal multiples with Marchenko-type equations. *Geophysics*, *79*(2), S63–S76. https://doi.org/10.1190/geo2013-0095.1

Slob, E., & Zhang, L. (2021). Unified elimination of 1d acoustic multiple reflection. *Geophysical Prospecting*, *69*(2), 327–348. https://doi.org/10.1111/1365-2478.13057

Staring, M., Grobbe, N., van der Neut, J., & Wapenaar, K. (2017). Sparse inversion for solving the coupled Marchenko equations including free-surface multiples. *79th EAGE Conference and Exhibition 2017, 2017*. https://doi.org/10.3997/2214-4609.201701130

Staring, M., & Wapenaar, K. (2020). Three-dimensional Marchenko internal multiple attenuation on narrow azimuth streamer data of the Santos Basin, Brazil. *Geophysical Prospecting*, *68*(6), 1864–1877. https://doi.org/10.1111/1365-2478.12964

Staring, M., Pereira, R., Douma, H., van der Neut, J., & Wapenaar, K. (2018). Source-receiver Marchenko redatuming on field data using an adaptive double-focusing method. *Geophysics*, *83*(6), S579–S590. https://doi.org/10.1190/geo2017-0796.1

Thorbecke, J., Slob, E., Brackenhoff, J., van der Neut, J., & Wapenaar, K. (2017). Implementation of the Marchenko method. *Geophysics*, *82*(6), WB29–WB45. https://doi.org/10.1190/GEO2017-0108.1

van der Neut, J., Thorbecke, J., Wapenaar, K., & Slob, E. (2015). Inversion of the multidimensional Marchenko equation. *77th EAGE Conference and Exhibition 2015, 2015*. https://doi.org/10.3997/2214-4609.201412939

van Groenestijn, G. J., & Verschuur, D. J. (2009). Estimating primaries by sparse inversion and application to near-offset data reconstruction. *Geophysics*, *74*(3), A23–A28. https://doi.org/10.1190/1.3111115

van IJsseldijk, J., & Wapenaar, K. (2021). Adaptation of the iterative Marchenko scheme for imperfectly sampled data. *Geophysical Journal International*, *224*(1), 326–336. https://doi.org/10.1093/gji/ggaa463

Vasconcelos, I., Reinicke Urruticoechea, C., & Brackenhoff, J. (2018). Estimating overburden-only transmission waveforms from surface reflection data. *80th EAGE Conference and Exhibition 2018*. https://doi.org/10.3997/2214-4609.201801096

Verschuur, D. J., Berkhout, A. J., & Wapenaar, C. P. A. (1992). Adaptive surface-related multiple elimination. *Geophysics*, *57*(9), 1166–1177. https://doi.org/10.1002/2014JB011262

Wapenaar, K., Thorbecke, J., van der Neut, J., Broggini, F., Slob, E., & Snieder, R. (2014). Marchenko imaging. *Geophysics*, *79*(3), WA39–WA57. https://doi.org/10.1190/geo2013-0302.1

Wapenaar, K., & van IJsseldijk, J. (2020). Discrete representations for Marchenko imaging of imperfectly sampled data. *Geophysics*, *85*(2), A1–A5. https://doi.org/10.1190/geo2019-0407.1

3

EXTRACTING SMALL TIME-LAPSE TRAVELTIME CHANGES IN A RESERVOIR AFTER MARCHENKO-BASED ISOLATION

Geophysical monitoring of subsurface reservoirs relies on detecting small changes in the seismic response between a baseline and monitor study. However, internal multiples, related to the over- and underburden, can obstruct the view of the target response, hence complicating the time-lapse analysis. In order to retrieve a response that is free from over- and underburden effects, the data-driven Marchenko method is used. This method effectively isolates the target response, which can then be used to extract time-lapse changes more precisely. Additionally, the method also reveals target-related multiples that probe the reservoir more than once, which further define the changes in the reservoir. To verify the effectiveness of the method, a numerical example is constructed. This test shows that when using the isolated target response, the observed time differences resemble the expected time differences in the reservoir. Moreover, the results obtained with target-related multiples also benefit from the Marchenko-based isolation of the reservoir. It is, therefore, concluded that this method has the potential to observe dynamic changes in the subsurface with increased accuracy.

This chapter was published as van IJsseldijk, J., van der Neut, J., Thorbecke, J., & Wapenaar, K. (2023). Extracting small time-lapse traveltime changes in a reservoir using primaries and internal multiples after Marchenko-based target zone isolation. *Geophysics*, *88*(2), no 2., R135–R143. https://doi.org/10.1190/geo2022-0227.1 Minor modifications have been applied to keep consistency within this thesis.

3.1. INTRODUCTION

Time-lapse seismic studies are concerned with detecting small changes in the seismic response between a baseline and a monitor study. These changes can either be a difference in amplitude (e.g. Landrø, 2001), a difference in traveltime (e.g. Landrø & Stammeijer, 2004) or a combination of both (e.g. Trani et al., 2011). These time-lapse methods are essential for observing and monitoring subsurface reservoirs, with applications ranging from determining pressure and fluid saturation changes (Landrø, 2001) to monitoring CO_2 injection (Roach et al., 2015) or observing compaction in a reservoir (Hatchell & Bourne, 2005).

In order for these methods to work optimally, it is important that the reservoir response can be clearly identified in the seismic response. In practice, this requirement is not always fulfilled, as multiple reflections from a (highly) reflective overburden can mask the response of the reservoir. It is, therefore, desirable to remove the overburden effects before applying any time-lapse analysis. The Marchenko method is able to redatum a wavefield from the surface of the earth to an arbitrary focal depth in the subsurface while accounting for all orders of multiples (Slob et al., 2014; Wapenaar et al., 2014). This data-driven method can be used to remove all interactions from layers above the selected focal level, hence giving an unobstructed view of the reservoir response. From this new response, the traveltime difference in the reservoir can more precisely be determined.

In addition to removing the overburden, the reservoir response can completely be isolated by also removing the underburden with the Marchenko method (Wapenaar & Staring, 2018). Consequently, not only the primary response of the reservoir is uncovered, but also internal multiples, which traversed through the reservoir more than once, will now also be clearly visible and unobstructed by primaries and multiples outside the target zone. Since these multiples have passed through the reservoir multiple times, the time-lapse traveltime change of the multiples will be larger, hence easier to detect. This is akin to coda-wave interferometry, which exploits the fact that time-lapse changes are exaggerated in the coda due to the longer paths traveled in the medium (Grêt et al., 2005; Snieder et al., 2002).

Inspired by this principle of coda-wave interferometry, Wapenaar and van IJsseldijk (2020) show how correlation of multiples improve the ability to detect small changes in velocity compared to correlation of primaries. This method is then adapted to find changes in laterally varying media (van IJsseldijk & Wapenaar, 2021). In this work we further develop the method in order to account for time-lapse changes in the overburden. First, we revise the theory of isolating the reservoir response with the Marchenko method and review how to extract traveltime changes from this isolated response. Furthermore, we show how multiples traveling through the reservoir can be enhanced, in order to improve the accuracy of the retrieved time shifts. Subsequently, we present a numerical model that will be used to test the methodology. The reservoir response is then isolated from the modeled data, and the traveltime changes of the primary as well as the multiple reflections are calculated. Finally, we discuss the results and possible future improvements to the method.

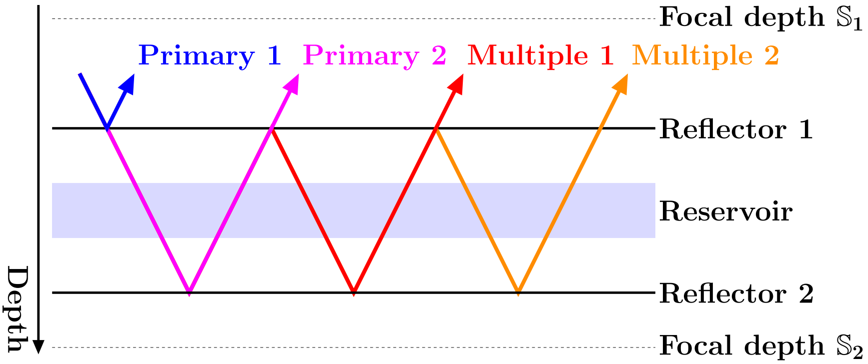

Figure 3.1: Graphic displaying the principle of the method. Note how the reservoir layer is located in between two reflectors. Primary 1 from reflector 1 does not propagate through the reservoir, whereas primary 2 from reflector 2 does. The multiples (1 and 2) are propagating through the reservoir twice or thrice, hence experiencing double or triple the traveltime changes compared to primary 2. Target zone "b" is located in between focal depths $\mathbb{S}_1$ and $\mathbb{S}_2$, overburden "a" and underburden "c" are above and below the target zone, respectively.

3.2. THEORY

Time-lapse seismic experiments aim to resolve the differences between a baseline study at time t_1 and a monitor study conducted at a later time t_2. These differences can be attributed to changes inside of a reservoir and overburden, for example due to production and geomechanical processes. Here we propose a method by which the reservoir response is isolated separately for the baseline and monitor studies, after which cross-correlation between the two studies is used to find the traveltimes differences.

Figure 3.1 shows the principle of the proposed method. Here the acoustic situation is considered, with a reservoir enclosed by two strong reflectors. Note how the primary from the first reflector, does not probe the reservoir, whereas the primary from the second reflector does. Moreover, the internal multiples generated by these reflectors will traverse the reservoir multiple times, hence they experience a larger traveltime shift. In order to achieve this same situation from a regular reflection response measured at the surface, the medium is first divided into 3 parts: overburden "a", target zone "b" which contains the reservoir and two reflectors as in Figure 3.1, and underburden "c". The reflection response of the full medium is denoted by $R_{abc}(\mathbf{x}_R,\mathbf{x}_S,t)$, here $\mathbf{x}_R$, $\mathbf{x}_S$ and t denote the receiver position, source position and time, respectively. Our first aim is to isolate the reflection response R_b of the target zone with the help of the Marchenko method, which will briefly be discussed in the next section.

3.2.1. EXTRAPOLATED MARCHENKO REPRESENTATIONS

At the base of the Marchenko method are the focusing functions ($f_1^{\pm}$) that allow for retrieval of the Green's functions ($G^{-,\pm}$) between the acquisition surface $\mathbb{S}_0$ and a focal level in the subsurface. Here the left superscript $-$ denotes that the wavefield is upgoing at the receiver position (at the focal level) and the right superscript $\pm$ denotes a down- or up-going direction from the source position (at the acquisition surface). Van der Neut and Wapenaar (2016) introduce modified functions that are extrapolated to the surface

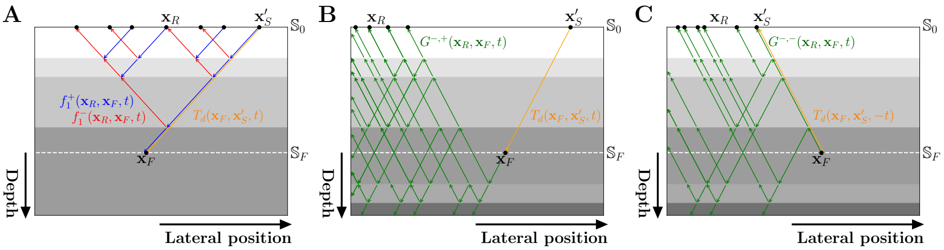

Figure 3.2: Schematic representation of the extrapolated focusing- and Green's functions. (A) The focusing functions f_1^+ (in blue) and f_1^- (in red) are defined in a medium truncated below the focal level ($\mathbb{S}_F$). They are extrapolated to the surface ($\mathbb{S}_0$) using the direct arrival of the transmission response T_d (in orange) to create the extrapolated focusing functions $v^{\pm}$. (B) the downgoing Green's function ($G^{-,+}$) is extrapolated to create $U^{-,+}$. (C) the upgoing Green's function ($G^{-,-}$) creates it's extrapolated counterpart $U^{-,-}$.

by convolution with the direct arrival of the transmission response (T_d). These extrapolated focusing functions ($v^{\pm}$) are defined as follows:

$$v^{\pm}(\mathbf{x}_R,\mathbf{x}'_S,t) = \int_{\mathbb{S}_F} f_1^{\pm}(\mathbf{x}_R,\mathbf{x}_F,t) * T_d(\mathbf{x}_F,\mathbf{x}'_S,t)\,d\mathbf{x}_F. \tag{3.1}$$

Here $\mathbf{x}_F$ is the coordinate of the focusing point at focal depth $\mathbb{S}_F$, $\mathbf{x}'_S$ is a coordinate on the acquisition surface, and $*$ denotes temporal convolution. Note, that except for $\mathbf{x}_F$, all coordinates in this work refer to positions at the surface $\mathbb{S}_0$. Similarly, the extrapolated Green's functions ($U^{-,\pm}$) are defined as:

$$U^{-,\pm}(\mathbf{x}_R,\mathbf{x}'_S,t) = \int_{\mathbb{S}_F} G^{-,\pm}(\mathbf{x}_R,\mathbf{x}_F,t) * T_d(\mathbf{x}_F,\mathbf{x}'_S,\pm t)\,d\mathbf{x}_F. \tag{3.2}$$

These two equations are visualized in Figure 3.2, which shows how the extrapolated functions are related to the original focusing and Green's functions. By using these extrapolated functions the retrieved wavefields derived in the next section will be situated at the surface $\mathbb{S}_0$ and not at focal level $\mathbb{S}_F$ as is the case with the regular Marchenko functions. Finally, the same convolutions are applied to the coupled Marchenko representations to find the extrapolated representations:

$$U^{-,+}(\mathbf{x}_R,\mathbf{x}'_S,t) + v^-(\mathbf{x}_R,\mathbf{x}'_S,t) = \int_{\mathbb{S}_0} R(\mathbf{x}_R,\mathbf{x}_S,t) * v^+(\mathbf{x}_S,\mathbf{x}'_S,t)\,d\mathbf{x}_S, \tag{3.3}$$

$$U^{-,-}(\mathbf{x}_R,\mathbf{x}'_S,-t) + v^+(\mathbf{x}_R,\mathbf{x}'_S,t) = \int_{\mathbb{S}_0} R(\mathbf{x}_R,\mathbf{x}_S,-t) * v^-(\mathbf{x}_S,\mathbf{x}'_S,t)\,d\mathbf{x}_S. \tag{3.4}$$

The reflection response is denoted by R. In this paper, this response will either be the response of the full medium R_{abc} or the response after overburden removal R_{bc}. Moreover, these two equations have four unknowns. In order to solve this system a causality constraint is introduced, which exploits the fact that the focusing and Green's functions are separable in time. In order to apply this constraint, an estimate of the two-way travel time between the focal level and the surface is required. In our case, this is achieved by computing the direct arrival of the Green's function in a smooth velocity model with an

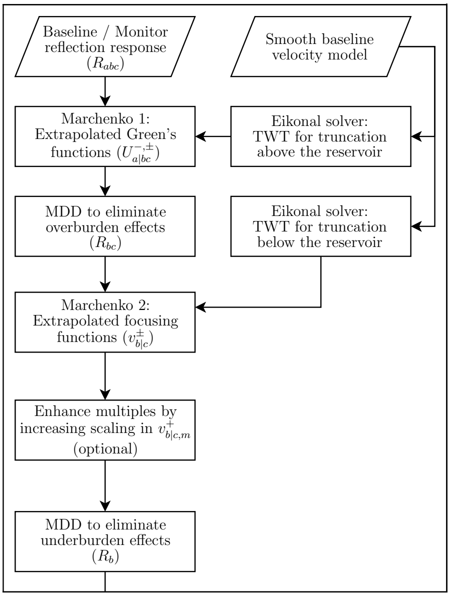

Figure 3.3: Flowchart depicting how the reservoir response is isolated with the Marchenko method.

Eikonal solver, and then convolving this response with itself to find the two-way travel time. A more elaborate derivation of the Marchenko method is beyond the scope of this paper. Instead, the reader is referred to Wapenaar et al. (2021), who give more background on both the regular and extrapolated expressions.

3.2.2. ISOLATION OF THE RESERVOIR'S RESPONSE

Using the relations presented in the previous section, the focusing and Green's functions above and below the reservoir can now be retrieved. From these functions, the reflection response of the target zone can be isolated. First, the overburden is removed, using the extrapolated Green's function between the overburden and the upper boundary $\mathbb{S}_1$ of the target zone (Wapenaar et al., 2021, and Appendix B):

$$U^{-,+}_{a|bc}(\mathbf{x}_R,\mathbf{x}'_S,t) = -\int_{\mathbb{S}_0} U^{-,-}_{a|bc}(\mathbf{x}_R,\mathbf{x}'_R,t) * R_{bc}(\mathbf{x}'_R,\mathbf{x}'_S,t)\,d\mathbf{x}'_R. \tag{3.5}$$

Here $U^{-,\pm}_{a|bc}$ are the extrapolated Green's functions, retrieved with the Marchenko method from Equations 3.3 and 3.4, where R_{abc} is used as reflection response R. The vertical line in the subscript indicates the location of focal level, i.e. between the overburden "a" and the target-zone "b". Equation 3.5 is solved for R_{bc} by multidimensional deconvolution (MDD, Wapenaar et al., 2011). This MDD is achieved with least-squares inversion in the frequency domain. Effectively we have now acquired a new reflection response R_{bc}, which is free from overburden interactions. Furthermore, coordinates $\mathbf{x}'_R$ as well as $\mathbf{x}'_S$ are located at the surface, due to the use of the extrapolated Green's functions. In contrast, previous work with regular Green's functions acquired a redatumed response

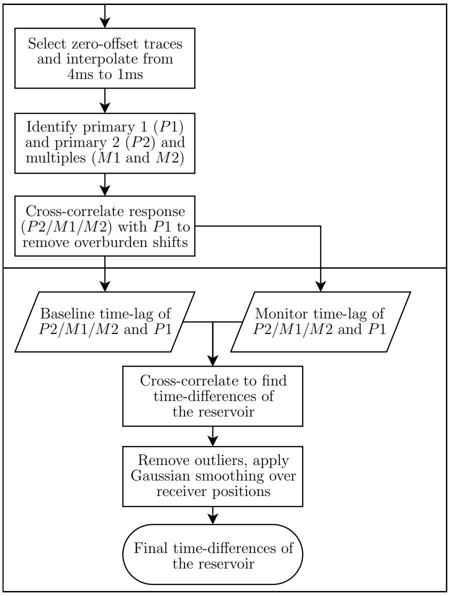

Figure 3.4: Flowchart to get the time differences in the reservoir from the isolated response (continuation of Figure 3.3).

at the focal depth, and then required an additional step to extrapolate this response to the surface (van IJsseldijk & Wapenaar, 2021).

Next, the newly acquired reflection response (R_{bc}) is used to retrieve the extrapolated focusing functions between the target zone and the upper boundary $\mathbb{S}_2$ of the underburden. These focusing functions are then used to remove the underburden (Appendix B):

$$v^-_{b|c}(\mathbf{x}_R, \mathbf{x}'_S, t) = \int_{\mathbb{S}_0} v^+_{b|c}(\mathbf{x}_R, \mathbf{x}'_R, t) * R_b(\mathbf{x}'_R, \mathbf{x}'_S, t) d\mathbf{x}'_R. \tag{3.6}$$

The subscript $b|c$ denotes that R_{bc} was used to retrieve the focusing functions from Equations 3.3 and 3.4, with the focal level between target zone "b" and underburden "c". Note, that Equation 3.6 directly follows from the definition of the focusing functions in the truncated medium (Wapenaar & Staring, 2018). Again, the reflection response of the target zone R_b can be resolved from Equation 3.6 by means of MDD.

Effectively, the target zone response has now been isolated, leaving a response analogous to the situation in Figure 3.1, but with the sources and receivers at the surface $\mathbb{S}_0$.

As a final step the multiples in the final response R_b can be further amplified. First, consider that the multiples in R_b continue infinitely in time, and are constructed from the focusing functions $v^-_{b|c}$ and $v^+_{b|c}$, which are finite in time (i.e. they are confined between $t = 0$ and the two-way travel time to the focal depth). Next, $v^+_{b|c}$ in Equation 3.6 is divided into an initial function $v^+_{b|c,0}$ and a coda $v^+_{b|c,m}$ (Wapenaar et al., 2021):

$$v^+_{b|c}(\mathbf{x}_R, \mathbf{x}'_R, t) = \delta(\mathbf{x}_{H,R} - \mathbf{x}'_{H,R})\delta(t) + v^+_{b|c,m}(\mathbf{x}_R, \mathbf{x}'_R, t). \tag{3.7}$$

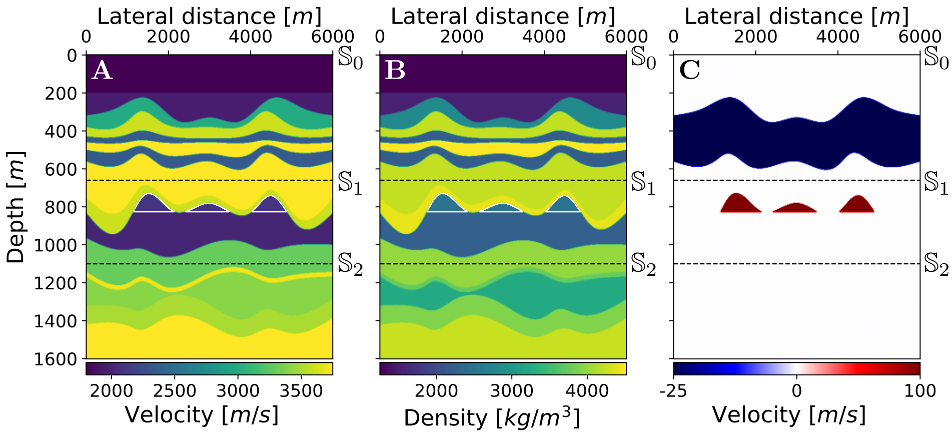

Figure 3.5: Velocity (A) and density (B) model of the baseline study for the numerical example. The black dashed lines define the focal levels above ($\mathbb{S}_1$) and below the reservoir ($\mathbb{S}_2$), used for the Marchenko method. The solid white contour depicts the three different reservoir pockets. C shows the difference in velocity between the baseline and monitor study. The density inside the reservoir pockets is also increasing with 100kg/m^3 for the monitor study, with no density changes outside the reservoir. Primary 1 and Primary 2 originate from the green to blue contrast at 700m to 900m and the blue to green contrast at 1000m, respectively.

Here, δ denotes the Dirac delta function. From this equation it follows that the initial function $v^+_{b|c,0}$ can be interpreted as a (bandlimited) delta pulse at $t = 0$. This pulse is followed by the coda $v^+_{b|c,m}$. Appendix A shows, when solving Equation 3.6 for R_b, that $v^+_{b|c,0}$ is mainly responsible for the primaries in R_b, whereas $v^+_{b|c,m}$ updates these primaries and constructs the subsequent multiples of the response. Therefore, by amplifying $v^+_{b|c,m}$ the multiples in response R_b should get enhanced as well. Note, this enhancement will cause the amplitudes of the response not to be accurate anymore. However, this is not an issue for the current implementation, since only time-shifts are desired. Figure 3.3 shows an overview of the process to isolate the target response. In this chart only a smooth velocity model of the baseline is used. It is assumed that this model can also be used for the monitor study, because the velocity changes are relatively small and only an approximation of two-way traveltime to the focal depth is needed. Next, the new responses R_b for the baseline and monitor will be used to extract the traveltime shifts in the reservoir.

3.2.3. EXTRACTION OF TIME DIFFERENCES

Before extracting the traveltime shifts in the reservoir, the different primaries and multiples are identified. Primary 1 and 2 are easily detected due to the isolation of the target zone (i.e. there are no interactions from the overburden to obscure the primaries). Subsequently, the arrival times of the internal multiples can be approximated based on the primaries, where the arrival time of the n-th multiple can be approximated by the arrival time of primary 2 plus n times the difference in time between the two primaries. The first step is now to eliminate any time shifts resulting from a time-lapse change in the overburden. In order to do this the temporal correlation between primary 1 (i.e. the response that is not penetrating the reservoir) and primary 2 or an internal multiple (i.e. the responses that go through the reservoir) is computed. This gives the correlation between primary 1 and the target response below the reservoir:

$$C_\star(\mathbf{x}_0,\tau) = \int_0^\infty \Theta_{P1}(t+\tau)R_b(\mathbf{x}_0,t+\tau)\Theta_\star(t)R_b(\mathbf{x}_0,t)dt. \tag{3.8}$$

Here, C is the correlation of the two responses, and $\mathbf{x}_0$ denotes the position of the zero-offset traces in the data, where $\mathbf{x}_S = \mathbf{x}_R$. Moreover, the star $\star$ can be replaced with P1, P2, M1 or M2, for primary 1, primary 2, multiple 1 and multiple 2, respectively. This correlation contains the time-lag between the first reflector and P2, M1 or M2. Theta is a time window or mute function that isolates a specific primary or multiple as follows:

$$\Theta_\star(t) = \begin{cases} 1, \text{if } t_\star - \epsilon < t \leq t_\star + \epsilon \\ 0, \text{otherwise.} \end{cases} \tag{3.9}$$

Hence $t_\star$ is the travel time of one of the primaries or multiples. ϵ is a small constant that defines the window, and makes sure the whole waveform is included. Any traveltime differences in the overburden are removed by first calculating the time-lag with primary 1 in Equation 3.8, i.e. the time difference between primary 1 and either P2, M1 or M2 is free from overburden interactions. After the time-lags of Equation 3.8 have been independently calculated for the baseline and monitor study, the time-lapse traveltime shifts in the reservoir can be determined with a second temporal correlation as follows:

$$\Delta t_\star(\mathbf{x}_0) = \underset{\tau}{\arg\max}\left(\int_0^\infty C_\star(\mathbf{x}_0,t+\tau)\bar{C}_\star(\mathbf{x}_0,t)dt\right). \tag{3.10}$$

The bar denotes that the monitor correlation is used, thus the time-lags, of primary 2 or one of the multiples with respect to primary 1, for the baseline and monitor are correlated. Next, the time instant, where the maximum of this correlation occurs, is taken to determine the traveltime differences in the reservoir. The process of extracting the time shifts is summarized in Figure 3.4. Note that there are a few additional practical considerations included in the chart, such as resampling and removing outliers. These will be discussed in more detail in the next section.

3.3. NUMERICAL EXAMPLE

A numerical experiment is designed, to show the viability of the method. The baseline velocity and density models are shown in Figure 3.5 A and B, respectively. Figure 3.5 C displays the change in velocity for the monitor model. In the overburden, there is a velocity decrease of 25 m/s, whereas the velocity and density in the three reservoir compartments increase by 100 m/s and 100 kg/m^3. The reflection responses of the baseline (R_{abc}) and monitor ($\bar{R}_{abc}$) are computed with finite differences, using a wavelet with a flat spectrum between 5 and 80 Hz (Thorbecke & Draganov, 2011). The receivers are placed along a 6000 m long line with a spacing of 10m, and the data are recorded with a sampling rate of 4 ms. The 601 sources are excited at the same positions as the receivers. Estimates of the two-way traveltimes, between the surface and the focal points at 675 m and 1100 m, are acquired using an eikonal solver in a smooth version of the baseline

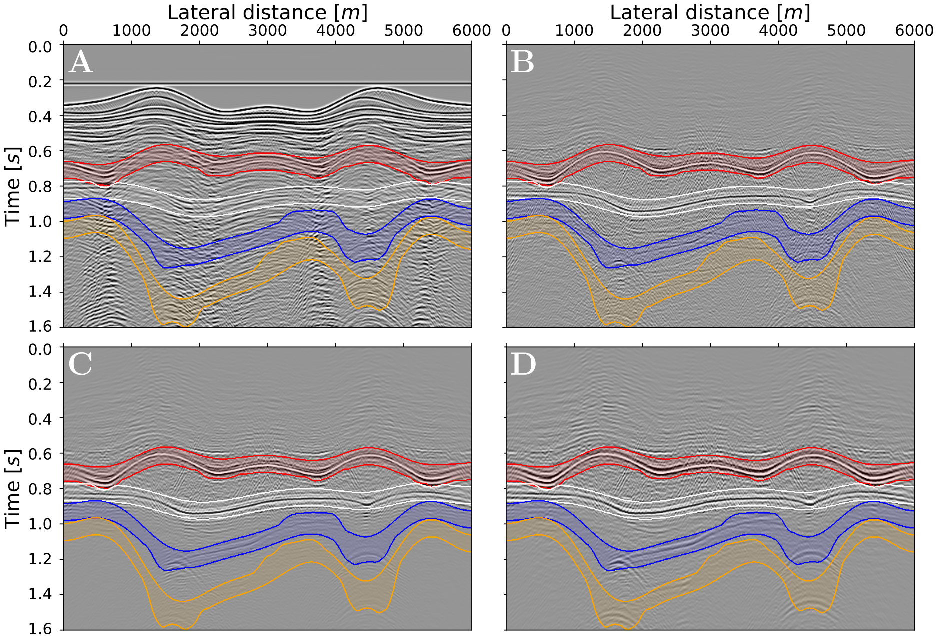

Figure 3.6: Zero-offset gathers for the baseline reflection response of the entire medium R_{abc} (A), after overburden removal R_{bc} (B), after over- and underburden removal R_b (C), after isolation and multiple enhancement of R_b (D). The windows used for cross-correlation for primary 1, primary 2, multiple 1 and multiple 2 are highlighted in red, white, blue and orange, respectively.

velocity model of Figure 3.5A. Lastly, a band-limited delta pulse is computed, which is used as the initial focusing function (v_0^+) in the iterative Marchenko scheme.

3.3.1. RESULTS OF TARGET ZONE ISOLATION

Figure 3.6A shows a zero-offset section of the initial reflection response before applying the multiple internal removal (R_{abc}). Note that only the zero-offset data are shown, but the data at all offsets are available and used to compute the isolated reservoir response R_b from R_{abc}. Due to the highly reflective overburden, the primaries (P1 in red and P2 in white) are nearly impossible to identify, and multiple 1 and 2 (in blue and orange) are completely obscured by the overburden and underburden interactions. After removing the overburden and acquiring R_{bc} (Figure 3.6B), the primaries are now clearly recognizable in the seismogram. However, the windows enclosing the multiples contain undesirable events from primary reflections from the underburden. The third panel (3.6C) reveals that these events are successfully removed after underburden removal. Also, note how the multiple events are enhanced in the fourth display (3.6D). This is the result of the previously described scaling factor applied to $v_{b|c,m}^+$ (which was scaled with a factor 2.5) before retrieving R_b.

All the time windows that select the primaries and multiples in Figure 3.6 are picked from this final response in panel D (R_b). First, the arrival time for both primaries is manually selected. As stated before, these times are then used to provide an estimate for the multiple arrivals. Finally, the windows are manually adjusted to ensure they include the full response from each individual event. In the next section, these windows will be used for the cross-correlations that compute the time differences.

3.3.2. TIME DIFFERENCES INSIDE THE RESERVOIR

From the isolated response, the traveltime changes can be estimated. First, the data are interpolated from 4ms to 1ms to achieve a better time resolution. Second, the primary enclosed in the red window is selected from the data. Similarly, either the second primary, first multiple or second multiple is also extracted using its respective window (as shown in Figure 3.6). For both the baseline and monitor studies, these responses are then correlated to effectively remove the time differences developed in the overburden, i.e. this correlation retrieves the time-lag between P1 and P2, M1 or M2, thus removing the shared path in the overburden. Finally, the baseline and monitor time-lag correlations are mutually correlated to find the time differences in the target zone.

The results of these final correlations are shown in Figure 3.7. These results can be interpreted as the zero-offset time-lag differences between the baseline and monitor surveys. Hence any deviation from $\Delta t = 0$ should represent the time shift within the reservoir. Since the velocity in the reservoir is increasing, a negative Δt is expected, whereas a positive shift indicates a velocity decrease (i.e. with the current model positive Δt would indicate that the result is contaminated with remaining overburden effects). Note that these results were acquired with the true Marchenko scaling without the previously described multiple enhancement. Here, the response of the full medium, the response after overburden removal and the response of the target zone (i.e. after over- and underburden removal) are displayed with blue, orange and green lines, respectively. The light-blue area marks the 1D-based zero-offset traveltime difference, which was computed by multiplying two times the reservoir thickness with the slowness change in the reservoir. However, this reference solution does not take into account lateral variations. The red line gives a second reference solution made by cross-correlating "ideal" data. These data were acquired in a model with a smooth overburden (A), the same target zone (B) as the actual model and a transparent underburden (C). The zero-offset response is then modeled with finite-differences, providing an accurate isolated response of the target zone R_b for both the monitor and baseline response. Subsequently, the primaries and multiples are identified in the modeled zero-offset response, and then correlated as described in flowchart in Figure 3.4.

Figure 3.7A shows the results for primary 2. Although, all three responses capture some differences in the reservoir, the response of the full medium still reflects changes in the overburden as shown by the time-shifts larger than 0ms. These positive time-shifts are almost fully removed after overburden removal. Note that, on the one hand, the correlations do not match the 1D reference very well, because of the lateral variations in the model. On the other hand, the match with correlation of the ideal data (the red line) is a lot better, which implies that the Marchenko based isolation was successful. Based on these results it is concluded that the expected time differences are smaller than 15ms for P1, M1 and M2. This observation is used to achieve more accurate results, by removing outliers that give a time difference larger than 15ms at any lateral distance (i.e. they are

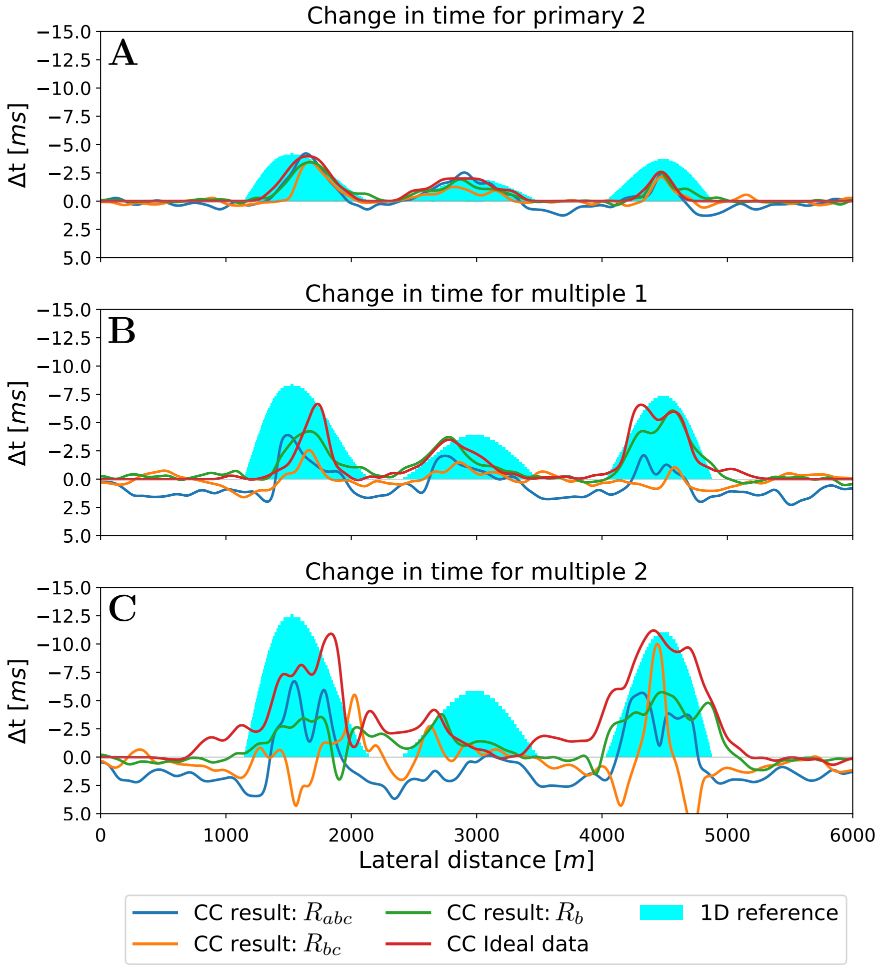

Figure 3.7: Results showing the estimated time difference in the reservoir from primary 2 (A), multiple 1 (B) and multiple 2 (C), no scaling factor has been applied to enhance the multiples. First, the time-lag with primary 1 is computed for the baseline and monitor study. These time-lags are then cross-correlated to find the time differences. In each plot the blue line shows the result derived from the full reflection response (R_{abc}), the orange and green lines are the time difference derived from R_{bc} and R_b, respectively. The red line shows the cross-correlations of the ideal data, where R_b is computed using finite differences. The light blue show the change in time for 1D zero-offset traces (i.e. two times the reservoir thickness times the difference in the slowness).

removed before applying the Gaussian smoothing along the lateral direction in Figure 3.4).

Next, the procedure is applied to multiple 1 and multiple 2, the results of which are shown in figures 3.7B and 3.7C, respectively. This time none of the results match either reference perfectly, and seemingly no meaningful information can be acquired from the multiple 2. However, these results are achieved without any multiple enhancement. In the next section, we will explore how the results can be improved by using multiple enhancement.

3.3.3. RESULTS AFTER MULTIPLE ENHANCEMENT

To improve results, i.e. to get more accurate time-differences, the multiple enhancement is now applied, by scaling $v^+_{b|c,m}$ with a factor of 2.5. This factor was chosen somewhat arbitrarily, but as a rule of thumb the maximum amplitude in the new $v^+_{b|c,m}$ should not exceed 80% of the maximum amplitude in $v^+_{b|c,0}$. The results of the correlations of this new R_b are shown in Figure 3.8. The time differences acquired by correlation with primary 2 (Figure 3.8A) show no significant differences from the original results, but the correlations of the multiples of the isolated response (the green lines in 3.8B and 3.8C) match the "ideal" data (the red lines) a lot better now. On the contrary, when looking at the results for the multiple 1 (Figure 3.8B), a clear dissimilarity is observed between the results of the isolated response in green and the full response in blue. Furthermore, note the improvement relative to results obtained with primary 2 at 4500 m lateral distance, where the correlation matches the 1D reference a lot better. The same can be seen in the results of multiple 2 in Figure 3.7C. The two other reservoir compartments at 1500 m and 3000 m do not present the same improvements, instead, their results confirm the observations for the correlations with primary 2.

Especially, the results for primary 2 and multiple 1 (the green lines in 3.8A and 3.8B) accurately match the correlation of the "ideal" data. The results of multiple 2 do not have the same match. This is due to the fact that events from multiple 1 are interfering within the correlation window of multiple 2 for the "ideal" data, and leaving an imprint on the reference solution. From this match with the "ideal" data, it can be concluded that the Marchenko method succeeded in correctly isolating the target response, as the results for multiple 1 coincide with the reference solution. This also highlights the importance of isolating the response, since the correlations of the multiples in R_{abc} and R_{bc} do not come close to the reference solution at all. Finally, the results outside the reservoir compartments should show a time differences equal to 0 ms, and time differences larger than 0 ms indicate that the result is contaminated by effects from the overburden.The correlation results of the isolated response R_b display less of these positive time differences compared to the results of the full response R_{abc}. Consequently, this is another confirmation that the isolation process has successfully eliminated the effects of the overburden.

3.4. DISCUSSION

Although the results show that the reservoir response can successfully be isolated and accurate time differences can be retrieved from both the primary reflection and the internal multiples, there are a number of issues that require a more in-depth discussion. In addition to this discussion, future improvements and practical considerations for the implementation on real data will be considered as well.

First, the scaling factor to $v^+_{b|c,m}$, introduced to amplify multiple events, was found experimentally. The authors conducted numerous 1D experiments to get a better under-

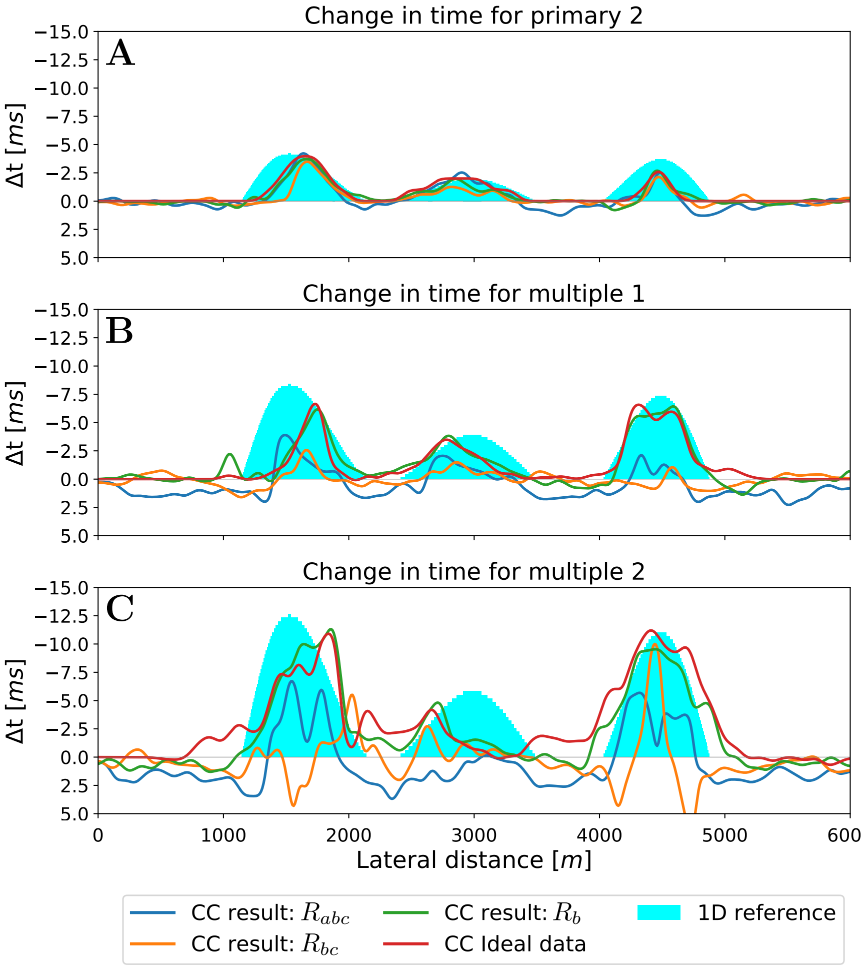

Figure 3.8: Same results as Figure 3.7, but with multiple enhancement by applying a scaling factor of 2.5 to $v^+_{b|c,m}$ before retrieving R_b with MDD. Note that the multiple correlations of the isolated response R_b (the green lines in 3.8B and 3.8C) are a lot closer to the ideal result (the red lines) compared to the results without multiple enhancement (figures 3.7B and 3.7C).

standing of the effect of the scaling factor, and found that the scaled $v^+_{b|c,m}$ should not exceed the maximum amplitude in $v^+_{b|c,0}$, in order to maintain a stable result, with as a rule of thumb the amplitudes preferably staying below 80% of this maximum. Due to these nuances it is always advised to obtain the results without any multiple enhancement first, and only make an effort to improve the results with multiple enhancement after this initial result is achieved.

A second point of discussion is the order of operations used to isolate the target response. In theory, it does not matter whether the underburden is removed before or after overburden removal. Numerical experiments indeed showed that removing the underburden before the overburden is also a viable approach to isolate the target response, by first retrieving R_{ab} from a MDD of $v^{\pm}_{ab|c}$ and then R_b from $U^{-,\pm}_{a|b}$. However, the previously discussed multiple enhancements are no longer available when the method is applied in this order, because the MDD of the focusing functions would be applied before the MDD of the Green's functions that require proper scaling. Therefore, it was decided to start with overburden elimination followed by removal of the underburden.

Third, the method is designed to use as little a priori information as possible, needing solely three prerequisites: the baseline reflection response (R_{abc}), the monitor reflection response ($\bar{R}_{abc}$) and a smooth version of the baseline velocity model. The smooth velocity model is used to approximate the two-way travel time between the surface and the focal depth. The same model can be used for both the baseline and monitor reflection response because it is assumed that the velocity changes in the medium are relatively small. When the velocity changes are large, a separate velocity model is required to isolate the target zone from the monitor reflection response, but the application of the method would not change otherwise.

In this work the time shifts are retrieved by a simple cross-correlation method. Instead of cross-correlation, a waveform-based or other method could be used to possibly improve the accuracy of the time shift results further. MacBeth et al. (2020) give a comprehensive overview of the different available methods to calculate time shifts.

Next, the primary results before the target zone isolation already match the actual results quite closely, and only minor deviations due to overburden effects are present (i.e. the parts where $\Delta t > 0$ ms). However, these results indirectly benefit from the isolated result, because the windows, which are used to identify the primaries, are selected from the isolated results (Figure 3.6C). Moreover, previous results by van IJsseldijk and Wapenaar (2021) show that the correlations from R_{abc} are insufficient to get accurate time differences in less complex models with overburden events interfering with the primaries.

Application of the Marchenko algorithm to field data can be quite cumbersome. Especially the MDD that is used to remove the overburden effects tends to be very sensitive to errors in the amplitude of the data. To overcome this limitation, Staring et al. (2018) introduce a double-focusing method, which is more stable but leaves some remaining interactions of the overburden. A similar approach is envisioned to acquire R_{bc}, when applying this method to real data. It is noted, however, that any errors in R_{bc} will affect the final result of R_b as well. Moreover, the Marchenko method is quite sensitive to wrong amplitudes in field data. In order to overcome this limitation either a scaling factor can be determined using cost functions (Brackenhoff, 2016) or an advanced 3D to 2D conversion can be applied (Dukalski & Reinicke, 2022).

Finally, we would ideally find the velocity change of the reservoir rather than the time differences. For very simple situations a similar approach as coda-wave interferometry can be considered, which finds the velocity perturbation from the change in traveltime and initial velocity (Snieder, 2006). However, this only holds when the relative velocity perturbation is constant at every location. In our case, the perturbation is different outside the reservoir, hence the relation does not hold. Alternatively, the velocity perturbation can be found by inversion of cross-correlations at all offsets (instead of just the zero-offset data used here). Compared to the traveltime differences, the velocity changes can more directly be related to physical processes such as flow in the reservoir. Currently, this is subject to ongoing research.

3.5. CONCLUSION

A good understanding of fluid flow, temperature variations and mechanical changes in subsurface reservoirs is essential for a large variety of geoscientific methods. These dynamic changes can be observed with seismic time-lapse methods by identifying amplitude changes, time shifts or both, between a baseline and a monitor study. However, the response of a subsurface target can be obscured by interferences from reflectors in the overburden and/or underburden, making it harder to detect the time-lapse effects. The Marchenko method can be used to remove primaries as well as internal multiples above or below an arbitrary focal level in the subsurface from the reflection response. Hence, this method can be used to isolate the reservoir response in both the baseline and monitor response, enabling an unobstructed examination of changes in the target zone.

A twofold methodology has been proposed to extract time differences. With this methodology, first the target response is isolated, by overburden removal, followed by underburden removal. This new response is then used to identify the primary and multiple reflections in the target zone. Second, time differences are retrieved by cross-correlating the different reflections of the baseline and monitor studies. By first correlating the response with primary 1 above the reservoir, all possible time shifts of the overburden are removed.

A numerical example with a strongly reflective overburden was created to test the methodology. The isolation of the target zone revealed the primary responses of the reservoir, allowing their extraction from the data. Next, the time differences of the reservoir could be approximated from correlations with a primary reflection below the reservoir. Furthermore, additional traveltime changes were retrieved from the first and second-order multiples, created by the two reflectors enclosing the reservoir. These multiples confirmed the earlier observations, but also improved specific blind spots in the original approximation of the time changes.

The proposed methodology provides a new means to extract traveltime differences, especially for situations where complex overburden and underburden interactions mask the target response. Future developments should also make it possible to invert for velocity changes in the reservoir, rather than time differences. The method will then enable us to more accurately observe dynamic changes in the subsurface.

3.A. MULTIPLE ENHANCEMENTS BY RESCALING FOCUSING FUNCTION CODA

This appendix aims to give a more comprehensive explanation as to why increasing the weight of $v^+_{b|c,m}$, results in enhanced multiples in the final reflection response R_b. First operator $\mathcal{V}^+_m$ is defined to apply a multidimensional convolution with $v^+_{b|c,m}$, as follows:

$$\mathcal{V}^+_m R_b(\mathbf{x}_R,\mathbf{x}'_S,t) = \int_{\mathbb{S}_0} v^+_{b|c,m}(\mathbf{x}_R,\mathbf{x}'_R,t) * R_b(\mathbf{x}'_R,\mathbf{x}'_S,t)\,d\mathbf{x}'_R. \tag{3A1}$$

Next, this equation and Equation 3.7 are substituted in Equation 3.6. After rearranging the terms, an expression to obtain R_b is acquired:

$$R_b(\mathbf{x}_R,\mathbf{x}'_S,t) = \left(1+\mathcal{V}_m^+\right)^{-1} v^-_{b|c}(\mathbf{x}_R,\mathbf{x}'_S,t). \tag{3A2}$$

Finally, the inverse in Equation 3A2 can be expanded as a Neumann series:

$$R_b(\mathbf{x}_R,\mathbf{x}'_S,t) = \sum_{k=0}^{\infty} \left(-\mathcal{V}_m^+\right)^k v^-_{b|c}(\mathbf{x}_R,\mathbf{x}'_S,t). \tag{3A3}$$

Equation 3A3 illustrates how the primaries and multiples in R_b are constructed from the focusing functions. First, for $k = 0$ only the contributions from $v^-_{b|c}$ are available. This will account for the primaries and multiples contained in R_b from times $t = 0$ up to times below the two-way traveltime to the focal depth, since $v^-_{b|c}$ is equal to zero outside this range. Consequently, the multiples at times larger than the two-way traveltime have to be constructed from terms with $k > 0$, which will be created using $v^+_{b|c,m}$. This implies that the multiples in R_b can artificially be enhanced by amplifying $v^+_{b|c,m}$. Application of Equation 3A3 is only stable if the L2 norm of the operator is less then 1, i.e. $||\mathcal{V}_m^+||_2^2 < 1$. This constraint does not necessarily hold for all subsurface models. Because of this limitation the Neumann series is solely introduced here to provide an intuitive explanation for the multiple enhancement, whereas the MDD in Equation 3.6 is solved by least-squares inversion in the frequency domain.

REFERENCES

Brackenhoff, J. (2016). *Rescaling of incorrect source strength using Marchenko redatuming* [Master's thesis, TU Delft repository, Delft University of Technology] [http://resolver.tudelft.nl/uuid:0f0ce3d0-088f-4306-b884-12054c39d5da, accessed 11 August 2022].

Dukalski, M., & Reinicke, C. (2022). Marchenko Multiple Elimination using conventional vs advanced 3-D to 2-D conversion on marine data. *83rd EAGE Annual Conference & Exhibition, 2022*. https://doi.org/10.3997/2214-4609.202210182

Grêt, A., Snieder, R., Aster, R. C., & Kyle, P. R. (2005). Monitoring rapid temporal change in a volcano with coda wave interferometry. *Geophysical Research Letters*, *32*(6). https://doi.org/10.1029/2004GL021143

Hatchell, P. J., & Bourne, S. J. (2005). Measuring reservoir compaction using time-lapse timeshifts. *SEG Technical Program Expanded Abstracts 2005*, 2500–2503. https://doi.org/10.1190/1.2148230

Landrø, M. (2001). Discrimination between pressure and fluid saturation changes from time-lapse seismic data. *Geophysics*, *66*(3), 836–844. https://doi.org/10.1190/1.1444973

Landrø, M., & Stammeijer, J. (2004). Quantitative estimation of compaction and velocity changes using 4D impedance and traveltime changes. *Geophysics*, *69*(4), 949–957. https://doi.org/10.1190/1.1778238

MacBeth, C., Amini, H., & Izadian, S. (2020). Review paper: Methods of measurement for 4D seismic post-stack time shifts. *Geophysical Prospecting*, *68*(9), 2637–2664. https://doi.org/10.1111/1365-2478.13022

Roach, L. A. N., White, D. J., & Roberts, B. (2015). Assessment of 4D seismic repeatability and CO2 detection limits using a sparse permanent land array at the Aquistore CO2 storage site. *Geophysics*, *80*(2), WA1–WA13. https://doi.org/10.1190/geo2014-0201.1

Slob, E., Wapenaar, K., Broggini, F., & Snieder, R. (2014). Seismic reflector imaging using internal multiples with Marchenko-type equations. *Geophysics*, *79*(2), S63–S76. https://doi.org/10.1190/geo2013-0095.1

Snieder, R. (2006). The theory of coda wave interferometry. *Pure and Applied Geophysics*, *163*(2), 455–473. https://doi.org/10.1007/s00024-005-0026-6

Snieder, R., Grêt, A., Douma, H., & Scales, J. (2002). Coda wave interferometry for estimating nonlinear behavior in seismic velocity. *Science*, *295*(5563), 2253–2255. https://doi.org/10.1126/science.1070015

Staring, M., Pereira, R., Douma, H., van der Neut, J., & Wapenaar, K. (2018). Source-receiver Marchenko redatuming on field data using an adaptive double-focusing method. *Geophysics*, *83*(6), S579–S590. https://doi.org/10.1190/geo2017-0796.1

Thorbecke, J. W., & Draganov, D. (2011). Finite-difference modeling experiments for seismic interferometry. *Geophysics*, *76*(6), H1–H18. https://doi.org/10.1190/geo2010-0039.1

Trani, M., Arts, R., Leeuwenburgh, O., & Brouwer, J. (2011). Estimation of changes in saturation and pressure from 4D seismic AVO and time-shift analysis. *Geophysics*, *76*(2), C1–C17. https://doi.org/10.1190/1.3549756

van der Neut, J., & Wapenaar, K. (2016). Adaptive overburden elimination with the multidimensional marchenko equation. *Geophysics*, *81*(5), T265–T284. https://doi.org/10.1190/geo2016-0024.1

van IJsseldijk, J., van der Neut, J., Thorbecke, J., & Wapenaar, K. (2023). Extracting small time-lapse traveltime changes in a reservoir using primaries and internal multiples after Marchenko-based target zone isolation. *Geophysics*, *88*(2), no 2., R135–R143. https://doi.org/10.1190/geo2022-0227.1

van IJsseldijk, J., & Wapenaar, K. (2021). Discerning small time-lapse traveltime changes by isolating the seismic response of a reservoir using the Marchenko method. *First International Meeting for Applied Geoscience & Energy Expanded Abstracts*, 3449–3453. https://doi.org/10.1190/segam2021-3583007.1

Wapenaar, K., & van IJsseldijk, J. (2020). Employing internal multiples in time-lapse seismic monitoring, using the Marchenko method. *82nd EAGE Annual Conference & Exhibition, 2020*. https://doi.org/10.3997/2214-4609.202011576

Wapenaar, K., Brackenhoff, J., Dukalski, M., Meles, G., Reinicke, C., Slob, E., Staring, M., Thorbecke, J., van der Neut, J., & Zhang, L. (2021). Marchenko redatuming, imaging, and multiple elimination and their mutual relations. *Geophysics*, *86*(5), WC117–WC140. https://doi.org/10.1190/geo2020-0854.1

Wapenaar, K., & Staring, M. (2018). Marchenko-based target replacement, accounting for all orders of multiple reflections. *Journal of Geophysical Research: Solid Earth*, *123*(6), 4942–4964. https://doi.org/10.1029/2017JB015208

Wapenaar, K., Thorbecke, J., van der Neut, J., Broggini, F., Slob, E., & Snieder, R. (2014). Marchenko imaging. *Geophysics*, *79*(3), WA39–WA57. https://doi.org/10.1190/geo2013-0302.1

Wapenaar, K., van der Neut, J., Ruigrok, E., Draganov, D., Hunziker, J., Slob, E., Thorbecke, J., & Snieder, R. (2011). Seismic interferometry by crosscorrelation and by multidimensional deconvolution: a systematic comparison. *Geophysical Journal International*, *185*(3), 1335–1364. https://doi.org/10.1111/j.1365-246X.2011.05007.x

4

A FRAMEWORK FOR SUBSURFACE MONITORING BY INTEGRATING RESERVOIR SIMULATION WITH TIME-LAPSE SEISMIC SURVEYS

Reservoir simulations for subsurface processes play an important role in successful deployment of geoscience applications such as geothermal energy extraction and geo-storage of fluids. These simulations provide time-lapse dynamics of the coupled poromechanical processes within the reservoir and its over-, under-, and side-burden environments. For more reliable operations, it is crucial to connect these reservoir simulation results with the seismic surveys (i.e., observation data). However, despite being crucial, such integration is challenging due to the fact that the reservoir dynamics alters the seismic parameters. In this work, a coupled reservoir simulation and time-lapse seismic methodology is developed for multiphase flow operations in subsurface reservoirs. To this end, a poromechanical simulator is designed for multiphase flow and connected to a forward seismic modeller. This simulator is then used to assess a novel methodology of seismic monitoring by isolating the reservoir signal from the entire reflection response. This methodology is shown to be able to track the development of the fluid front over time (i.e. where one fluid phase is being displaced by an other phase), even in the presence of a highly reflective overburden with strong time-lapse variations. These results suggest that the proposed methodology can contribute to a better understanding of fluid flow in the subsurface. Ultimately, this will lead to improved monitoring of reservoirs for underground energy storage or production.

This chapter was published as van IJsseldijk, J., Hajibeygi, H., & Wapenaar, K. (2023a). A framework for subsurface monitoring by integrating reservoir simulation with time-lapse seismic surveys. *Scientific Reports*, *13*, 13661. https://doi.org/10.1038/s41598-023-40548-0
Minor modifications have been applied to keep consistency within this thesis.

4.1. INTRODUCTION

Understanding fluid flow in subsurface reservoirs is crucial to predict underground processes related to the energy transition, such as geothermal energy (Barbier, 2002), temporary storage of green gasses like hydrogen (Kumar et al., 2022), and long-term storage of greenhouse gasses like CO_2 (Wang et al., 2022). Reservoir simulations allow us to accurately predict fluid flow inside a reservoir, based on a combination of geological, geophysical and borehole data (Fanchi, 2005; Peaceman, 2000). Geophysical methods, such as seismic monitoring, are able to observe time-lapse changes of dynamic properties like pressure and fluid saturation, everywhere in a three-dimensional subsurface. Seismic monitoring relies on the fact that changes in the reservoir will translate into changes in the seismic reflection response. The fluid flow inside the reservoir can then be imaged by comparing a baseline seismic survey with a monitor survey, recorded over the same location at a later point in time (Johnston, 2013; Landrø, 2001; Lumley, 2001; Tura & Lumley, 1998).

Feasibility studies aim to assess the seismic detectability of fluid movement inside a hydrocarbon reservoir (Lumley et al., 1994) or migration of injected CO_2 for CCS projects (Macquet et al., 2019; Pevzner et al., 2011). These types of studies rely on reservoir simulations to predict the movement of the fluids in the reservoir. Although this methodology provides accurate estimates of the time-lapse changes inside the reservoir, it does not predict geomechanical changes in the overburden. However, these changes can have large effects on the repeatability of time-lapse experiments, as overburden time-shifts might be mistaken for changes inside the reservoir (Calvert, 2005). Generally, an independent geomechanical model is used to compute the time-lapse changes in the layers above the reservoir (Hatchell et al., 2005; MacBeth & Bachkheti, 2021). Recently, multiphase poromechanical models were introduced as an all-in-one solution to link fluid flow, transport and deformation in the subsurface (White et al., 2019). Traditionally, these models are used to predict induced seismicity due to fluid injection in the subsurface (Castiñeira et al., 2016; Han et al., 2021; Jha & Juanes, 2014). Additionally, poromechanical simulations can, in theory, also be used to model both time-lapse changes inside the reservoir and overburden at once for seismic monitoring applications.

In addition to time-lapse overburden effects, static overburden effects can also obstruct the reservoir signal in the baseline and monitor seismic surveys, due to the presence of highly reflective layers in the overburden. Both the static and dynamic overburden effects can be accounted for by isolating the reservoir response (van IJsseldijk et al., 2023b; Wapenaar & van IJsseldijk, 2020). This isolation is based on the 3D Marchenko equations that describe all orders of multiple scattering inside the medium (Broggini et al., 2012; Slob et al., 2014; Wapenaar et al., 2014). After this Marchenko-based isolation is applied to the seismic data, the reflections related to the reservoir are clearly visible in the seismic response. Next, the primary reflection from the top of the reservoir is used as a reference event that contains all the delays of the overburden. This reference event is then combined with events originating from the reservoir's base to retrieve time-lapse differences that are solely dependent on the changes inside the reservoir (van IJsseldijk et al., 2023b).

In this work, a poromechanical simulator is proposed to model time-lapse changes in density and compressional velocity due to fluid injection in a subsurface reservoir.

Since multiphase fluid flow as well as geomechanics are included in the formulation, the changes in the overburden and reservoir are modelled all at once. Next, the velocities and densities are computed at a number of time-steps during the simulation, which are used to model the seismic response for the seismic baseline and different monitor studies. Finally, time-lapse changes are retrieved. These changes are then independently assessed both before and after isolation of the reservoir response from the total seismic response (i.e. the response of the overburden, reservoir and underburden). In the next section, we will first discuss the governing equations behind the poromechanical model, the connection with seismic parameters and the retrieval of time-lapse traveltime differences. Secondly, the methodology is tested on a simple as well as a complex model. To conclude, we discuss the results and possible future improvements and extensions to the method.

4.2. METHODS

This section discusses the background on how time-lapse changes can be extracted from a modelled reservoir. The constitutive equations related to poromechanics are first reviewed, then these equations are related to seismic properties, which can be used to model the seismic response at different times in the simulation. These responses are compared to one another to find seismic time-lapse traveltime differences between the different surveys.

4.2.1. MULTIPHASE POROMECHANICS

The geomechanical changes in an isotropic subsurface are represented by the conservation of momentum (Equation 4.1 (Wang, 2001)), and conservation of mass describes flow of immiscible fluids through a reservoir (Equation 4.2 and 4.3 (Aziz & Settari, 1979)). This gives the following system of equations:

$$\nabla \cdot \boldsymbol{\sigma} = \mathbf{f}, \tag{4.1}$$

$$\frac{\partial m_\alpha}{\partial t} + \nabla \cdot (\rho_\alpha \mathbf{v}_\alpha) = \rho_\alpha q_\alpha, \tag{4.2}$$

$$\frac{\partial m_\beta}{\partial t} + \nabla \cdot (\rho_\beta \mathbf{v}_\beta) = \rho_\beta q_\beta. \tag{4.3}$$

Here, m, ρ, $\mathbf{v}$ and q, are the fluid mass per unit volume, density, velocity and sinks/sources, respectively. The subscripts α and β denote two different fluid phases. Furthermore, t denotes time, $\boldsymbol{\sigma}$ is the stress tensor, and $\mathbf{f}$ stands for the body forces acting on the system. Next, the stress tensor in Equation 4.1 is connected to the changes in fluid pressure and displacement according to Biot's theory of poroelasticity (Biot, 1941). Moreover, the mass per unit volume of each phase is related to it's saturation, density and the porosity (i.e. $m = \phi S \rho$). Finally, Darcy's law is used to write the fluid velocity in terms of phase mobility and pore pressure. After applying all these conditions, the system of equations 4.1-4.3 now reads (White et al., 2019):

$$\nabla \cdot \left(\mathbb{C}_{dr} : \nabla^s \mathbf{u} - b p_f \mathbf{I}\right) = \mathbf{f}, \tag{4.4}$$

$$\frac{\partial \phi S_\alpha \rho_\alpha}{\partial t} - \nabla \cdot (\boldsymbol{\lambda}_\alpha \rho_\alpha \nabla p_f) = \rho_\alpha q_\alpha, \tag{4.5}$$

$$\frac{\partial \phi S_\beta \rho_\beta}{\partial t} - \nabla \cdot (\boldsymbol{\lambda}_\beta \rho_\beta \nabla p_f) = \rho_\beta q_\beta. \tag{4.6}$$

In Equation 4.4 b denotes Biot's coefficient, $\nabla^s \mathbf{u} = 0.5(\nabla \mathbf{u} + \nabla \mathbf{u}^T)$ is the symmetric gradient operator operating on displacement $\mathbf{u}$, $\mathbf{I}$ is a unit tensor and $\mathbb{C}_{\text{dr}}$ the rank-4 drained elasticity tensor, which for isotropic linear elastic material reads:

$$\mathbb{C}_{\text{dr},ijkl} = \lambda_{\text{dr}} \delta_{ij} \delta_{jk} + G_{\text{dr}} (\delta_{ik} \delta_{jl} + \delta_{il} \delta_{jk}). \tag{4.7}$$

Here, δ_{ij} is Kronecker's delta, λ Lamé's first parameter, and G Lamé's second parameter or the shear modulus. The subscript dr denotes that the elastic moduli are drained. p_f in equations 4.4-4.6 represents the pore pressure, which in the absence of capillary forces is the same for each phase. In Equation 4.5 and 4.6 S indicates the saturation, for two-phase flow $S_\beta = 1 - S_\alpha$. Moreover, $\boldsymbol{\lambda}$ depicts the phase mobility, which is equal to the rock permeability times the relative permeability over the viscosity $(\mathbf{K} k_r / \mu)$. Lastly, ϕ is the porosity, which differss from a reference ϕ_0 due to the fluid pressure and volumetric strain $\epsilon_v = \text{trace}(\nabla^s \mathbf{u})$ as (Coussy, 2004):

$$\Delta \phi = b \Delta \epsilon_v + \frac{(b - \phi_0)(1 - b)}{K_{\text{dr}}} \Delta p_f, \tag{4.8}$$

with drained bulk modulus $K_{\text{dr}} = \lambda_{\text{dr}} + (2/3) G_{\text{dr}}$.

4.2.2. SEISMIC PARAMETERS VIA FLUID SUBSTITUTION

After the dynamic fluid and geomechanic quantities have been computed by the poromechanical simulation, they have to be converted into seismic parameters, namely density and compressional wave velocity. Note that, in this study, only compressional waves are considered for the forward seismic modelling, even though retrieving the shear wave velocity is trivial once all elastic parameters are calculated. This is due to current limitations of the Marchenko-based isolation of the reservoir response, as the Marchenko equations are not straightforwardly applied to elastic theory (Reinicke et al., 2020), but extensions are under investigation (da Costa Filho et al., 2014; Reinicke & Wapenaar, 2019). The saturated density can be calculated using the fluid saturation and density as well as the porosity and rock density:

$$\rho_{\text{sat}} = (1 - \phi) \rho_{\text{rock}} + \phi (\rho_\alpha S_\alpha + \rho_\beta S_\beta). \tag{4.9}$$

Next, the compressional wave velocity c_p is computed using the elastic moduli K and G as well as density ρ:

$$c_p = \sqrt{\frac{K_{\text{sat}} + \frac{4}{3} G_{\text{sat}}}{\rho_{\text{sat}}}}, \tag{4.10}$$

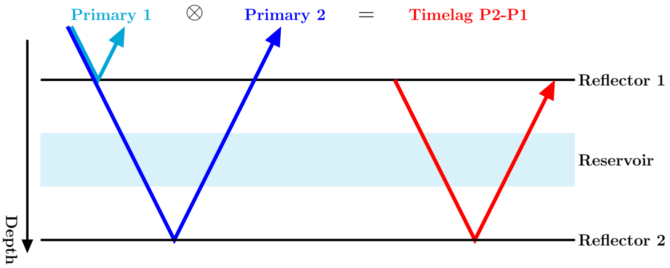

Figure 4.1: Principle of seismic interferometry: a reservoir is situated between two reflectors that reflect primaries 1 and 2. Cross-correlating these primaries cancels their common path, hence only the timelag between the two reflections remains (i.e. the traveltime through the reservoir).

where the subscript sat denotes a saturated medium. Gassmann's equation describes how the saturated bulk and shear moduli can be found (Biot, 1956; Gassmann, 1951):

$$K_{\mathrm{sat}} = K_{\mathrm{dr}} + \frac{(1 - K_{\mathrm{dr}}/K_0)^2}{\phi/K_{\mathrm{fl}} + (1-\phi)/K_0 - K_{\mathrm{dr}}/K_0^2}, \tag{4.11}$$

$$G_{\mathrm{sat}} = G_{\mathrm{dr}}. \tag{4.12}$$

Again, K_{dr} and G_{dr} are the drained bulk and shear modulus, respectively (Mavko et al., 2009). K_0 is the bulk modulus of the minerals of the rock that can be experimentally determined (e.g. Angel et al., 2009; Prasad et al., 2002). K_{fl} is effective bulk modulus of the fluid that can, for example, be calculated using the Reuss method for uniform saturation (Reuss, 1929):

$$K_{\mathrm{fl}} = \frac{1}{S_\alpha \kappa_\alpha + S_\beta \kappa_\beta}, \tag{4.13}$$

where κ is the compressibility of the fluid, which is equal to the inverse of the bulk modulus ($\kappa = 1/K$), and can be derived from the pressure, volume and temperature of the fluid (e.g. Rackett, 1970). Note that Equation 4.11 and 4.12 are only valid at low frequencies (< 100 Hz), which makes them ideal for field-scale experiments such as in this study (Mavko et al., 2009).

4.2.3. EXTRACTING TIME-LAPSE TRAVELTIME DIFFERENCES

First, the subsurface is divided in three units, overburden a, target zone b and underburden c. The reservoir is located in the target zone. Next, the velocity and density explained in the previous section are used to model the seismic reflection response $R_{abc}(\mathbf{x}_R, \mathbf{x}_S, t)$ of the entire subsurface, specified by the subscript abc. The source and receiver coordinates at the surface are indicated with $\mathbf{x}_S$ and $\mathbf{x}_R$, respectively. Additionally, t denotes the seismic recording time, which is different from the flow simulation time in Equation 4.5 and 4.6. The seismic recording time is typically in the order of seconds, whereas the flow simulation time is in the order of hours to days. Reflections in the overburden can interfere with the signal from the reservoir, which can prevent the accurate retrieval of time-lapse differences. Therefore, the reservoir response has to be isolated from the full

response. This isolated response $R_b(\mathbf{x}_R, \mathbf{x}_S, t)$ is free from over- and underburden reflections, which allows accurate retrieval of the time-lapse differences inside the reservoir (van IJsseldijk et al., 2023b). Details of this isolation are discussed in the supplementary material accompanying this paper.
Correlations are a popular method to extract time-lapse traveltime differences from seismic data (MacBeth et al., 2020; Snieder et al., 2002). The traveltime differences Δt can be found by cross-correlating the same signal between a baseline and monitor survey and taking the time instance of the maximum of the correlation:

$$\Delta t_{P2}(\mathbf{x}_0) = \arg\max_{\tau} \left(\int_0^{\infty} C_{P2}(\mathbf{x}_0, t+\tau) \bar{C}_{P2}(\mathbf{x}_0, t)\, dt \right). \tag{4.14}$$

In Equation 4.14, $\mathbf{x}_0$ represents the zero-offset coordinate, where $\mathbf{x}_S = \mathbf{x}_R$. Moreover, C_{P2} denotes the event to be correlated of the baseline survey, and $\bar{C}_{P2}$ the same event in the monitor survey. Note, that no multiples are considered in this chapter, hence the use of C_{P2} as opposed to $C_\star$ in Appendix 3. If this event is simply a primary originating from a reflector below the reservoir, all the time-delays of the overburden will be present in the calculated traveltime differences. Instead a control reflection from above the reservoir can be used to first compute the timelag inside the reservoir (van IJsseldijk et al., 2023b). In Figure 4.1 this idea is systematically depicted; primary 1 does not travel through the reservoir, while primary 2 does. By cross-correlating these two primaries the timelag in the reservoir is computed, while all time-delays from the overburden are cancelled out. This is akin to the idea of seismic interferometry (Wapenaar et al., 2010). Equation 4.15 describes how correlation of primaries 1 ($P1$) and 2 ($P2$) returns the correlation (C_{P2}) between these two events:

$$C_{P2}(\mathbf{x}_0, \tau) = \int_0^{\infty} P1(\mathbf{x}_0, t+\tau) P2(\mathbf{x}_0, t)\, dt. \tag{4.15}$$

If the timelag in Equation 4.15 is computed for both the baseline and monitor survey, the retrieved correlations can be inserted into Equation 4.14 in order to acquire time-lapse traveltime differences that only encompass the changes in the reservoir layer. A similar procedure can be applied to multiples, selected from the isolated target response R_b. Since multiples have traveled through the reservoir layer multiple times, they are more responsive to time-lapse changes in the reservoir (van IJsseldijk et al., 2023b). In the following, only primaries are considered.

4.3. NUMERICAL EXAMPLES

A customised fully implicit multiphase poromechanics simulator was designed for this work. The poromechanics part of this simulator was benchmarked on the 1D Terghazi and 2D Mandel problems (Mandel, 1953; Terzaghi et al., 1996). Furthermore, the two-phase fluid flow simulation was validated using the DARSim Matlab simulator (Cusini, 2019). The simulation considers two immiscible fluids without capillary pressures, and uses a quadratic model to estimate the phase relative permeability. The simulator also includes fluid substitution to find saturated elastic parameters and produce subsurface density and velocity models for seismic modelling. Forward seismic modelling was achieved with an existing finite-difference modeller (Thorbecke & Draganov, 2011), and

Table 4.1: Properties for each layer and fluid for the first numerical example, layers are displayed on the left of Figure 4.2. The asterisk indicates the reservoir layer. In this table the elastic parameters are represented by the Poisson ratio $\nu = \lambda/(2\lambda + 2G)$ and Young's modulus $E = (G(3\lambda + 2G))/(\lambda + G)$.

layer #	ν [−]	E [GPa]	K_0 [GPa]	ϕ [−]	ρ_{rock} [kg/m^3]
1	0.24	10	25	0.4	3150
2	0.21	14	20	0.25	2800
3	0.31	14	5	0.15	3500
4	0.26	15	50	0.1	3000
5	0.2	11	50	0.3	2800
6	0.3	12	33	0.2	2800
7	0.25	6	5	0.15	2400
8*	0.15	29	30	0.3	3000
9	0.19	15	42	0.15	3100
10	0.25	32	70	0.3	4400
11	0.3	50	10	0.15	5000
12	0.2	60	50	0.2	6000

fluid	μ [Pa · s]	κ [GPa^{-1}]	ρ_{fluid} [kg/m^3]
α	$1 \cdot 10^{-3}$	0.5	1035
β	$5 \cdot 10^{-4}$	1	750

Marchenko-based isolation of the target response was performed with publicly available algorithms (van IJsseldijk et al., 2023b). In this section two models are considered. The first example is a simple piston-like flow in a homogeneous reservoir with simple overburden. Second, a more heterogeneous model is considered with a highly reflective overburden.

4.3.1. Case 1: Simple model

The subsurface model for this numerical experiment is shown in Figure 4.2, and the values for the properties of each layer and fluid can be found in Table 4.1. The simulation has 401 and 801 gridpoints in the depth and lateral dimensions, leading to grid cells of 5 m^2. This discretization was chosen to ensure stability of both the multiphase poromechanical and the seismic simulations. A smaller grid-size would lead to an unstable fluid flow simulation, whereas a larger grid-size would cause dispersion in the seismic modeller. To start the simulation fluid α is injected on the left side of the reservoir (initially filled with fluid β) with a constant pressure of 50 MPa, and the production wells, in line with the right side of the reservoir, have a pressure of 5 MPa, while the initial pressure in the reservoir is equal to 10 MPa. The fluid flow is constrained to the reservoir, and roller boundary conditions (i.e. zero normal displacement) are imposed on the four edges of the model. The total simulation time is 600 days, and a seismic survey is modelled at every 100th day. The forward seismic model utilizes a zero-phase wavelet with a flat spectrum between 5 and 70 Hz, a time sampling of 4 ms, and 401 co-located sources and receivers at a spacing of 10 m.

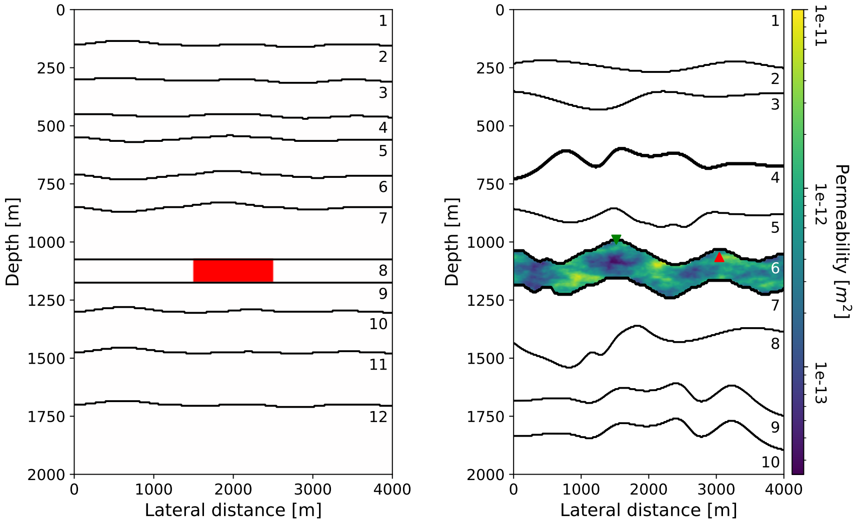

Figure 4.2: Subsurface model for the first (left) and second (right) numerical example. The reservoir for the first numerical example (in red) has a constant permeability of $1 \cdot 10^{-13}$ m^2, and fluid is injected at the left border of the reservoir and produced at the right border. For the second example the reservoir (in colour) has a variable permeability between $2.5 \cdot 10^{-14}$ and $1 \cdot 10^{-11}$ m^2. The green and red triangles indicate the location of the injection and production well, respectively (which are now a single point source or sink). Other relevant properties of the numbered layers can be found in Table 4.1 for the first model, and Table 4.2 for the second model.

Figure 4.3 shows the time-lapse change in P-wave velocity after 200 days compared to the baseline (a), as well as the zero-offset reflectivity modelled at this time step (b). In Figure 4.3a, a decrease in velocity is noted above the injector wells (caused by the time-lapse response of the soft layer on top of the reservoir), whereas the velocity increases above the production wells and inside the reservoir. Inside the reservoir an increase in velocity is noticed due to fluid β being replaced with fluid α. The changes in P-wave velocity above the reservoir are caused by the pressure change, that is, the increase in pressure due to injection leads to a decrease in velocity; vice versa the pressure decrease above the production wells causes an increase in velocity. Furthermore, primary 1 and primary 2, at the top and base of the reservoir are clearly visible in the seismic reflectivity section, as indicated by the red and blue arrows in Figure 4.3b. Due to this clear visibility, no Marchenko-based isolation is necessary for the simple model. Next, reflectivity is modelled for every 100th day between 0 and 600 days. The initial reflectivity at day 0 is used as baseline study and the subsequent reflection responses are considered monitor studies.

After the simulation and forward seismic modelling is finished, the correlation of $P1$ and $P2$ (i.e. the reflection inside the reservoir) is first computed for each of seismic study using Equation 4.15. To further improve the resolution of the results, the correlations are interpolated to 0.5 ms, by padding the data with zeros in the frequency domain. These correlations are then used to find the traveltime differences between the baseline and

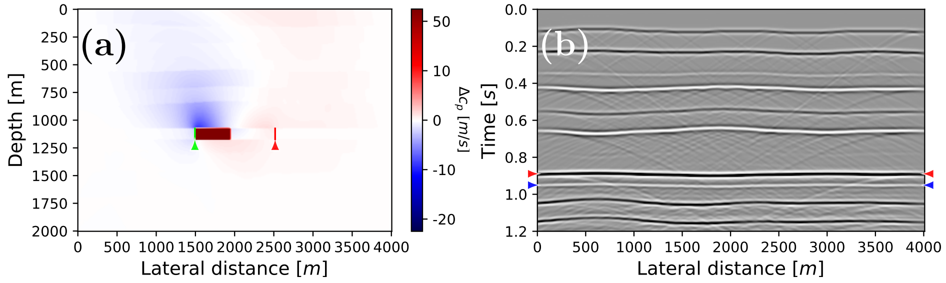

Figure 4.3: Time-lapse difference in P-wave velocity between 0 and 200 days of simulation (a) and zero-offset reflection response after 200 days of simulating fluid injection (b). In (a) the injection and production wells are marked with the green and red lines, respectively. In (b) the arrows mark primary 1 (red) and primary 2 (blue). These primaries delineate the reservoir and will be used to extract traveltime differences.

monitor studies (Equation 4.14). The results of this numerical experiment are shown in Figure 4.4. The dashed lines in the figure show the reference result based on the time-lapse changes in velocity. The solid lines are time-lapse traveltime differences retrieved with the proposed method. These lines clearly mark the fluid front advancing from left to right in the reservoir. The lines do not perfectly coincide with the reference result due to limitations in the spatial and temporal resolution of the seismic responses, which were measured with a time sampling of 4 ms and a receiver spacing of 5 m. Finally, to illustrate the effect of the overburden, the dotted line shows the traveltime differences computed solely from reflection $P2$ of the baseline and monitor data after 200 days. This is in contrast to the solid lines where reflections $P1$ and $P2$ are first correlated, and this correlation is then used to compute the traveltime changes between the baseline and monitor study. This means that the dotted lines do not retrieve the correlation of Equation 4.15, but rather insert reflector $P2$ of the baseline and monitor study directly into Equation 4.14. All overburden changes are, therefore, included in the dotted line, hence the location of the fluid front can no longer be accurately observed (i.e. it deviates from the reference result).

4.3.2. CASE 2: COMPLEX MODEL

The second numerical experiment examines a more complex model shown on the right in Figure 4.2, with all layer and fluid parameters listed in Table 4.2. This model contains a highly reflective overburden, designed to produce strong multiple reflections that interfere with the reservoir response (van IJsseldijk & Wapenaar, 2021). Additionally, this also means that the overburden yields a strong response due to geomechanical changes. Furthermore, the reservoir is no longer rectangular, instead it has a wave-like structure with variable permeabilities between $2.5 \cdot 10^{-14}$ and $1 \cdot 10^{-11}$ m^2. This permeability is pseudo random, generated using Perlin noise that allows for a somewhat coherent distribution (Perlin, 1985). As shown in Figure 4.2, a single injector well (50 MPa) is located at the top of the reservoir at 1500 m lateral distance, alongside with a production well at 3000 m with a pressure of 5 MPa. The boundary conditions are the same as in the simple model. Every 50th day of simulation the reflection response is modelled, the total sim-

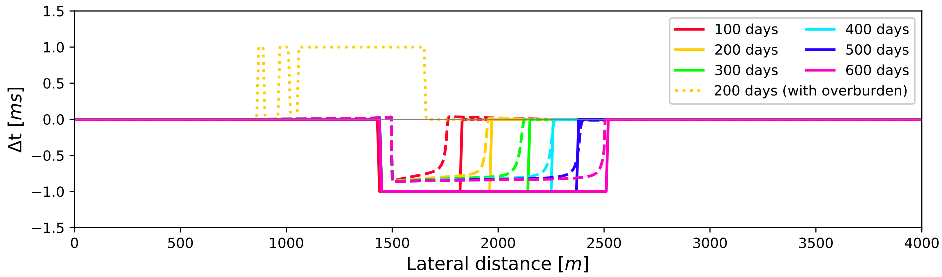

Figure 4.4: Traveltime differences between the baseline and monitor study at different times of the reservoir simulation for the simple model. The dashed lines represent the actual differences, whereas the solid lines are the differences extracted from the modelled seismic response. To highlight the importance of removing overburden effects, the dotted line shows the traveltime differences after 200 days when primary 2 (below the reservoir) is immediately correlated in the baseline and monitor study. Opposed to this, for the solid lines the overburden effects are first removed using primary 1 (above the reservoir) as reference, and only thereafter the baseline and monitor study are correlated to get the time-lapse changes inside the reservoir.

Table 4.2: Properties for each layer and fluid for the second numerical example, layers are displayed on the right of Figure 4.2. The asterisk indicates the reservoir layer.

layer	ν	E	K_0	ϕ	ρ_{rock}
#	[−]	[GPa]	[GPa]	[−]	[kg/m^3]
1	0.23	6	25	0.4	2917
2	0.24	8	20	0.25	4333
3	0.16	3	5	0.15	1470
4	0.25	11.5	50	0.25	4667
5	0.27	2.5	33	0.1	1333
6*	0.25	7	5	0.3	2487
7	0.4	15	30	0.3	4285
8	0.31	15	70	0.15	3176
9	0.24	20	10	0.1	3333
10	0.35	22.5	200	0.15	4705

fluid	μ	κ	ρ_{fluid}
	[Pa · s]	[GPa^{-1}]	[kg/m^3]
α	$1 \cdot 10^{-3}$	0.5	1035
β	$5 \cdot 10^{-4}$	1	750

ulation time is 300 days. The seismic modelling uses the same parameters as in the first numerical example, except for the spectrum of the source wavelet, which is flat between 5 and 50 Hz.

The evolution of the saturation is shown in the left column of Figure 4.5. This figure also displays the changes in velocity for 6 monitor time steps, which shows that the time-lapse changes outside the reservoir overpower the changes inside the reservoir. Again, the velocity decreases and increases above the injection and productions wells, respectively. Figure 4.6 displays the zero-offset seismic sections of the initial baseline and final

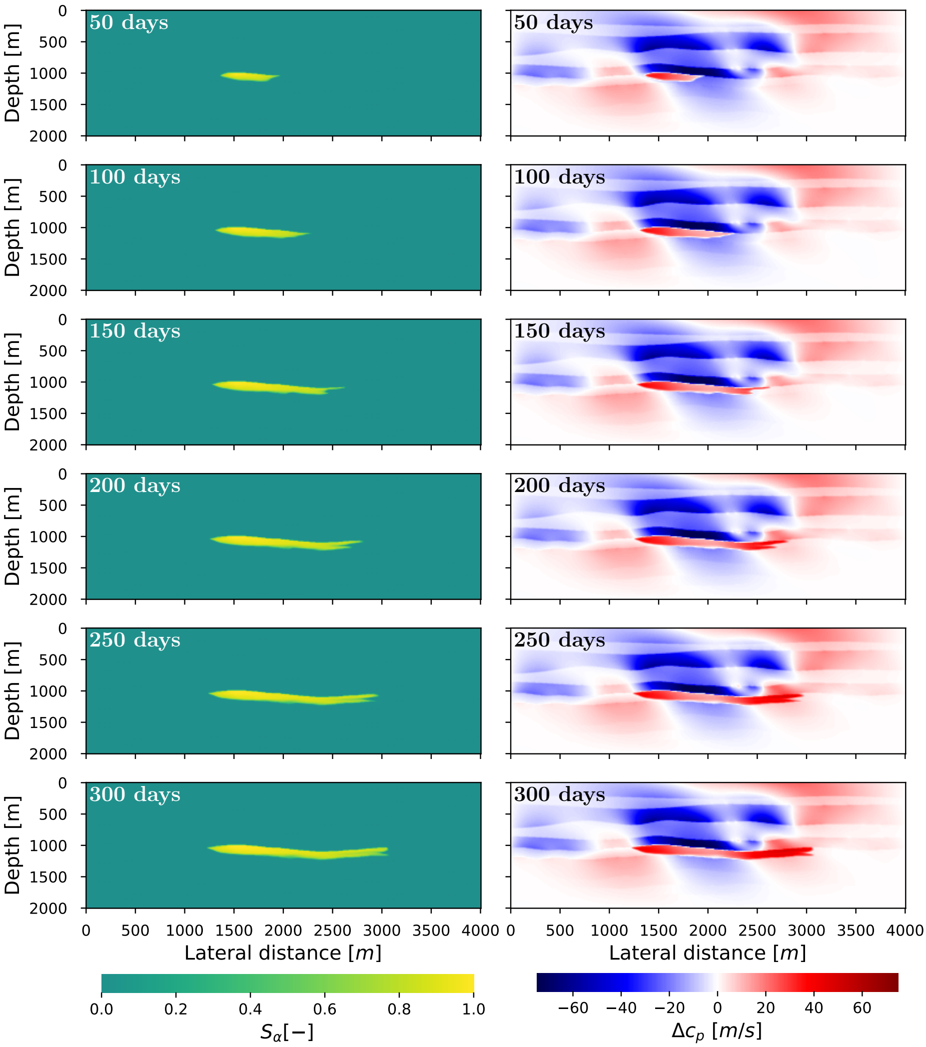

Figure 4.5: Change in saturation (left column) and P-wave velocity (right column) over time. On the right side the blue and red colours indicate a decrease and increase in velocity, respectively.

monitor studies at 0 and 300 days, respectively. Figure 4.6a and 4.6b show that the two primary reflections (marked in red and blue) are obscured by overburden events. As seen in Figure 4.6c the time-lapse differences from the reservoir are masked by overburden effects. Consequently, it is beneficial to isolate the reservoir response, contrary to the first example. The results of this isolation are shown in 4.6d, 4.6e and 4.6f. The desired events (i.e. $P1$ and $P2$) are now revealed in the reflection response. Similarly, the isolation is applied to the remaining monitor surveys as well as the baseline survey. Next, the correlations are interpolated from 4 to 1 ms via the frequency domain for improved

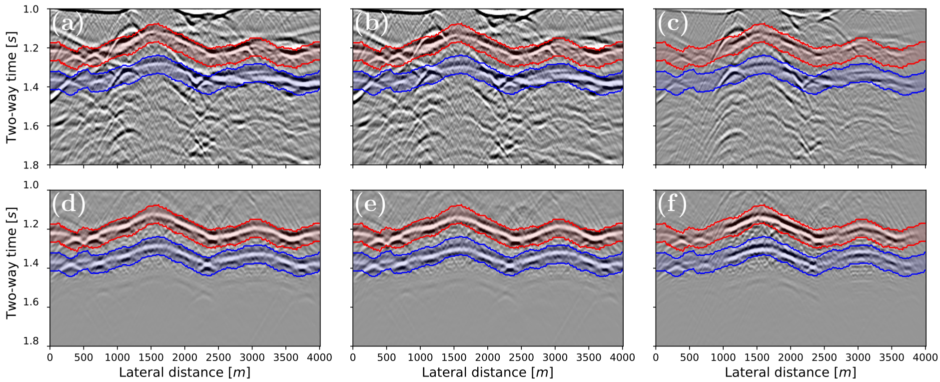

Figure 4.6: Zero-offset reflectivity at after 0 (left column), 300 days (middle column) and their difference (right column), zoomed in on 1 to 1.8 s of recording time. The top and bottom rows show the full (R_{abc}) and isolated (R_b) response, respectively. The primary at the top of the reservoir ($P1$) is marked in red, and the primary at the base of the reservoir ($P2$) in blue. Note that these primaries are only clearly visible in the isolated responses.

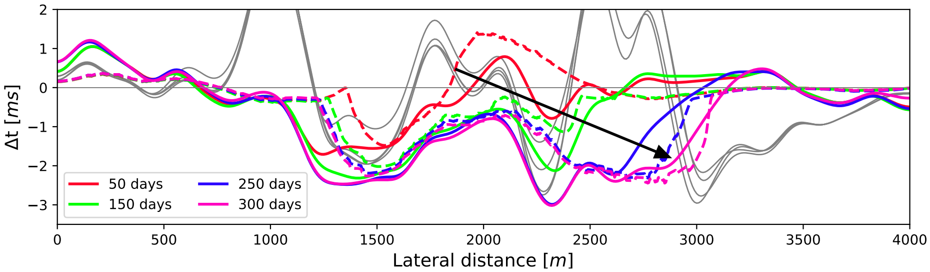

Figure 4.7: Traveltime differences at different times of the reservoir simulation for the complex model. The dashed lines represent the actual differences, and are included as a reference solutions, whereas the solid lines are the differences extracted from the seismic data after Marchenko-based isolation (i.e. Figure 4.6d and 4.6e). The black arrow indicates the general direction of the fluid front over time. The gray lines show the travel differences extracted from the full response, that is before Marchenko-based isolation (Figure 4.6a and 4.6b).

resolution. Subsequently, the correlations between $P1$ and $P2$ are computed, which will be used to find the time differences of the reservoir layer.

Once again, the time-lapse traveltime differences inside the reservoir are computed according to Equation 4.14; the results of this procedure are plotted with solid lines in Figure 4.7. As before, the dashed lines depict the reference result calculated based on the velocity changes in Figure 4.5. However, their behaviour is a lot more complex than the previous results. The solid, coloured lines represent the traveltimes difference computed from the correlations of $P1$ and $P2$ of the baseline and monitor surveys. Lastly, the gray lines show the results of computing the time-differences from the full medium responses (i.e. without isolation, Figure 4.6a and 4.6b), these results clearly deviate from the reference solution due to overburden effects appearing in the selection window of the primaries. Even though the computed differences somewhat agree with the reference solution, the match is significantly poorer than for the simple model. Especially around 2200 m the results strongly differ from the reference solution, as all 4 solid lines underestimate the reference indicated with the dashed lines. This underestimation is also observed in the gray lines in the background, and could, therefore, indicate that some remainder of overburden effects is still present in the isolated response. Nevertheless, the results after applying the reservoir isolation (i.e. the solid coloured lines) show a clear improvement in recovering the trend of the fluid movement compared to the solid gray lines. Further improvements may be possible using a migration technique to collapse the diffractions to their true location, thus improving the spatial resolution of the data.

4.4. DISCUSSION

In the previous section it was shown that poromechanical modelling can add valuable insights to seismic reservoir monitoring, specifically because overburden changes are predicted together with fluid flow. In this section possible improvements upon both the poromechanical and the seismic part of the method are discussed.

Firstly, poromechanical simulations are computationally expensive, which sets practical limitations on their use. Currently, the simulation takes around 8 hours, when using 8 CPUs on the Delft High Performance Computer (Delft High Performance Computing Centre (DHPC), 2022). However, this time dramatically increases on a grid with finer discretization. One solution to this problem is to apply a preconditioner to improve convergence of the equations, allowing to still achieve high resolution simulations (White et al., 2019). Alternatively, a multiscale approach could be used in order to limit the size of the problem, thus speeding up the simulations (Cusini et al., 2016; HosseiniMehr et al., 2018; Sokolova et al., 2019).

Additionally, the simulator could be improved by extending the formulations to include fractures. This is especially relevant as fractures can unexpectedly block the fluid or bypass impermeable zones. Another feature that is currently missing from the simulator is the ability to model cyclic storage, which is required to accurately monitor temporary storage of hydrogen or other gasses in the subsurface (Ramesh Kumar et al., 2021). It would also be interesting to include a third fluid to the simulator, in order to account for solution and dissolution of gasses into fluid due to the pressure changes inside the reservoir.

In the current seismic study, only timelapse time-differences were considered. Future developments should also consider seismic amplitude variations of the signal. Recent work investigated how angle-dependent amplitude information can be retrieved with the Marchenko method (Alfaraj et al., 2020). Ideally, a combination of both amplitude and traveltime differences is used to recover the dynamic fluid parameters from the seismic data (Trani et al., 2011).

4.5. CONCLUSION

This work developed a multiphase poromechanical simulator that is directly coupled with a seismic survey simulator, through the update of the seismic parameters. This integrated simulator allows to instantly resolve time-lapse changes not only inside the reservoir but also in its overburden. The simulator was used to test the feasibility of a novel methodology to extract time-lapse travel time changes after Marchenko-based isolation of the reservoir response. This methodology solves the repeatability issue of time-lapse seismic surveys by identifying and utilizing a reference reflection above the reservoir. Future developments should focus on inverting the seismic time-lapse changes back to the dynamic reservoir properties, in order to close the loop between reservoir simulations and seismic monitoring.

These results are a significant step to achieve higher resolution monitoring of subsurface reservoirs. A better understanding of fluid flow in these reservoirs will improve predictions of underground processes related to geothermal energy, subsurface storage of gasses like hydrogen, and sequestration of CO_2.

REFERENCES

Alfaraj, H., Brackenhoff, J., & Wapenaar, K. (2020). Obtaining angle-dependent reflectivity using the Marchenko redatuming method. *82nd EAGE Annual Conference & Exhibition*. https://doi.org/10.3997/2214-4609.202012138

Angel, R. J., Jackson, J. M., Reichmann, H. J., & Speziale, S. (2009). Elasticity measurements on minerals: A review. *European Journal of Mineralogy*, *21*(3), 525–550. https://doi.org/10.1127/0935-1221/2009/0021-1925

Aziz, K., & Settari, A. (1979). *Petroleum reservoir simulation*. Springer Netherlands. https://doi.org/10.2118/9781613999646

Barbier, E. (2002). Geothermal energy technology and current status: An overview. *Renewable and Sustainable Energy Reviews*, *6*(1), 3–65. https://doi.org/10.1016/S1364-0321(02)00002-3

Biot, M. A. (1941). General theory of three-dimensional consolidation. *Journal of applied physics*, *12*(2), 155–164. https://doi.org/10.1063/1.1712886

Biot, M. A. (1956). Theory of propagation of elastic waves in a fluid-saturated porous solid. II. Higher frequency range. *The Journal of the Acoustical Society of America*, *28*(2), 179–191. https://doi.org/10.1121/1.1908239

Broggini, F., Snieder, R., & Wapenaar, K. (2012). Focusing the wavefield inside an unknown 1D medium: Beyond seismic interferometry. *Geophysics*, *77*(5), A25–A28. https://doi.org/10.1190/geo2012-0060.1

Calvert, R. (2005). 4D technology: Where are we, and where are we going? *Geophysical Prospecting*, *53*(2), 161–171. https://doi.org/10.1111/j.1365-2478.2004.00469.x

Castiñeira, D., Jha, B., & Juanes, R. (2016). Uncertainty Quantification and Inverse Modeling of Fault Poromechanics and Induced Seismicity: Application to a Synthetic Carbon Capture and Storage (CCS) Problem. *U.S. Rock Mechanics/Geomechanics Symposium*.

Coussy, O. (2004). *Poromechanics*. John Wiley & Sons. https://doi.org/10.1002/0470092718

Cusini, M. (2019). *Dynamic multilevel methods for simulation of multiphase flow in heterogeneous porous media* [Doctoral dissertation, Delft University of Technology]. https://doi.org/10.4233/uuid:c624cd58-25e0-4bf9-bf36-025e08c46169

Cusini, M., van Kruijsdijk, C., & Hajibeygi, H. (2016). Algebraic dynamic multilevel (ADM) method for fully implicit simulations of multiphase flow in porous media. *Jour-*

nal of Computational Physics, *314*, 60–79. https://doi.org/10.1016/j.jcp.2016.03.007

da Costa Filho, C. A., Ravasi, M., Curtis, A., & Meles, G. A. (2014). Elastodynamic Green's function retrieval through single-sided Marchenko inverse scattering. *Phys. Rev. E*, *90*, 063201. https://doi.org/10.1103/PhysRevE.90.063201

Delft High Performance Computing Centre (DHPC). (2022). DelftBlue Supercomputer (Phase 1) [https://www.tudelft.nl/dhpc/ark:/44463/DelftBluePhase1].

Fanchi, J. R. (2005). *Principles of applied reservoir simulation*. Elsevier.

Gassmann, F. (1951). Uber die elastizitat poroser medien. *Vierteljahrsschrift der Naturforschenden Gesellschaft in Zurich*, *96*, 1–23.

Han, Z., Ren, G., & Younis, R. M. (2021). Unified reservoir and seismic simulation with explicit representation of fractures and faults. *SPE Reservoir Simulation Conference*. https://doi.org/10.2118/203979-MS

Hatchell, P., Kawar, R., & Savitski, A. (2005). Integrating 4D seismic, geomechanics and reservoir simulation in the Valhall oil. *67th EAGE Annual Conference & Exhibition*. https://doi.org/10.3997/2214-4609-pdb.1.C012

HosseiniMehr, M., Cusini, M., Vuik, C., & Hajibeygi, H. (2018). Algebraic dynamic multilevel method for embedded discrete fracture model (F-ADM). *Journal of Computational Physics*, *373*, 324–345. https://doi.org/10.1016/j.jcp.2018.06.075

Jha, B., & Juanes, R. (2014). Coupled multiphase flow and poromechanics: A computational model of pore pressure effects on fault slip and earthquake triggering. *Water Resources Research*, *50*(5), 3776–3808. https://doi.org/10.1002/2013WR015175

Johnston, D. H. (2013). *Practical applications of time-lapse seismic data*. Society of Exploration Geophysicists.

Kumar, K. R., Honorio, H. T., & Hajibeygi, H. (2022). Simulation of the inelastic deformation of porous reservoirs under cyclic loading relevant for underground hydrogen storage. *Scientific Reports*, *12*(1), 21404. https://doi.org/10.1038/s41598-022-25715-z

Landrø, M. (2001). Discrimination between pressure and fluid saturation changes from time-lapse seismic data. *Geophysics*, *66*(3), 836–844. https://doi.org/10.1190/1.1444973

Lumley, D. E. (2001). Time-lapse seismic reservoir monitoring. *Geophysics*, *66*(1), 50–53. https://doi.org/10.1190/1.1444921

Lumley, D. E., Nur, A., Strandenes, S., Hydro, N., Dvorkin, J., & Packwood, J. (1994). Seismic monitoring of oil production: A feasibility study. *SEG Technical Program Expanded Abstracts 1994*, 319–322. https://doi.org/10.1190/1.1932085

MacBeth, C., Amini, H., & Izadian, S. (2020). Review paper: Methods of measurement for 4D seismic post-stack time shifts. *Geophysical Prospecting*, *68*(9), 2637–2664. https://doi.org/10.1111/1365-2478.13022

MacBeth, C., & Bachkheti, S. (2021). A geomechanical correction for time-lapse amplitude variation with offset. *Geophysics*, *86*(2), M29–M40. https://doi.org/10.1190/geo2020-0398.1

Macquet, M., Lawton, D. C., Saeedfar, A., & Osadetz, K. G. (2019). A feasibility study for detection thresholds of CO2 at shallow depths at the CaMI Field Research

Station, Newell County, Alberta, Canada. *Petroleum Geoscience*, *25*(4), 509–518. https://doi.org/10.1144/petgeo2018-135

Mandel, J. (1953). Consolidation des sols (étude mathématique). *Geotechnique*, *3*(7), 287–299. https://doi.org/10.1680/geot.1953.3.7.287

Mavko, G., Mukerji, T., & Dvorkin, J. (2009). *The rock physics handbook: Tools for seismic analysis of porous media* (2nd ed.). Cambridge University Press. https://doi.org/10.1017/CBO9780511626753

Peaceman, D. W. (2000). *Fundamentals of numerical reservoir simulation*. Elsevier.

Perlin, K. (1985). An image synthesizer. *ACM Siggraph Computer Graphics*, *19*(3), 287–296. https://doi.org/10.1145/325165.325247

Pevzner, R., Shulakova, V., Kepic, A., & Urosevic, M. (2011). Repeatability analysis of land time-lapse seismic data: CO2CRC Otway pilot project case study. *Geophysical Prospecting*, *59*(1), 66–77. https://doi.org/10.1111/j.1365-2478.2010.00907.x

Prasad, M., Kopycinska, M., Rabe, U., & Arnold, W. (2002). Measurement of Young's modulus of clay minerals using atomic force acoustic microscopy. *Geophysical Research Letters*, *29*(8), 13-1-13–4. https://doi.org/10.1029/2001GL014054

Rackett, H. G. (1970). Equation of state for saturated liquids. *Journal of Chemical and Engineering Data*, *15*(4), 514–517. https://doi.org/10.1021/je60047a012

Ramesh Kumar, K., Makhmutov, A., Spiers, C. J., & Hajibeygi, H. (2021). Geomechanical simulation of energy storage in salt formations. *Scientific Reports*, *11*(1), 19640. https://doi.org/10.1038/s41598-021-99161-8

Reinicke, C., Dukalski, M., & Wapenaar, K. (2020). Comparison of monotonicity challenges encountered by the inverse scattering series and the Marchenko demultiple method for elastic waves. *Geophysics*, *85*(5), Q11–Q26. https://doi.org/10.1190/geo2019-0674.1

Reinicke, C., & Wapenaar, K. (2019). Elastodynamic single-sided homogeneous Green's function representation: Theory and numerical examples. *Wave Motion*, *89*, 245–264. https://doi.org/10.1016/j.wavemoti.2019.04.001

Reuss, A. (1929). Berechnung der fließgrenze von mischkristallen auf grund der plastizitätsbedingung für einkristalle. *ZAMM - Journal of Applied Mathematics and Mechanics / Zeitschrift für Angewandte Mathematik und Mechanik*, *9*(1), 49–58. https://doi.org/10.1002/zamm.19290090104

Slob, E., Wapenaar, K., Broggini, F., & Snieder, R. (2014). Seismic reflector imaging using internal multiples with Marchenko-type equations. *Geophysics*, *79*(2), S63–S76. https://doi.org/10.1190/geo2013-0095.1

Snieder, R., Grêt, A., Douma, H., & Scales, J. (2002). Coda wave interferometry for estimating nonlinear behavior in seismic velocity. *Science*, *295*(5563), 2253–2255. https://doi.org/10.1126/science.1070015

Sokolova, I., Bastisya, M. G., & Hajibeygi, H. (2019). Multiscale finite volume method for finite-volume-based simulation of poroelasticity. *Journal of Computational Physics*, *379*, 309–324. https://doi.org/10.1016/j.jcp.2018.11.039

Terzaghi, K., Peck, R. B., & Mesri, G. (1996). *Soil mechanics in engineering practice*. John wiley & sons.

Thorbecke, J. W., & Draganov, D. (2011). Finite-difference modeling experiments for seismic interferometry. *Geophysics*, *76*(6), H1–H18. https://doi.org/10.1190/geo2010-0039.1

Trani, M., Arts, R., Leeuwenburgh, O., & Brouwer, J. (2011). Estimation of changes in saturation and pressure from 4D seismic AVO and time-shift analysis. *Geophysics*, *76*(2), C1–C17. https://doi.org/10.1190/1.3549756

Tura, A., & Lumley, D. E. (1998). Subsurface fluid flow properties from time-lapse elastic wave reflection data. *Mathematical Methods in Geophysical Imaging V*, *3453*, 125–138. https://doi.org/10.1117/12.323284

van IJsseldijk, J., Hajibeygi, H., & Wapenaar, K. (2023a). A framework for subsurface monitoring by integrating reservoir simulation with time-lapse seismic surveys. *Scientific Reports*, *13*, 13661. https://doi.org/10.1038/s41598-023-40548-0

van IJsseldijk, J., van der Neut, J., Thorbecke, J., & Wapenaar, K. (2023b). Extracting small time-lapse traveltime changes in a reservoir using primaries and internal multiples after Marchenko-based target zone isolation. *Geophysics*, *88*(2), no 2., R135–R143. https://doi.org/10.1190/geo2022-0227.1

van IJsseldijk, J., & Wapenaar, K. (2021). Discerning small time-lapse traveltime changes by isolating the seismic response of a reservoir using the Marchenko method. *First International Meeting for Applied Geoscience & Energy Expanded Abstracts*, 3449–3453. https://doi.org/10.1190/segam2021-3583007.1

Wang, H. F. (2001). *Theory of linear poroelasticity with applications to geomechanics and hydrogeology*. Princeton University Press. https://doi.org/10.1515/9781400885688

Wang, Y., Vuik, C., & Hajibeygi, H. (2022). Analysis of hydrodynamic trapping interactions during full-cycle injection and migration of CO2 in deep saline aquifers. *Advances in Water Resources*, *159*, 104073. https://doi.org/10.1016/j.advwatres.2021.104073

Wapenaar, K., & van IJsseldijk, J. (2020). Employing internal multiples in time-lapse seismic monitoring, using the Marchenko method. *82nd EAGE Annual Conference & Exhibition*, *2020*. https://doi.org/10.3997/2214-4609.202011576

Wapenaar, K., Draganov, D., Snieder, R., Campman, X., & Verdel, A. (2010). Tutorial on seismic interferometry: Part 1—basic principles and applications. *Geophysics*, *75*(5), 75A195–75A209. https://doi.org/10.1190/1.3457445

Wapenaar, K., Thorbecke, J., van der Neut, J., Broggini, F., Slob, E., & Snieder, R. (2014). Marchenko imaging. *Geophysics*, *79*(3), WA39–WA57. https://doi.org/10.1190/geo2013-0302.1

White, J. A., Castelletto, N., Klevtsov, S., Bui, Q. M., Osei-Kuffuor, D., & Tchelepi, H. A. (2019). A two-stage preconditioner for multiphase poromechanics in reservoir simulation. *Computer Methods in Applied Mechanics and Engineering*, *357*, 112575. https://doi.org/10.1016/j.cma.2019.112575

5

TIME-LAPSE APPLICATIONS OF THE MARCHENKO METHOD ON THE TROLL FIELD

The data-driven Marchenko method is able to redatum wavefields to arbitrary locations in the subsurface, and can, therefore, be used to isolate zones of specific interest. This creates a new reflection response of the target zone without interference from over- or underburden reflectors. Consequently, the method is well suited to obtain a clear response of a subsurface reservoir, which can be advantageous in time-lapse studies. The clean isolated responses of a baseline and monitor survey can be more effectively compared, hence the retrieval of time-lapse characteristics is improved. This research aims to apply Marchenko-based isolation to a time-lapse marine dataset of the Troll field in Norway in order to acquire an unobstructed image of the primary reflections, and retrieve small time-lapse traveltime difference in the reservoir. It is found that the method not only isolates the primary reflections but can also recover internal multiples outside the recording time. Both the primaries and the multiples can then be utilised to find time-lapse traveltime differences. More accurate ways of time-lapse monitoring will allow for a better understanding of dynamic processes in the subsurface, such as observing saturation and pressure changes in a reservoir or monitoring underground storage of hydrogen and CO_2.

This chapter has been submitted and is under review, a preprint is available here: van IJsseldijk, J., Brackenhoff, J., Thorbecke, J., & Wapenaar, K. (2023a). Time-lapse applications of the Marchenko method on the Troll field. https://doi.org/10.48550/arXiv.2303.10964

Minor modifications have been applied to keep consistency within this thesis.

5.1. INTRODUCTION

Time-lapse seismic has become increasingly important to monitor fluid flows and geomechanical changes in subsurface reservoirs, such as observing pressure and saturation changes (Dadashpour et al., 2007; Johnston et al., 1998; Landrø, 2001), monitoring CO_2 storage sites (Chadwick et al., 2010; Ivandic et al., 2018; Pevzner et al., 2011) and assessing compaction and subsidence (Barkved & Kristiansen, 2005; Hatchell & Bourne, 2005). Typically, these studies compare an initial baseline study followed by one or more monitor studies. From these studies small differences in amplitude (Landrø, 2001), in traveltime (Landrø & Stammeijer, 2004; MacBeth et al., 2019) or in a combination of both (Trani et al., 2011; Tura et al., 2005) can be observed. These changes can be retrieved by independently creating an image for both the baseline and monitor study, and subtracting these images from one another to find the time-lapse differences. This subtraction highlights the dynamic differences, for example the fluid flow in the reservoir, while removing the static part from the data, such as the time invariant geology (Lumley, 2001).

A common technique to retrieve time-lapse time differences is by cross-correlating the signal of the baseline and monitor surveys. This can either be done on picked events shared by both surveys or to the complete data sets all at once (MacBeth et al., 2020). Snieder et al. (2002) show that due to multiple scattering, correlations of the coda of a signal can display larger time-lapse effects compared to correlating first arrivals. This technique, called coda wave interferometry, can be applied on laboratory scale to core samples (Singh et al., 2019) as well as on field scales to monitor temporal changes in a volcano (Grêt et al., 2005). Wapenaar and van IJsseldijk (2020) introduce a novel methodology to clearly identify the reservoir response from a seismic survey using Marchenko-based isolation as well as to improve the detectability of the traveltime changes by correlating reservoir-related internal multiples, akin to the principle of coda wave interferometry.

At the base of this new methodology are the Marchenko equations, which allows for a data-driven redatuming of the seismic wavefield to an arbitrary focal point in the subsurface (Slob et al., 2014; Wapenaar et al., 2014). Since all orders of internal multiples are accounted for, the redatumed wavefields are free from any interactions of the overburden, hence providing an unobstructed view of the primary reflections of the reservoir when a focal level just above the reservoir is chosen. The Marchenko equations can then be applied a second time to the newly found reflection response to also remove underburden interactions (Wapenaar & Staring, 2018). If the second focal depth is chosen just below the reservoir, the final result has effectively isolated all primaries and multiples of the reservoir. This isolated response can then be used to more accurately retrieve time-lapse traveltime shifts due to changes in the reservoir by cross-correlating baseline and monitor responses (van IJsseldijk & Wapenaar, 2021; van IJsseldijk et al., 2023b, and Chapter 3).

Here, the aim is to apply the Marchenko method to marine time-lapse datasets of the Troll Field and retrieve accurate time-lapse traveltime shifts. In order to do this we first review the theory of isolating the reservoir response and how to extract time-lapse traveltime differences from the primary and multiple reflections. Next, the Troll Field data are introduced; before the methodology can be applied a number of preprocessing steps and limitations of the data need to be considered. After properly preparing both the baseline and monitor surveys, Marchenko-based isolation is used to clean up the reservoir response for time-lapse analysis. Finally, the traveltime differences related to the reservoir are calculated from suitable primaries and multiples.

5.2. THEORY

This section briefly reviews the theory of Marchenko-based isolation of the reservoir response from the full reflection response. After applying this isolation to both a baseline and monitor study, the traveltime differences inside the reservoir can be more accurately calculated, as described in the second part of this section. A full derivation of the Marchenko method is beyond the scope of this paper, instead only relevant equations are discussed here. Wapenaar et al. (2021) provide a more thorough derivation and background on the Marchenko method.

5.2.1. MARCHENKO-BASED ISOLATION

The Marchenko method relies on two Green's function representations that relate the extrapolated Green's functions ($U^{-,\pm}$) to the extrapolated focusing functions ($v^{\pm}$) via the reflection response $R(\mathbf{x}_R,\mathbf{x}_S,t)$. In this notation the first and second coordinate describe the receiver and source position, respectively, and t denotes time. The superscripts $-,\pm$ represent an up-going receiver field from a up $(-)$ or down-going $(+)$ source field. The focusing functions are defined in a truncated medium, which is the same as the actual medium above an arbitrary focal level and homogeneous below. In the actual medium the focusing functions let the wavefield converge to the focal point, creating a virtual source that produces the Green's functions between the focal depth and the surface. Both the focusing and Green's functions are extrapolated from the focal depth to the surface, so that the coordinates of all the functions are located at acquisition surface $\mathbb{S}_0$. The focusing of the wavefield in the actual medium is then described by the following equations (van der Neut & Wapenaar, 2016):

$$U^{-,+}(\mathbf{x}_R,\mathbf{x}'_S,t)+v^{-}(\mathbf{x}_R,\mathbf{x}'_S,t)=\int_{\mathbb{S}_0} R(\mathbf{x}_R,\mathbf{x}_S,t)*v^{+}(\mathbf{x}_S,\mathbf{x}'_S,t)d\mathbf{x}_S, \tag{5.1}$$

and

$$U^{-,-}(\mathbf{x}_R,\mathbf{x}'_S,-t)+v^{+}(\mathbf{x}_R,\mathbf{x}'_S,t)=\int_{\mathbb{S}_0} R(\mathbf{x}_R,\mathbf{x}_S,-t)*v^{-}(\mathbf{x}_S,\mathbf{x}'_S,t)d\mathbf{x}_S. \tag{5.2}$$

Here, $*$ denotes a convolution and the right-hand side integrates over the source positions $\mathbf{x}_S$ at the acquisition surface $\mathbb{S}_0$. These two equations have four unknowns, hence, to solve the equations, an additional causality constraint is introduced, which takes advantage of the fact that the focusing and Green's functions are separable in time (Wapenaar et al., 2014). In order to achieve this separation an estimate of the two-way traveltime (twt) from $\mathbb{S}_0$ to the focal depth and back is required. This estimate can for example be obtained from a smooth velocity model. By limiting Equations 5.1 and 5.2 between $t=0$ s and this twt, the Green's functions in the left-hand side vanish (van der Neut & Wapenaar, 2016); the resulting equations are known as the extrapolated Marchenko equations, which now only contain two unknowns and can, therefore, be solved iteratively (Thorbecke et al., 2017) or by inversion (van der Neut et al., 2015a).

Next, the subsurface is divided in three units; overburden a, target zone b and underburden c as shown in Figure 5.1. The over- and underburden contain undesirable responses, whereas the target zone contains the reservoir of interest for the time-lapse study. The primary and multiple reflections of the over- and underburden can be removed using a twofold Marchenko-based strategy, leaving a reflection response only containing events from the target zone. First, Equations 5.1 and 5.2 are used to find the extrapolated Green's functions with a focal level between overburden a and target zone b. Using these Green's functions, a reflection response free of overburden interactions can be acquired by solving (Wapenaar et al., 2021, and Appendix B):

$$U^{-,+}_{a|bc}(\mathbf{x}_R,\mathbf{x}'_S,t) = -\int_{\mathbb{S}_0} U^{-,-}_{a|bc}(\mathbf{x}_R,\mathbf{x}'_R,t) * R_{bc}(\mathbf{x}'_R,\mathbf{x}'_S,t)\,d\mathbf{x}'_R. \tag{5.3}$$

The subscript $a|bc$ denotes that the extrapolated Green's functions are retrieved from the full reflection response (R_{abc}) with a focal depth between units a and b. The reflection response R_{bc} is retrieved by a multi-dimensional deconvolution (MDD, Broggini et al., 2014), and contains all primary and multiple reflections from b and c, but none from overburden a (Figure 5.1b). This new reflection response can then be used to find focusing functions below the target zone, which in turn are used to find the reflection response that only contains target zone events (Wapenaar & Staring, 2018, and Appendix B):

$$v^{-}_{b|c}(\mathbf{x}_R,\mathbf{x}'_S,t) = \int_{\mathbb{S}_0} v^{+}_{b|c}(\mathbf{x}_R,\mathbf{x}'_R,t) * R_{b}(\mathbf{x}'_R,\mathbf{x}'_S,t)\,d\mathbf{x}'_R. \tag{5.4}$$

The subscript $b|c$ denotes that the extrapolated focusing functions are retrieved from the reflection response without overburden (R_{bc}) using a focal depth at the interface of units b and c. Equation 5.4 directly follows from the definition of a focusing function in the truncated medium (Wapenaar et al., 2021). Once again, the isolated reflection response R_b can be retrieved from this equation by MDD, and consists solely of the reflections (primary and multiple) from the target zone. van IJsseldijk et al. (2023b) demonstrate how the internal multiples in the target area b can be artificially enhanced by increasing the amplitude of the coda of the downgoing focusing function v^+, in order to benefit the identification of the multiples and the extraction of time-lapse traveltime differences. Figure 5.1 summarises the twofold approach to isolate the reservoir response from a full reflection response. This process is applied to the baseline as well as the monitor study, to acquire the isolated reservoir responses in both studies. These isolated responses are then used to find the time-lapse traveltime differences inside the reservoir.

5.2.2. EXTRACTING TRAVEL-TIME DIFFERENCES

Once an isolated reflection response of the primary and multiples around the reservoir is acquired, the traveltime differences in the reservoir between the baseline and monitor survey can be determined. However, the time-lapse delays due to changes in the overburden have not yet been accounted for. To remove these delays a primary reflection ($P1$) above the reservoir is identified, which can then be used as a control event that includes the overburden time differences, but excludes the differences in the reservoir. Identifying such an event is trivial in the isolated response, which is solely comprised of the target zone reflections. Next, a second reflection, either a second primary ($P2$) or an

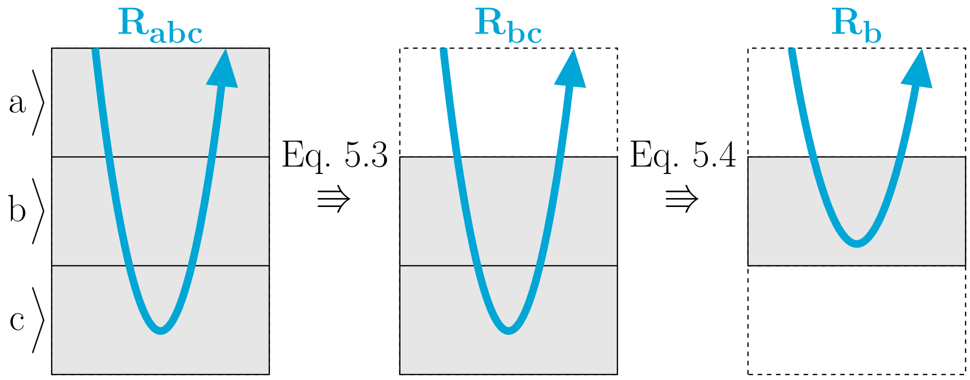

Figure 5.1: Graphic showing the concept of Marchenko-based isolation. The medium is divided in 3 units; overburden a, target zone b and underburden c. First, the overburden is removed from the response as described in equation 3. Next, the underburden is removed, leaving only the target zone with the reservoir response.

internal multiple ($M1$, $M2$ etc.), is identified, this time from below the reservoir so that it contains both overburden and the reservoir traveltime differences. Subsequently, these two reflections are cross-correlated to remove overburden changes (Chapter 3):

$$C_\star(\mathbf{x}_0,\tau) = \int_0^\infty \Theta_{P1}(t+\tau)R_b(\mathbf{x}_0,t+\tau)\Theta_\star(t)R_b(\mathbf{x}_0,t)\,dt. \tag{5.5}$$

Here, C represents the cross-correlation, $\mathbf{x}_0$ the zero-offset coordinate, and Θ is a time-window that selects the desired reflection from the isolated reflection response as follows:

$$\Theta_\star(t) = \begin{cases} 1, \text{if } t_\star - \epsilon < t \leq t_\star + \epsilon \\ 0, \text{otherwise.} \end{cases} \tag{5.6}$$

The subscript $\star$ denotes either primary 1 or 2 ($P1$ or $P2$) or an internal multiple, $t_\star$ then specifies the twt of this event, and ϵ serves as a small shift to include the full wavelet. Figure 5.2a and b show how Figure 5.5 is used to retrieve the time-lags of primary 1 with primary 2 as well as with multiple 1, respectively. The final results after cross-correlation no longer contain time-lapse overburden effects. The next step, where the baseline and monitor time-difference will be computed, will, therefore, only contain time-differences from the reservoir and none from the overburden.

Finally the actual time-lapse differences are retrieved. In order to achieve this, the time-lag correlations for both the baseline and monitor study are computed using Figure 5.5. Thereafter, these time-lags are cross-correlated once more to retrieve the traveltime difference ($\Delta t_\star$) in the reservoir:

$$\Delta t_\star(\mathbf{x}_0) = \underset{\tau}{\arg\max}\left(\int_0^\infty C_\star(\mathbf{x}_0,t+\tau)\bar{C}_\star(\mathbf{x}_0,t)\,dt\right). \tag{5.7}$$

$C_\star$ is the retrieved correlation from Figure 5.5, the bar denotes retrieval in the monitor survey as opposed to the baseline survey. The argument of the maximum is used to find the zero-offset time shifts from the final correlation. Van IJsseldijk et al. (2023b) apply

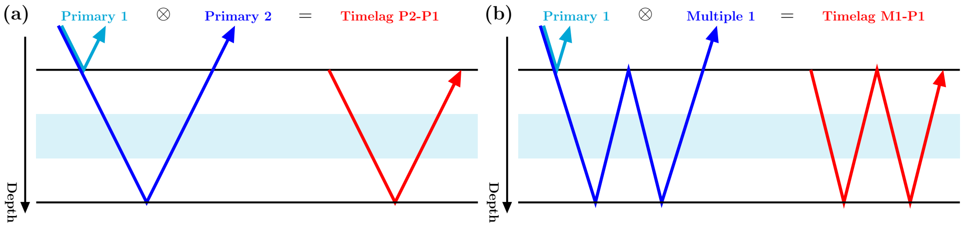

Figure 5.2: Example of cross-correlations of primary 1 with primary 2 (a) and multiple 1 (b). In the resulting time-lags, the common path is canceled, i.e. the overburden effects are effectively removed. Note, how the multiple travels through the reservoir layer (in light blue) an additional time compared to primary 2.

this method to a synthetic set to find time differences in three subsurface dome structures. Application of the Marchenko method to field data is more complex due to strict amplitude requirements on the reflection response (Brackenhoff et al., 2019; Staring et al., 2018). The next section discusses how to to overcome this and other limitations on field data.

5.3. APPLICATION TO THE TROLL FIELD

The methodology is applied to a marine time-lapse data set shot over the Troll Field off the Norwegian coast. In 1997 a 3D baseline survey was conducted over the Troll West Gas Province, followed by a monitor survey in 2002. This study considers a 2D subset of these 3D surveys. The time-lapse target is a hydrocarbon-water contact. Specifically the hydrocarbon is a gas layer underlain by an oil leg with a varying thickness between 0 and 28 m (Hellem et al., 1986). The contact partially coincides with a geologic structure, which makes extracting time-lapse effects from the data challenging (Bannister et al., 2005). Additionally, the repeatability of the surveys is subpar, further complicating time-lapse analysis with conventional methods (Qu & Verschuur, 2020).

A number of basic pre-processing steps were applied to both datasets. First, it should be noted that the data were not completely raw, namely some unknown time gain and wavelet processing as well as far offset muting was performed. The known pre-processing first applied a regularisation to get a 2D geometry with 481 co-located source and receiver positions sampled at 12.5 m. Near-offsets of about 85 m were interpolated by parabolic Radon transform (Kabir & Verschuur, 1995). Next, surface-related multiple elimination (SRME) was applied to get a clearer image of the reservoir reflections (Verschuur et al., 1992). Note that this does not handle internal multiples, which will be dealt with separately using the Marchenko-based isolation. Deghosting was then applied as well as optimum wavelet processing to ensure zero-phase character.

Aside from the unknown scaling factors, application of the Marchenko method also suffered due to a lack of a velocity model and the limited recording time of 2 s. To properly remove internal multiples with the Marchenko method, it is important that the scaling of the reflection response is accurate (van der Neut et al., 2015b). Moreover, a (smooth) velocity model is required to compute an estimate of the twt between the focal depth and the surface. The limited recording time means that some of the internal multiples from the target zone are not recorded. In the following sections these three problems

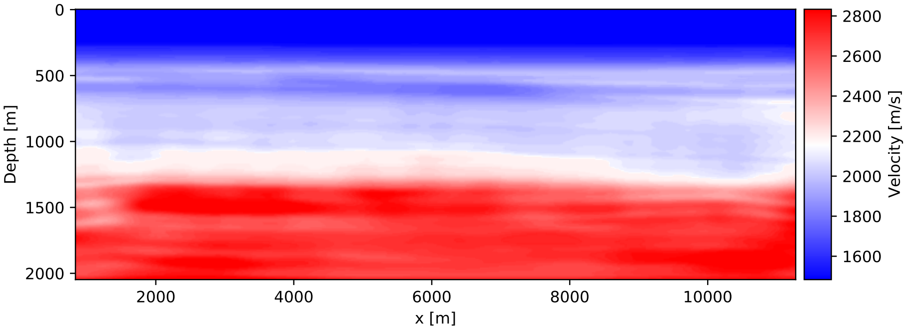

Figure 5.3: Baseline velocity model of the Troll field, derived from Qu and Verschuur (2020).

will be taken care of one-by-one. Finally, the results of isolating the reservoir response and extracting time-differences will be discussed.

5.3.1. VELOCITY MODEL ESTIMATION

In order to separate focusing functions from Green's functions an estimation of the twt from the surface to the focal depth is required. Ordinarily, this is achieved with the use of an eikonal solver in a smooth velocity model. Qu and Verschuur (2020) use a simultaneous joint migration inversion (S-JMI) approach to find the approximate baseline velocity model. However, this model was not readily available for this study. Instead the model was derived from Figure 14a in Qu and Verschuur (2020). By matching the RGB values in the figure with the colorbar, a rough estimate of the original model was acquired, as shown in Figure 5.3. Since no major velocity changes are expected between the two time-lapse surveys, this model can be used for the Marchenko-based isolation of both the reservoir in the baseline and the monitor survey.

5.3.2. SCALING OF THE REFLECTION RESPONSE

Brackenhoff (2016) introduces a cost function that can be minimised to find the optimal scaling of the reflection data. Here, this function has to be slightly adapted in order to handle the extrapolated functions, but the principle of the method remains the same. The principle of using these cost functions relies on the fact that the energy in the redatumed reflection response usually decreases due to the removal of internal multiples. Consequently, if the scaling of the data is too low not all multiple energy will be removed. Whereas, if the scaling is too high the energy will be excessively magnified. Hence, only if the data are correctly scaled the cost function will be minimized due to the lower energy by the multiple removal. The redatuming in Equation 5.7 is relatively expensive to apply multiple times on the data for each scaling factor. Therefore, the computationally inexpensive alternative of double dereverberation (ddr) by double-focusing is considered instead (Wapenaar et al., 2021):

$$R_{ddr}(\mathbf{x}'_R, \mathbf{x}'_S, t) = \int_{\mathbb{S}_0} v^{+}(\mathbf{x}_R, \mathbf{x}'_R, t) * U^{-,+}(\mathbf{x}_R, \mathbf{x}'_S, t)\, d\mathbf{x}_R. \tag{5.8}$$

The downside of Equation 5.8 is that some remaining interactions of the overburden will still be present in the computed reflection response R_{ddr}. As mentioned before the upside is that the double-focusing method is relatively cheap, more stable and can easily be applied for a wide range of scaling factors (Staring et al., 2018). The cost function considers the ratio of the energy in the reflection response before and after Marchenko redatuming, and is applied as follows:

$$J(b) = \frac{||R_{ddr}(\mathbf{x}'_R, \mathbf{x}'_S, t)||_2}{||R_{ddr,0}(\mathbf{x}'_R, \mathbf{x}'_S, t)||_2}. \tag{5.9}$$

Here, $||...||_2$ denotes the L2-norm, J is the cost function, and b is the scaling of the original reflection response. $R_{ddr,0}$ is the response for the focusing and Green's function of the first Marchenko iteration, which parallels a standard time-reversal experiment without internal multiple removal (Wapenaar et al., 2017). R_{ddr} is the response after the final Marchenko iteration, as specified by the user.

The estimation of the scaling factor depends on the removal of internal multiples by the Marchenko method. This process is complicated by the limited recording time of 2 s. This means that instead of picking a deep focal level below all reflectors, as is ideal (Brackenhoff, 2016), a shallower focal level has to be used to calculate the cost functions. Consequently, the cost functions do not contain a lowest minimum, and only a range of possible factors is acquired. This range is further refined to find a single scaling factor by inverting for the reflection response in Equation 5.3 for a limited amount of scaling factors, and visually examining the resulting reflection response. Finally, a single factor of $5 \cdot 10^{-5}$ is found using this method for both time-lapse surveys.

5.3.3. MULTIPLE RETRIEVAL BEYOND RECORDED TIME

The short recording time not only constrains the effectiveness of the scaling factor, but also causes some of the target multiples to not be recorded in the data. These multiples provide complementary information of the target zone and are ideally recovered from the data. A closer look at the focusing functions in Equation 5.4 reveals that these functions are solely defined between $t = 0$ and the two-way traveltime to the focal depth (i.e. in the truncated medium). Because of this finite behaviour, the focusing functions do not require all the recorded internal multiples to retrieve the reflection response without underburden. Consequently, Equation 5.4 can be used to compute the internal multiples outside of the recorded time. Note that this only applies for underburden removal (i.e. Equation 5.4), but not for overburden removal (i.e. Equation 5.3) as the Green's functions are infinite in time, hence all events in the Green's functions are used to reconstruct the reflection response without overburden.

In order to illustrate how the focucing functions can be used to retrieve additional multiples outside the recorded time, a simple 3-layer 1D model is considered. The acoustic impedance contrasts in this model are very strong, ensuring that a strong multiple train is generated as shown in Figure 5.4a. Next, two focal levels are considered; one at 1000 m that does not include any multiples in it's response, and one at 1200 m that does. Subsequently, the Marchenko method and Equation 5.4 are used to retrieve a reflection response free of underburden effects, once with the full reflection response, and once using solely the primary reflections (i.e. with limited information). On the one hand,

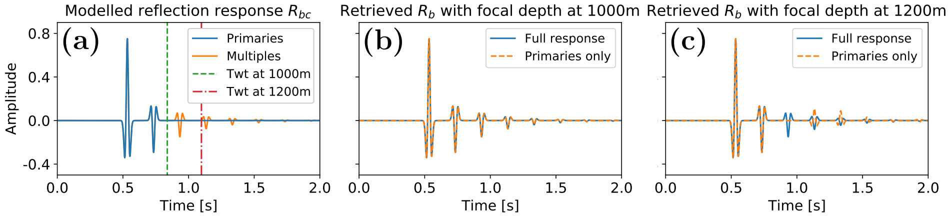

Figure 5.4: Reflection response R_{bc} modelled in a medium with a velocity and density profile of 1500 [m/s] & [kg/m^3] for depths 0 to 400 m, 4000 [m/s] & [kg/m^3] from 400 to 800 m and 1750 [m/s] & [kg/m^3] below 800 m. In (a), the primary reflections are shown in blue and the internal multiples in orange, with the two-way traveltime (twt) for depths 1000 m and 1200 m marked with a green dashed and red dot-dashed line, respectively. Next, the retrieved (by MDD) reflection response above the focal depth R_b are shown for Marchenko with the full response vs for the primary reflections only in blue and orange, respectively. Note that, in (b) and (c), response R_b can be properly retrieved (using Equation 5.4) from data that contains all events within the time-window (b), if any events are missing in this window response R_b can no longer be correctly retrieved (c).

shown in Figure 5.4b in the case where no multiples are present in the time-window at the focal depth, the underburden is correctly removed independent on inclusion of all multiples in the original reflection response. On the other hand if the time window does include one or more multiples, the underburden can no longer accurately be removed when using primary reflections only (e.g. Figure 5.4c). This is caused by the fact that using the primaries only in Figure 5.4c, reconstructs the reflection response with incomplete data (i.e. it misses a multiple important for reconstruction). It is, therefore, important that the time-window contains all information of both primaries and multiples when removing the underburden.

This numerical experiment suggests that even though the internal multiples may not be recorded, they can still be extracted from the data by using the focusing functions. However, one has to ensure that all information is included in the time-window, meaning that focal depth and corresponding time-window should be picked as closely to the end of the recorded data as possible, in order to ensure all events for finding the focusing functions are included. Since the focal level in Equation 5.4 can be arbitrary chosen at any level below the two primary reflectors, this constraint can easily be satisfied in the current study.

5.3.4. RESULTS OF THE MARCHENKO-BASED ISOLATION

After the data are properly pre-processed as described in the previous sections, the Marchenko-based isolation can now be applied. The result of this isolation is shown in Figure 5.5. A reflector right above the reservoir is selected as primary 1 just after 1.65 s twt. The first focal depth, for overburden removal, is chosen above this reflector at a depth of 1575 m. Next, primary 2 is identified around 1.9 s twt, with a third primary following closely behind. Hence, the second focal depth, for underburden removal, is picked right in between these two reflectors at a depth of 1975 m. Subsequently, primary 1 and primary 2 can be isolated from the full reflection response. Finally, the internal multiples of the target zone are enhanced by increasing the amplitudes of the coda of the down-going focusing function before MDD of Equation 5.4 as described in van IJsseldijk et al. (2023b).

Figure 5.5 shows the results for the baseline and monitor study in the first and second row, respectively. Note that this figure shows zero-offsets gathers with red, green, blue and orange highlights for the first primary, second primary, first multiple and second multiple of the target area, respectively. These windows will later on be used to extract time-differences. The first column in the figure shows the original reflection response with a recording time until 2 s. There are no data available at 2.15 s and 2.4 s, where the internal multiples are expected. In the second column the response after over- and underburden removal is shown. Note that the internal multiples can now be observed at times beyond 2 s twt, these multiples are especially strong at a lateral distance of 3500 m to 6000 m. Furthermore, the over- and underburden reflections are removed not only below and above the focal levels, but also inside the target zone as marked by the blue arrows in the figure. Finally, the third column shows the difference between the first two panels, once again the removal of overburden multiples in the target area between primary 1 and 2 is noted. However, there also seems to be quite some coherent information removed from the first and second primary. This could be an indication that the optimal scaling factor has not been found or another explanation could be that the MDD applied a correction on the phase of the signal (e.g. van Dalen et al., 2015).

5

The results in Figure 5.5 for the baseline and monitor survey are quite similar, although some minor differences can be detected when carefully analyzing the panels on each row. In order to more precisely compare the two studies, a raw stack of all shots in the reflection data was computed for both the regular and the isolated response. The results of these stacks are displayed in Figure 5.6. The time-lapse effects are especially strong in the first primary at 1.65 s twt. Additionally, the stack created from the isolated response in (b) is much cleaner compared to the stack of the full reflection response in (a). Consequently, the isolated stack shows more continuity, which will aid in a better interpretation of the data.

5.3.5. EXTRACTING TIME-LAPSE TRAVELTIME DIFFERENCES

In order to accurately retrieve the time-lapse traveltime differences, the reflection the time is interpolated in the frequency domain from 4ms to 1ms. Next, the coloured windows in Figure 5.5 are now used to extract the time-lapse differences as described in Equation 5.7. Primary 1, highlighted in red, is correlated either with the second primary or with one of the multiples giving the time-lag between the two events. The baseline timelag is then correlated with the monitor timelag to find the time difference. First, the timelag of $P1$ and $P2$ is considered for the full reflection response R_{abc}, the response after overburden removal R_{bc} and the response after total isolation of the target zone R_b. The results of this experiment are shown in Figure 5.7. Note that the three lines are matching quite closely aside from the edges, where the deviations are slightly larger. The close match is easily explained with Figure 5.5, which shows that both primaries are already visible in the original reflection response with little obstructions from the overburden. The worse performance at the edges is most likely due to edge effects introduced by the MDD.

Figure 5.8 shows the retrieved traveltime differences for the primary and multiples in the isolated response R_b, which is the only response that contains the predicted internal

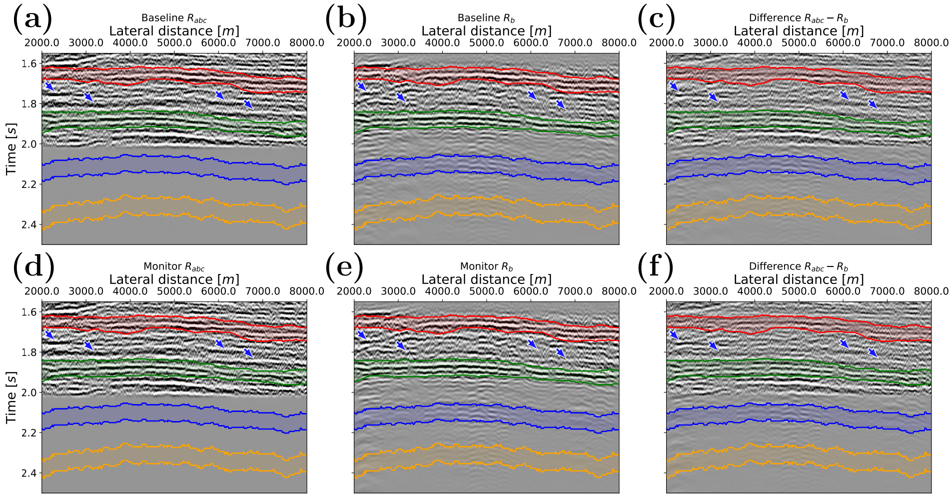

Figure 5.5: Zero-offset gathers of the baseline survey before (a), after Marchenko-based isolation (b) and their difference (c). The second row shows the same gathers for the monitor survey. The red, green, blue and orange highlights mark the first and second primary as well as the first and second order multiples from these primaries. The arrows point at removed multiples originating from the overburden. As shown in (a) and (d) the original data only recorded 2 s, but the Marchenko method is able to retrieve multiples beyond this cut-off (i.e. b and e).

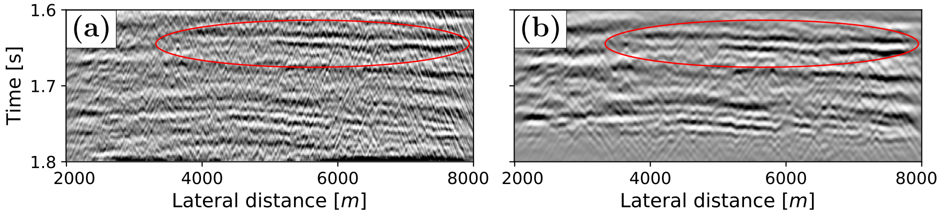

Figure 5.6: Time-lapse differences between the stacked baseline and monitor images, zoomed in on the target zone. The difference before Marchenko-based isolation is shown in (a). After Marchenko-based isolation (b) the reflectivity differences are a lot clearer as marked by the red ellipse.

multiples for this analysis. The red shading indicates the zone where the multiples are weak in amplitude shown in Figure 5.5 (b) and (e). The results for multiple 1 (in orange) and multiple 2 (in green) have been divided by a factor of 2 and 3, respectively, in order to have a fair comparison with the results from primary 2 (in blue), as these multiples probe the reservoir two or three times. Especially, between the red zones a strong match between the results of primaries and multiples in Figure 5.7 and the results in Figure 5.8 is noticed, which implies that the multiples are successfully recovered outside the recording time. The Marchenko-based isolation in Equation 5.4 predicts multiples based on only primary reflection data. This also happens in target area b, the primaries are used to predict the internal multiples between $P1$ and $P2$.

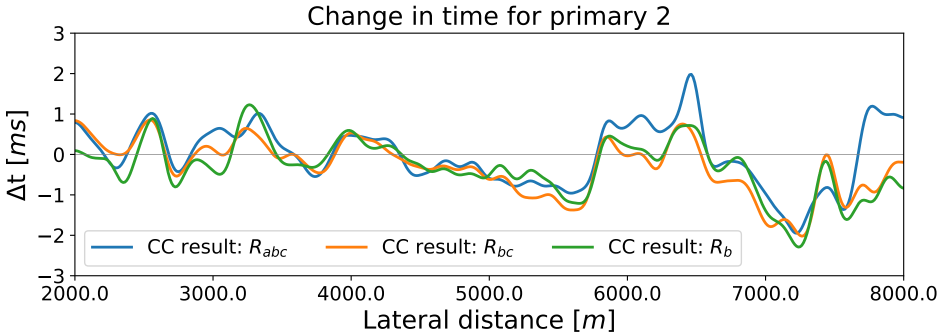

Figure 5.7: Time difference between the baseline and monitor time-lag of primary 1 and primary 2. The blue, orange and green colors represent the time-shift in the zero-offset response before Marchenko, after overburden removal and after full isolation, respectively.

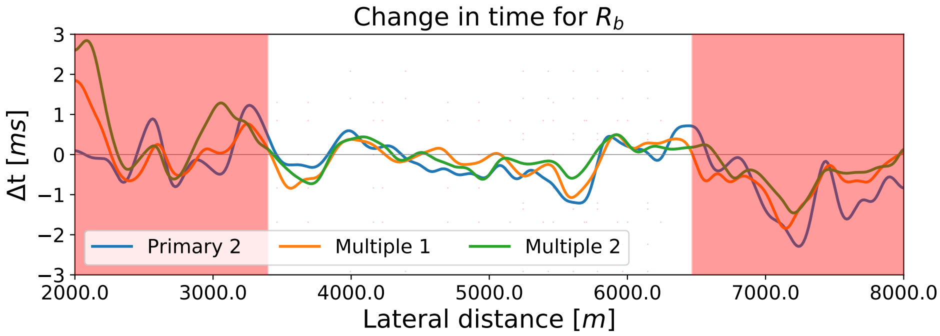

Figure 5.8: Time difference between the baseline and monitor time-lag. The time-lags between primary 1 and, respectively, primary 2 (blue), multiple 1 (orange) and multiple 2 (green) are shown. Note that the time shifts have been divided by 2 and 3, respectively, for multiple 1 and 2 to compare them with the primary shift. These differences where calculated in the isolated response, the red shading indicates the areas where the multiples are weaker, as shown in Figure 5.5b.

The extracted time-differences are compared to the results by Qu and Verschuur (2020), who retrieved approximate velocity changes. Some similarities are observed when looking at the sign of the change in velocity in Figure 15 of Qu and Verschuur (2020) and the differences in Figures 5.7 and 5.8. Additionally, based on approximations of the thickness of the reservoir and the velocity changes, the time-lapse traveltime differences are roughly estimated to lie somewhere between +1 ms and −1.5 ms, which is similar to the result found in this study. However, it is difficult to make one-on-one comparisons between the two studies as they consider different quantities that are not directly related to each other.

5.4. DISCUSSION

As shown in the previous section, Marchenko-based isolation of the reservoir response demonstrates promising results to improve time-lapse monitoring on field data. The reflection data are cleaned up, hence providing a superior image of the target zone, and time-lapse traveltime differences can be extracted from the primaries and recovered multiples. In this section, some limitations and potential future advancements of the method will be discussed.

Firstly, the current method only considers one time-lapse aspect of the data, namely traveltime differences. Traditional time-lapse studies, oftentimes, also consider changes in the amplitudes in the form of amplitude versus offset or angle (AVO and AVA) analyses. Recent studies investigated how angle-dependent reflectivity can be obtained with the Marchenko method for lateral invariant media with constant velocities (Alfaraj et al., 2020). If this method can be further extended to include fully heterogeneous media, it will be able to provide new insights for Marchenko-based time-lapse monitoring with AVA.

These AVA time-lapse analyses generally consider changes in both P- and S-waves (Landrø, 2001). On the contrary, the Marchenko method is mostly used for the acoustic case only, because the causality constraint is no longer ensured when elastic waves are introduced (da Costa Filho et al., 2014; Reinicke et al., 2020). This further complicates advanced AVA analysis on an isolated response, where only P-waves are considered.

The biggest obstacle to apply the Marchenko method to field data is the strict scaling requirements on the reflection data. This either calls for a carefully designed preprocessing scheme (Dukalski & Reinicke, 2022), which is not always feasible in the case of legacy data. Alternatively, a cost function can be minimised to find the optimal scaling; the approach that was considered in the current study. This technique suffered from the limited recording time of the data, causing most events to fall outside this limit. The cost function, therefore, was unable to converge to a minimum value.

Furthermore, the limited recording time also meant that the internal multiples of the target zone were not recorded. It was shown that these multiples could, in theory, be recovered accurately with the Marchenko method. The accuracy of this prediction on field data is harder to determine, where missing multiples of the target zone were predicted based on the primaries. While these multiples were not recorded in the data itself, once they were recovered with the Marchenko method, they still provided valuable insights into the time lapse differences of the target zone.

The current study extracted time-lapse differences from the zero-offset gathers. Instead, multiple offsets can be combined to acquire traveltime differences. On the one hand, the advantage of using multiple offsets is that the result is smoother over multiple offsets and thus more robust. On the other hand, the disadvantage is that the correlation windows have to be manually picked for each individual shot in the reflection response. While the inclusion of multiple offsets was explored for this study, it was found that the results did not significantly improve, hence the zero-offset gathers were deemed sufficient for the time-lapse analysis. However, computation of velocity changes from the traveltime differences demands multiple offsets to be used.

5.5. CONCLUSION

The purpose of this study was to apply Marchenko-based isolation of the reflection response on marine time-lapse data of the Troll field, in order to extract traveltime differences between the baseline and monitor surveys. To achieve this goal an approximate velocity model was acquired, and the correct scaling of the reflection response was determined. Subsequently, the over- and underburden were removed by twice employing Marchenko redatuming, once above and once below the target zone. From this newfound response two primaries and multiples were identified, and the time-lag between these events calculated. Finally, the baseline and monitor time-lags were correlated to obtain the time-lapse traveltime differences in the reservoir.

The methodology successfully eliminated imprints from signal originating outside of the target zone, resulting in an unobstructed view of the reservoir reflections. However, the target zone was relatively clean to begin with. It would, therefore, be interesting to test the methodology on a data with stronger interference from internal multiples (such as a subsalt reservoir), to be able to conclusively determine the impact of the time-lapse Marchenko scheme. On the current data the method was able to restore internal multiples lying outside of the recorded times. These were used together with the unobstructed primaries to retrieve the time-lapse traveltime differences inside of the reservoir.

These results open the door for future time-lapse applications of the Marchenko method, which ultimately can aid in our understanding of time-lapse changes in a reservoir caused by storage or production of resources inside the subsurface.

REFERENCES

Alfaraj, H., Brackenhoff, J., & Wapenaar, K. (2020). Obtaining angle-dependent reflectivity using the Marchenko redatuming method. *82nd EAGE Annual Conference & Exhibition*. https://doi.org/10.3997/2214-4609.202012138

Bannister, D., Roussanov, M., & Jones, C. (2005). Amplitude preserving Kirchhoff prestack time migration for time lapse processing on Troll west. In *Seg technical program expanded abstracts 2005* (pp. 1874–1877). https://doi.org/10.1190/1.2148069

Barkved, O. I., & Kristiansen, T. (2005). Seismic time-lapse effects and stress changes: Examples from a compacting reservoir. *The Leading Edge*, *24*(12), 1244–1248. https://doi.org/10.1190/1.2149636

Brackenhoff, J., Thorbecke, J., & Wapenaar, K. (2019). Monitoring of induced distributed double-couple sources using Marchenko-based virtual receivers. *Solid Earth*, *10*(4), 1301–1319. https://doi.org/10.5194/se-10-1301-2019

Brackenhoff, J. (2016). *Rescaling of incorrect source strength using Marchenko redatuming* [Master's thesis, TU Delft repository, Delft University of Technology] [http://resolver.tudelft.nl/uuid:0f0ce3d0-088f-4306-b884-12054c39d5da, accessed 11 August 2022].

Broggini, F., Wapenaar, K., van der Neut, J., & Snieder, R. (2014). Data-driven Green's function retrieval and application to imaging with multidimensional deconvolution. *Journal of Geophysical Research: Solid Earth*, *119*(1), 425–441. https://doi.org/10.1002/2013JB010544

Chadwick, A., Williams, G., Delepine, N., Clochard, V., Labat, K., Sturton, S., Buddensiek, M.-L., Dillen, M., Nickel, M., Lima, A. L., et al. (2010). Quantitative analysis of time-lapse seismic monitoring data at the Sleipner CO2 storage operation. *The Leading Edge*, *29*(2), 170–177. https://doi.org/10.1190/1.3304820

da Costa Filho, C. A., Ravasi, M., Curtis, A., & Meles, G. A. (2014). Elastodynamic Green's function retrieval through single-sided Marchenko inverse scattering. *Phys. Rev. E*, *90*, 063201. https://doi.org/10.1103/PhysRevE.90.063201

Dadashpour, M., Landrø, M., & Kleppe, J. (2007). Nonlinear inversion for estimating reservoir parameters from time-lapse seismic data. *Journal of Geophysics and Engineering*, *5*(1), 54–66. https://doi.org/10.1088/1742-2132/5/1/006

Dukalski, M., & Reinicke, C. (2022). Marchenko Multiple Elimination using conventional vs advanced 3-D to 2-D conversion on marine data. *83rd EAGE Annual Conference & Exhibition, 2022*. https://doi.org/10.3997/2214-4609.202210182

Grêt, A., Snieder, R., Aster, R. C., & Kyle, P. R. (2005). Monitoring rapid temporal change in a volcano with coda wave interferometry. *Geophysical Research Letters*, *32*(6). https://doi.org/10.1029/2004GL021143

Hatchell, P. J., & Bourne, S. J. (2005). Measuring reservoir compaction using time-lapse timeshifts. *SEG Technical Program Expanded Abstracts 2005*, 2500–2503. https://doi.org/10.1190/1.2148230

Hellem, T., Kjemperud, A., & Ovrebo, O. (1986). The Troll Field: a geological/geophysical model established by the PL085 Group. *Habitat of hydrocarbons on the Norwegian continental shelf. International conference*, 217–238.

Ivandic, M., Bergmann, P., Kummerow, J., Huang, F., Juhlin, C., & Lueth, S. (2018). Monitoring CO2 saturation using time-lapse amplitude versus offset analysis of 3D seismic data from the Ketzin CO2 storage pilot site, Germany. *Geophysical Prospecting*, *66*(8), 1568–1585. https://doi.org/10.1111/1365-2478.12666

Johnston, D. H., McKenny, R. S., Verbeek, J., & Almond, J. (1998). Time-lapse seismic analysis of Fulmar Field. *The Leading Edge*, *17*(10), 1420–1428. https://doi.org/10.1190/1.1437864

Kabir, M. N., & Verschuur, D. (1995). Restoration of missing offsets by parabolic Radon transform. *Geophysical Prospecting*, *43*(3), 347–368. https://doi.org/10.1111/j.1365-2478.1995.tb00257.x

Landrø, M. (2001). Discrimination between pressure and fluid saturation changes from time-lapse seismic data. *Geophysics*, *66*(3), 836–844. https://doi.org/10.1190/1.1444973

Landrø, M., & Stammeijer, J. (2004). Quantitative estimation of compaction and velocity changes using 4D impedance and traveltime changes. *Geophysics*, *69*(4), 949–957. https://doi.org/10.1190/1.1778238

Lumley, D. E. (2001). Time-lapse seismic reservoir monitoring. *Geophysics*, *66*(1), 50–53. https://doi.org/10.1190/1.1444921

MacBeth, C., Amini, H., & Izadian, S. (2020). Review paper: Methods of measurement for 4D seismic post-stack time shifts. *Geophysical Prospecting*, *68*(9), 2637–2664. https://doi.org/10.1111/1365-2478.13022

MacBeth, C., Mangriotis, M.-D., & Amini, H. (2019). Review Paper: Post-stack 4D seismic time-shifts: Interpretation and evaluation. *Geophysical Prospecting*, *67*(1), 3–31. https://doi.org/10.1111/1365-2478.12688

Pevzner, R., Shulakova, V., Kepic, A., & Urosevic, M. (2011). Repeatability analysis of land time-lapse seismic data: CO2CRC Otway pilot project case study. *Geophysical Prospecting*, *59*(1), 66–77. https://doi.org/10.1111/j.1365-2478.2010.00907.x

Qu, S., & Verschuur, D. J. (2020). Simultaneous joint migration inversion for high-resolution imaging/inversion of time-lapse seismic datasets. *Geophysical Prospecting*, *68*(4), 1167–1188. https://doi.org/10.1111/1365-2478.12918

Reinicke, C., Dukalski, M., & Wapenaar, K. (2020). Comparison of monotonicity challenges encountered by the inverse scattering series and the Marchenko demultiple method for elastic waves. *Geophysics*, *85*(5), Q11–Q26. https://doi.org/10.1190/geo2019-0674.1

Singh, J., Curtis, A., Zhao, Y., Cartwright-Taylor, A., & Main, I. (2019). Coda wave interferometry for accurate simultaneous monitoring of velocity and acoustic source locations in experimental rock physics. *Journal of Geophysical Research: Solid Earth*, *124*(6), 5629–5655. https://doi.org/10.1029/2019JB017577

Slob, E., Wapenaar, K., Broggini, F., & Snieder, R. (2014). Seismic reflector imaging using internal multiples with Marchenko-type equations. *Geophysics*, *79*(2), S63–S76. https://doi.org/10.1190/geo2013-0095.1

Snieder, R., Grêt, A., Douma, H., & Scales, J. (2002). Coda wave interferometry for estimating nonlinear behavior in seismic velocity. *Science*, *295*(5563), 2253–2255. https://doi.org/10.1126/science.1070015

Staring, M., Pereira, R., Douma, H., van der Neut, J., & Wapenaar, K. (2018). Source-receiver Marchenko redatuming on field data using an adaptive double-focusing method. *Geophysics*, *83*(6), S579–S590. https://doi.org/10.1190/geo2017-0796.1

Thorbecke, J., Slob, E., Brackenhoff, J., van der Neut, J., & Wapenaar, K. (2017). Implementation of the Marchenko method. *Geophysics*, *82*(6), WB29–WB45. https://doi.org/10.1190/GEO2017-0108.1

Trani, M., Arts, R., Leeuwenburgh, O., & Brouwer, J. (2011). Estimation of changes in saturation and pressure from 4D seismic AVO and time-shift analysis. *Geophysics*, *76*(2), C1–C17. https://doi.org/10.1190/1.3549756

Tura, A., Barker, T., Cattermole, P., Collins, C., Davis, J., Hatchell, P., Koster, K., Schutjens, P., & Wills, P. (2005). Monitoring primary depletion reservoirs using amplitudes and time shifts from high-repeat seismic surveys. *The Leading Edge*, *24*(12), 1214–1221. https://doi.org/10.1190/1.2149620

van der Neut, J., Thorbecke, J., Wapenaar, K., & Slob, E. (2015a). Inversion of the multidimensional Marchenko equation. *77th EAGE Conference and Exhibition 2015, 2015*. https://doi.org/10.3997/2214-4609.201412939

van der Neut, J., & Wapenaar, K. (2016). Adaptive overburden elimination with the multidimensional marchenko equation. *Geophysics*, *81*(5), T265–T284. https://doi.org/10.1190/geo2016-0024.1

van der Neut, J., Wapenaar, K., Thorbecke, J., & Slob, E. (2015b). Practical challenges in adaptive Marchenko imaging. In *Seg technical program expanded abstracts 2015* (pp. 4505–4509). https://doi.org/10.1190/segam2015-5791035.1

van Dalen, K. N., Mikesell, T. D., Ruigrok, E. N., & Wapenaar, K. (2015). Retrieving surface waves from ambient seismic noise using seismic interferometry by multidimensional deconvolution. *Journal of Geophysical Research: Solid Earth*, *120*(2), 944–961.

van IJsseldijk, J., Brackenhoff, J., Thorbecke, J., & Wapenaar, K. (2023a). Time-lapse applications of the Marchenko method on the Troll field. https://doi.org/10.48550/arXiv.2303.10964

van IJsseldijk, J., van der Neut, J., Thorbecke, J., & Wapenaar, K. (2023b). Extracting small time-lapse traveltime changes in a reservoir using primaries and internal multiples after Marchenko-based target zone isolation. *Geophysics*, *88*(2), no 2., R135–R143. https://doi.org/10.1190/geo2022-0227.1

van IJsseldijk, J., & Wapenaar, K. (2021). Discerning small time-lapse traveltime changes by isolating the seismic response of a reservoir using the Marchenko method. *First International Meeting for Applied Geoscience & Energy Expanded Abstracts*, 3449–3453. https://doi.org/10.1190/segam2021-3583007.1

Verschuur, D. J., Berkhout, A. J., & Wapenaar, C. P. A. (1992). Adaptive surface-related multiple elimination. *Geophysics*, *57*(9), 1166–1177. https://doi.org/10.1002/2014JB011262

Wapenaar, K., & van IJsseldijk, J. (2020). Employing internal multiples in time-lapse seismic monitoring, using the Marchenko method. *82nd EAGE Annual Conference & Exhibition, 2020*. https://doi.org/10.3997/2214-4609.202011576

Wapenaar, K., Brackenhoff, J., Dukalski, M., Meles, G., Reinicke, C., Slob, E., Staring, M., Thorbecke, J., van der Neut, J., & Zhang, L. (2021). Marchenko redatuming, imaging, and multiple elimination and their mutual relations. *Geophysics*, *86*(5), WC117–WC140. https://doi.org/10.1190/geo2020-0854.1

Wapenaar, K., & Staring, M. (2018). Marchenko-based target replacement, accounting for all orders of multiple reflections. *Journal of Geophysical Research: Solid Earth*, *123*(6), 4942–4964. https://doi.org/10.1029/2017JB015208

Wapenaar, K., Thorbecke, J., van der Neut, J., Broggini, F., Slob, E., & Snieder, R. (2014). Marchenko imaging. *Geophysics*, *79*(3), WA39–WA57. https://doi.org/10.1190/geo2013-0302.1

Wapenaar, K., Thorbecke, J., van der Neut, J., Slob, E., & Snieder, R. (2017). Review paper: Virtual sources and their responses, part ii: Data-driven single-sided focusing. *Geophysical Prospecting*, *65*(6), 1430–1451. https://doi.org/10.1111/1365-2478.12495

6

CONCLUSIONS AND RECOMMENDATIONS

This chapter will first summarize the most important findings of the previous chapters. Based on these findings some general conclusions will be drawn regarding the Marchenko method and its application to time-lapse monitoring. However, science is never finished, and the second part of this chapter will, therefore, discuss future prospects and research recommendations based on the results presented in this thesis.

6.1. CONCLUSIONS

Chapter 2 presented an adaptation to the iterative Marchenko scheme that is able to correct for imperfectly sampled reflection data. This new scheme utilizes point-spread functions (PSFs) to characterize the blurring of the focusing and Green's functions due to the irregular sampling. Subsequently, these PSFs are deconvolved from the blurred functions in order to retrieve "clean" functions. A numerical example is used to assess the efficacy of the new method. Although the numerical results confirmed that the PSFs are able to correct for missing offsets in the reflection data, it is shown that, for certain models, the new methodology introduced an unstable inversion of the upgoing focusing function. To avoid these instabilities I present a second scheme, which is more universally applicable (i.e. it had the same restrictions as the regular Marchenko scheme). Finally, the new method is compared to reflection data that was interpolated as a preprocessing step. This comparison found that both methods are able to remove artifacts in the final migrated image. The ability to deal with irregular geometries is especially relevant to time-lapse studies as it can aid to suppress 4D repeatability issues.

In Chapter 3, the extrapolated Marchenko equations are used to isolate the target response from the full reflection response. A two-fold strategy is designed that first creates a response without overburden interactions by redatuming the wavefield to a focal level above the target zone. Secondly, the Marchenko method is applied on the new response and the underburden reflections are removed by deconvolving the focusing functions from one another. The final isolated response then provides an unobstructed view of the primary and multiple reflections of the target zone, free from any interference from the over- and underburden effects. Consequently, accurate time-lapse traveltime differences can be extracted from the isolated responses using interferometry, from both the primaries and the multiples. Furthermore, time-lapse changes in the overburden can be eliminated by first calculating the timelag between a reference reflection above the reservoir and a primary or multiple reflection from below. A numerical example indicates that amplitudes of the internal multiples are relatively weak, leading to the calculation of erroneous traveltime differences. However, this problem is circumvented by artificially increasing the amplitudes of the internal multiples. The final time-lapse changes, retrieved with these stronger multiples, provides accurate and complementary information to the primary results. It is, therefore, concluded that time-lapse experiments can benefit from the Marchenko method to remove undesirable reflections from the over- and underburden. Additionally, internal multiples, when used in conjunction with primary results, are able to provide added benefits, as they travel through the reservoir more than once.

Next, Chapter 4 introduces a framework to combine multiphase poromechanical reservoir simulations with time-lapse seismic surveys. A coupled and fully implicit methodology is designed to simulate fluid flow inside a reservoir as well as the related geomechanical changes in the whole subsurface. These simulation results are then translated to seismic parameters via fluid substitution, which enables a finite-difference modeler to compute the reflection response at different times during the simulation. Subsequently, the isolation and extraction methods described in Chapter 3, are used to extract time-lapse traveltime differences. This integrated simulator is tested on two numerical models. First, the methodology is able to almost perfectly predict the location of the fluid front in the reservoir for a simple test case. The second, more complex, model proved to be more challenging, but the method is still able to resolve the general trends of the fluid movement in the reservoir. The experiments in this chapter highlights the importance of simulating the time-lapse changes of the entire subsurface, instead of solely inside the reservoir, as the geomechanical changes played a significant role inside as well as outside the reservoir.

Finally, Chapter 5 discusses the implementation of the previously mentioned time-lapse isolation and extraction strategy on a marine dataset of the Troll field just off the Norwegian coast. Before applying the Marchenko method a velocity model is estimated, and the reflection data are scaled to ensure convergence of the iterative Marchenko scheme. The limited recording time of the reflection data caused an additional complication, as it meant that the internal multiples of the target zone were not actually recorded. Fortunately, it is discovered that these multiples can be reconstructed with the Marchenko method, provided that the focal depth is carefully chosen to not include any of the missing multiples. The results show that the isolated response is able to clarify the reflections and removed some noise related to the overburden. Moreover, the extracted time-lapse traveltime differences display remarkable similarities independent on what primary or multiple is used. In the end, the additional information provided by the multiples improves the confidence of the final time-lapse results.

In conclusion, this thesis set out to further develop the Marchenko method for time-lapse applications, and it provides promising results for more accurate monitoring of subsurface fluid flows. It was found that the extrapolated Marchenko equations provide a straightforward technique to remove undesirable reflections from the reflection response. Moreover, Marchenko-based isolation proved to be a powerful tool to monitor time-lapse changes in a specific target zone. Additionally, multidimensional deconvolutions are surprisingly stable when used to redatum the wavefield to the focal level, even when applied to field data. Finally, it was shown that internal multiples are not solely a nuisance to be removed from the data, but that they can provide complementary time-lapse information, which may be missed when only primaries are used. Even though some of the potential for time-lapse monitoring is unlocked in this thesis, exciting opportunities and daunting limitations still remain before the methodology can be more widely adopted in the field of geophysics, which will be discussed in the next section.

6.2. FUTURE OUTLOOK

There is a nearly endless list of possible improvements to the methodology proposed in this thesis, this section will focus on the most pressing issues that currently prevent the widespread use of the Marchenko method in general as well as for time-lapse applications specifically.

One major inhibitor, discussed in Chapter 5 and Appendix A, is the strict requirement imposed on the reflection data for the Marchenko method, as the amplitudes have to be carefully scaled to ensure convergence and thus proper multiple removal. For the synthetic examples this is not an issue, as the exact scaling of the modeled response is known. Contrarily, for field data a number of unknown scaling factors have to be corrected for. The first error is introduced when the, oftentimes unknown, source signature is removed from the data. Next, interpolation of near- and other missing offsets is able to recover gaps in the data, but the interpolated events display more erroneous scaling. Additionally, line field data are measured in a 3D subsurface, which requires a correction for the geometrical spreading, and absorption in the subsurface will dampen the wavefield. Brackenhoff (2016) estimates the scaling factor based on minimizing the energy of the internal multiples in the data. This method, however, oftentimes fails to converge on field data due to noise or a lack of internal multiples. Alternatively, Staring et al. (2021) find a scaling factor as a pre-processing step by matching surface-related multiples predicted from the scaled data with the actual multiples found in the data. For this method to work, the surface-related multiples are required to be present in the data, hence this method is ideal for surveys with a shallow water layer. Finally, Dukalski and Reinicke (2022) provide a more accurate method to correct for geometrical spreading, which currently is limited to 1.5D media. Ideally, a more universal procedure to correct for distorted amplitudes is developed that can be added to the pre-processing workflow of the reflection data. However, as the problem is dependent on the geology of the subsurface, this may not be feasible. In that case, a set of more general rules of thumb for scaling corrections should at the very least be investigated to make the Marchenko method more accessible.

The current time-lapse methodology sequentially applies the Marchenko-based isolation first to the baseline and second to the monitor study. However, it has been shown that simultaneous inversion of time-lapse data can be beneficial (e.g. Qu & Verschuur, 2020). The advantage of such a joint process is that the static part of the data is inverted simultaneously with the dynamic time-lapse part, which leads to a more robust inversion with reduced 4D repeatability issues. Haindl et al. (2021) present a Marchenko-based joint inversion, which could be considered as a first step towards a methodology that is able to jointly isolate the target response in time-lapse data.

Currently, the time-lapse extraction method proposed here only utilizes zero-offset data, whereas the full 2D offsets are available. Consequently, a large amount of information is presently wasted. Moreover, time-lapse methods oftentimes require amplitude versus offset information to retrieve reservoir dynamic properties. An inversion for velocity and reservoir thickness, would also require more than solely zero-offset information. Future research should, therefore, look into how to make use of this wealth of information that is not yet used, and focus on the development of new applications that deal with this information.

Another common strategy in time-lapse seismic is using P-wave and S-wave impedance cross-plots to convert seismic parameters into reservoir dynamic properties. The current Marchenko scheme is limited to the acoustic case, hence it is unable to retrieve any elastic parameters from the data. Extending the scheme to elastic scenarios is complicated, because the causality constraint, used to separate focusing and Green's functions, no longer holds due to the presence of converted waves. Development of a full elastic Marchenko method is currently researched (da Costa Filho et al., 2014; Reinicke et al., 2020), and would be beneficial for time-lapse applications. Alternatively, the reflection data can be decomposed into a P-wave and a S-wave dataset, to which the Marchenko method can be applied individually.

Lastly, this thesis explored the relation between forward reservoir simulation and seismic modeling, to link reservoir dynamic properties to seismic parameters. The inverse of this process, retrieving dynamic reservoir properties from seismic data, is even more essential and valuable for monitoring of reservoirs. As mentioned before, current state-of-the-art time-lapse methods rely on amplitude versus offset and/or elastic data to find the pressure and saturation in the reservoir (Landrø, 2001; Trani et al., 2011). Additionally, it would be interesting to see if the internal multiples can provide any new insights into retrieval of reservoir properties. Another point to consider for time-lapse methods in general is how to differentiate between the various properties, such that time-lapse differences can be related to saturation, pressure or geomechanical changes in the subsurface.

If these concerns are properly addressed, the Marchenko method will be able to significantly improve time-lapse monitoring of reservoirs and other specific targets in the subsurface.

REFERENCES

Brackenhoff, J. (2016). *Rescaling of incorrect source strength using Marchenko redatuming* [Master's thesis, TU Delft repository, Delft University of Technology] [http://resolver.tudelft.nl/uuid:0f0ce3d0-088f-4306-b884-12054c39d5da, accessed 11 August 2022].

da Costa Filho, C. A., Ravasi, M., Curtis, A., & Meles, G. A. (2014). Elastodynamic Green's function retrieval through single-sided Marchenko inverse scattering. *Phys. Rev. E*, *90*, 063201. https://doi.org/10.1103/PhysRevE.90.063201

Dukalski, M., & Reinicke, C. (2022). Marchenko Multiple Elimination using conventional vs advanced 3-D to 2-D conversion on marine data. *83rd EAGE Annual Conference & Exhibition, 2022*. https://doi.org/10.3997/2214-4609.202210182

Haindl, C., Ravasi, M., & Broggini, F. (2021). Handling gaps in acquisition geometries — Improving Marchenko-based imaging using sparsity-promoting inversion and joint inversion of time-lapse data. *Geophysics*, *86*(2), S143–S154. https://doi.org/10.1190/geo2020-0036.1

Landrø, M. (2001). Discrimination between pressure and fluid saturation changes from time-lapse seismic data. *Geophysics*, *66*(3), 836–844. https://doi.org/10.1190/1.1444973

Qu, S., & Verschuur, D. J. (2020). Simultaneous joint migration inversion for high-resolution imaging/inversion of time-lapse seismic datasets. *Geophysical Prospecting*, *68*(4), 1167–1188. https://doi.org/10.1111/1365-2478.12918

Reinicke, C., Dukalski, M., & Wapenaar, K. (2020). Comparison of monotonicity challenges encountered by the inverse scattering series and the Marchenko demultiple method for elastic waves. *Geophysics*, *85*(5), Q11–Q26. https://doi.org/10.1190/geo2019-0674.1

Staring, M., Dukalski, M., Belonosov, M., Baardman, R. H., Yoo, J., Hegge, R. F., van Borselen, R., & Wapenaar, K. (2021). Robust estimation of primaries by sparse inversion and Marchenko equation-based workflow for multiple suppression in the case of a shallow water layer and a complex overburden: A 2D case study in the Arabian Gulf. *Geophysics*, *86*(2), Q15–Q25. https://doi.org/10.1190/geo2020-0204.1

Trani, M., Arts, R., Leeuwenburgh, O., & Brouwer, J. (2011). Estimation of changes in saturation and pressure from 4D seismic AVO and time-shift analysis. *Geophysics*, *76*(2), C1–C17. https://doi.org/10.1190/1.3549756

A

APPLICATION OF VIRTUAL SEISMOLOGY TO DAS AND GEOPHONE DATA IN GRONINGEN

In this appendix practical aspects are discussed for applying virtual seismology via the Marchenko method to DAS data on a survey in Groningen, The Netherlands. Virtual seismology allows to retrieve the Green's function between a virtual source at an arbitrary focal point in the subsurface, while accounting for all orders of multiples. The method only requires the reflection response at the surface and an estimate of the traveltime between the surface and focal point. However, in order to successfully apply the method the reflection response needs to be free from surface waves as well as properly scaled in order for the Marchenko equations to converge, these limitations severely complicate the application of the Marchenko method to field data, especially seismic surveys on land. This appendix considers a full 2D geophone survey as well as a 1.5D approximation for the DAS data, and compares the results of the virtual sources with an actual dynamite source. The results show that virtual seismology can be used to recreate the reflections recorded at the surface from the dynamite source using both geophone and DAS data.

This appendix is available on arXiv: van IJsseldijk, J., Al Hasani, M., Verschuur, E., Drijkoningen, G., & Wapenaar, K. (2023). Application of virtual seismology to DAS data in Groningen. https://doi.org/10.48550/arXiv.2305.13407
Minor modifications have been applied to keep consistency within this thesis.

A.1. INTRODUCTION

Seismic reflection data at the Earth's surface can be employed to create responses to virtual sources in the subsurface, observed by virtual receivers in the subsurface and physical receivers at the surface (Brackenhoff et al., 2022; Wapenaar et al., 2018). This methodology, which we call "Virtual Seismology", is based on the 3D Marchenko method (Broggini et al., 2014; Wapenaar et al., 2014). The retrieved virtual responses consist not only of direct waves and primary reflections, but also contain all internal multiple reflections. Virtual seismology can be used to forecast responses to induced earthquakes (Brackenhoff et al., 2019a, 2019b). Here we discuss our results of retrieving virtual seismic responses from reflection data obtained with an electrically driven seismic vibrator as a source and optical fibers with a laser interrogator (distributed acoustic sensing, DAS) as multi-component receivers.

A.2. DATA ACQUISITION

We briefly discuss the data acquisition. For a more extensive discussion we refer to Al Hasani and Drijkoningen (2023). A seismic line has been deployed in the province Groningen (The Netherlands), at 53°9'16.12"N, 6°50'53.99"E (Figure A.1). An electrically driven seismic vibrator, based on linear motor technology (Noorlandt et al., 2015) was used at every 2 m along a source line of 750 m. At each position the source was driven with a sweep signal from 2 to 180 Hz. Straight and helically wound fiber-optic cables were buried along the same line and two different types of interrogators were used to record the seismic responses at every meter with a gauge length of 2 m. Using the two types of cables allows retrieval of the horizontal and vertical strain rates (Al Hasani & Drijkoningen, 2023). Along a part of the line, vertical-component geophones were deployed at every 4 m, for reference. Figure A.2 shows a common-receiver gather (CRG) for a receiver at 173 m, after preprocessing. The red and yellow boxes show shallow and deep P-wave reflection events, whereas the event in the green box is interpreted as a P-to-S reflection event. Moreover, a borehole was drilled at 375 m and dynamite sources were ignited at depths of 90 m, 95 m and 100 m as a reference for the virtual-source responses that will be discussed later. Figure A.3 shows the response of a dynamite source at 100 m depth, registered by geophones at the surface. The goal of this work is to virtually recreate this response from the reflection data measured at the surface by means of the Marchenko method.

A.3. DATA PRE-PROCESSING

The raw data were correlated with the source sweep to remove the source signature from the raw data. Before the Marchenko method can be applied the reflection data need to be prepared further. This pre-processing includes removing the direct arrivals and ground roll from the data as well as applying the proper scaling required for the Marchenko scheme.

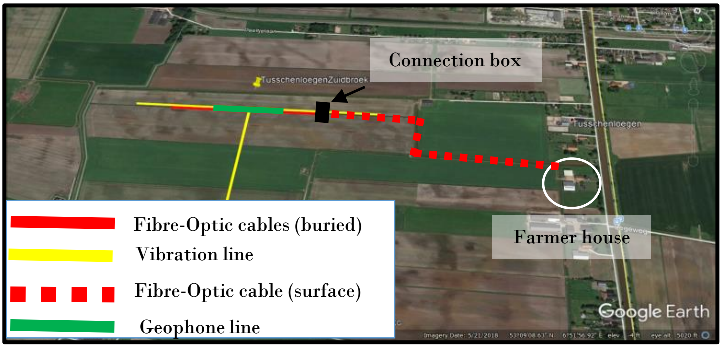

Figure A.1: Field map with the position of the fiber cables (surface and buried), geophone line and source line. Adapted from Al Hasani and Drijkoningen (2023).

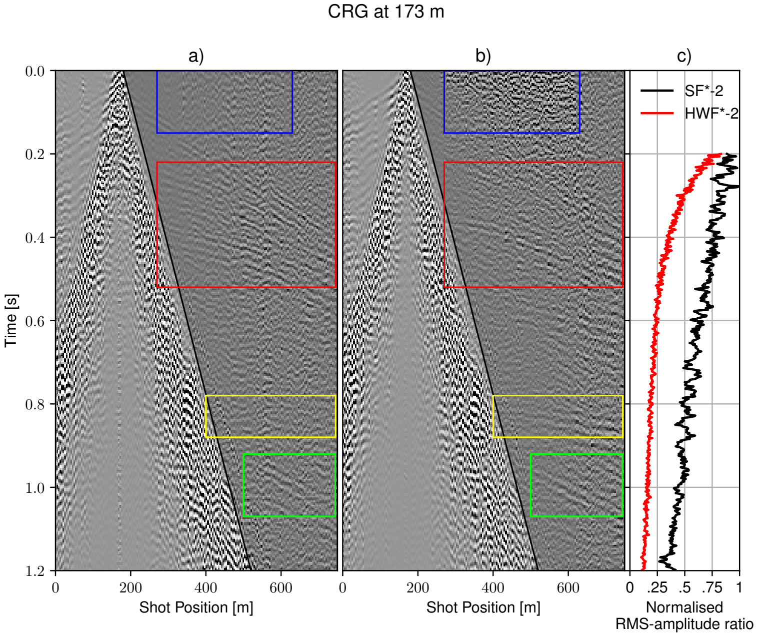

Figure A.2: Common-receiver gather (CRG) at 173 m of (a) straight fiber and (b) helically wound fiber, and (c) their normalized RMS values as a function of time (outside the surface-wave cones). Adapted from Al Hasani and Drijkoningen (2023).

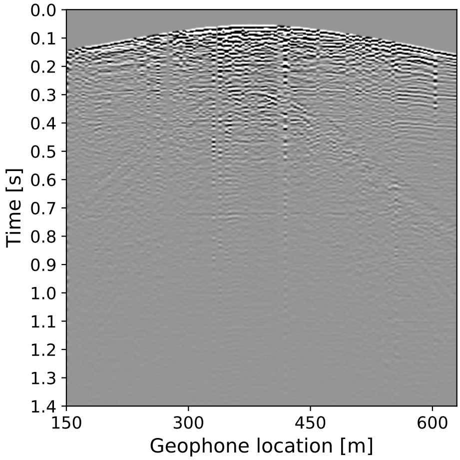

Figure A.3: Response to dynamite source at (x,z)=(375,100)m, registered by vertical-component geophones at the surface.

A.3.1. GROUND ROLL MUTE AND INTERPOLATION

The surface waves, as seen inside of the cone in Figure A.2, were muted. Thereafter, normal-moveout (NMO) was applied to align the hyperbolic reflections in the data. Next, the data were transformed to the Radon domain to interpolate the muted part of the data (Kabir & Verschuur, 1995). Finally, the NMO correction is undone to acquire the interpolated data-set free from surface waves. Figure A.4 shows this interpolation applied to three common-source gathers (CSG) on the geophone line. The first CSG of the geophone line in the left panel of Figure A.4 contains more reflections than can be identified in the last CSG, the right-most panel. This is likely caused due to the final shot being located on loose soil, resulting in worse coupling of the source with the earth.

The quality of the DAS data was varying at different source locations, meaning that the resolution of P-wave reflections was sub-par for a number of the CSGs. It was, therefore, decided to create a 1.5D reflection response from a single helically wound fiber CSG with clearly defined reflections instead of using all DAS CSGs. For this purpose the CRG at 173 m (Figure A.2) was selected. This gather was mirrored to create the symmetric gather as shown in Figure A.5. Once again, the ground roll is muted and interpolated using the Radon transform on the NMO-corrected CSG. After undoing the NMO, the interpolated gather is shown on the right in Figure A.5. From this gather the full 578 m by 578 m reflection response is produced, with 289 shots and a fixed spread of 289 receivers. Since the single CSG is used for all source positions, the reflector at 0.8 s as well as the P-to-S reflection will be clearly visible in all CSGs, contrary to the CSGs of the geophone line that differ in resolution between different shot locations.

A.3.2. SCALING CORRECTION OF THE REFLECTION DATA

In order for the Marchenko method to converge, the amplitude of the reflection data have to be properly scaled. Firstly, to correct for 3D geometrical spreading (approxi-

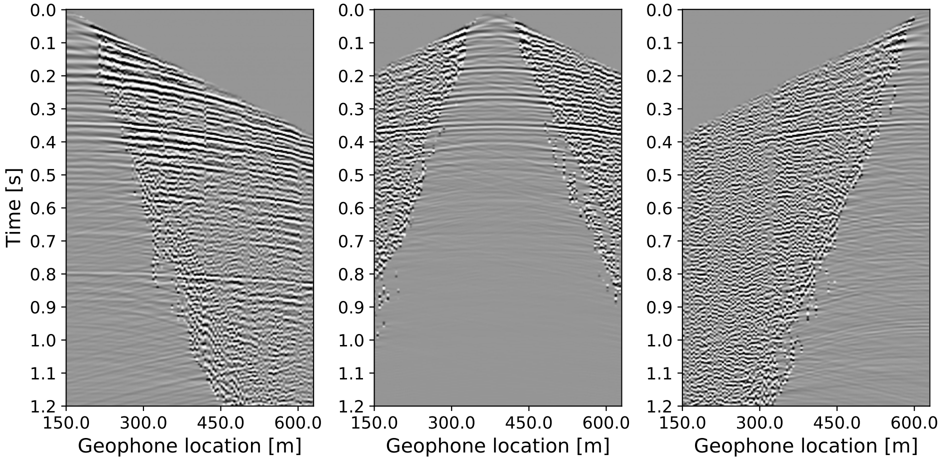

Figure A.4: From left to right, the first, middle and last common-source gather (CSG) on the geophone line after ground roll mute and Radon interpolation.

mately $1/t$) on the 2D ($\approx 1/\sqrt{t}$) scheme a factor of $\sqrt{t}$ is applied to the data. Next, we correct for absorption effects and other effects that are for example related to the source signature or the interpolation. This is achieved by minimizing the cost functions as described in Brackenhoff (2016). Different gains and linear factors are considered to find an optimal factor of the form ae^{bt}, where a is a linear factor and b a time-dependent exponential gain. However, there are other factors, such as amplitude versus offset behaviour, that have not been considered, meaning that the final scaling factor may not give the optimal results. The consequences and limitations of these decisions will be discussed at the end of this appendix.

A.4. APPLICATION OF VIRTUAL SEISMOLOGY

The next step before applying virtual seismology is finding an estimate of the traveltime between the focal point and the surface. Here, this is achieved by finite-difference modeling the Green's function between the receivers on the surface and the focal point at x = 375 m and a depth of 100 m (i.e. at the same location as the dynamite source). Subsequently, the first arrival of this Green's function is time-reversed, and used as initial estimation of the focusing function for the Marchenko method. The iterative Marchenko scheme is then used to find the upgoing- and downgoing-Green's functions between the focal point and the surface (Thorbecke et al., 2017). These decomposed Green's functions are summed to find the two-way Green's function, which can then be compared with the response to the dynamite shot at depth, shown in the left of Figure A.6. The results of 8 iterations applied to the geophone data is shown in the middle panel of this figure. The reflection at 0.3 s, marked by a blue arrow, is clearly visible in both gathers. Furthermore, the red arrows show some similarities after the direct arrival of the Green's function. The rightmost gather of Figure A.6 shows the results of applying the

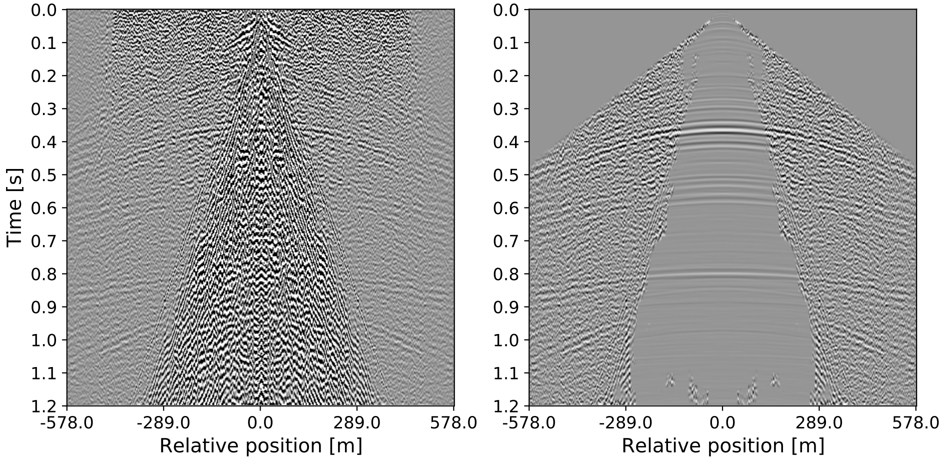

Figure A.5: On the left, CRG from the DAS data in Figure A.2, the mirror image of the same gather is added to create a symmetric CSG, the full 1.5D reflection response is created from this CSG. The right panel shows the same CSG after ground roll mute and Radon interpolation.

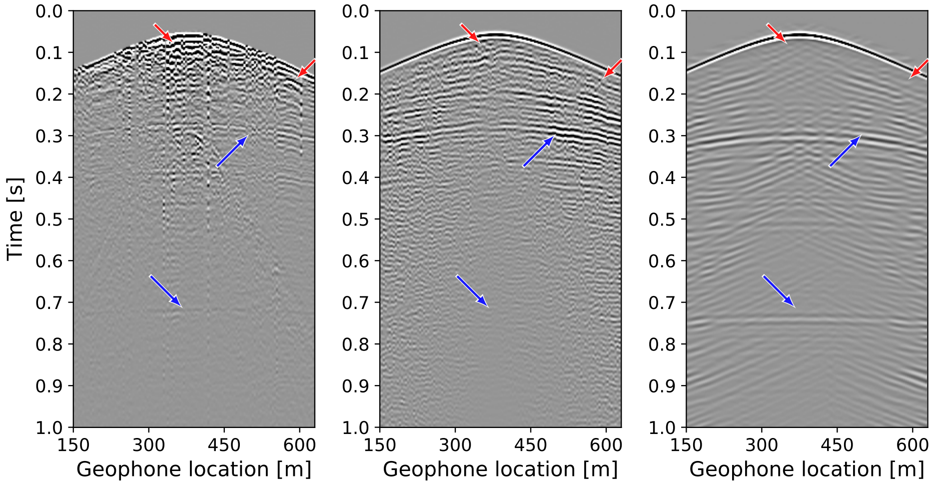

Figure A.6: From left to right: reference dynamite shot at 100 m depth (same as Figure A.3), virtual shot at 100 m from the geophone data and the same virtual shot acquired with the DAS data. The blue arrows indicate the first and second primary event.

Marchenko scheme to the DAS data. Now the second reflection at approximately 0.8 s, marked by a second blue arrow, is also apparent in the data, contrary to the geophone results. This result is explained by the fact that the 1.5D DAS data contains two obvious reflections at 0.4 s and 0.8 s, whereas this second reflection at 0.8 s is not always visible in all the geophone CSGs. The downside of using a 1.5D approximation for the DAS data is that it is unable to resolve finer details, which is especially apparent after the direct arrival (red arrows); the geophone results are able to resolve some heterogeneity in the signal here, whereas the DAS results display no similarities with the dynamite shot at the same traveltimes.

A.5. DISCUSSION AND CONCLUSIONS

In this appendix we assessed the feasibility of applying our virtual seismology methodology to seismic land datasets of geophone as well as DAS recordings. A number of challenges need to be overcome to properly apply the method. Firstly, the direct and surface waves need to be removed from the data, which was achieved by applying a strict mute to eliminate the ground roll and interpolating the subsequent gap in the Radon domain. The second challenge is finding the correct scaling of the reflection response, in order for the Marchenko scheme to converge to a solution, and ensure that internal multiples are properly accounted for.

The surface waves are easily removed by the mute, and the interpolation was able to reconstruct the hyperbolic reflections in the data. The downside of this method is that near-surface reflections that mostly overlap with the ground roll will be destroyed in the process. This means that a valuable part of the data is lost, and internal multiples from these reflectors can no longer be resolved with the Marchenko method. Future research should consider how these reflections can be preserved or recreated from their multiple reflections, especially because the near-surface can be a prolific source of internal multiples. A secondary consequence of the Radon interpolation is the inaccurate amplitudes of the interpolated reflections, we hope to compensate for this effect by applying the scaling factors.

The scaling factors are designed to compensate for a number of factors that reduce the accuracy of the amplitude in the data. Nevertheless they are far from perfect, and aside from the previously mentioned loss of accuracy due to the interpolation, there are a number of additional parameters to consider. Firstly, the geometrical spreading estimation is not fully accurate, as Dukalski and Reinicke (2022) show. Another scaling error is introduced by the fact that the formulation of the Marchenko equations assumes a dipole source (F_z) with monopole receivers (P), or via reciprocity a monopole source (Q) with dipole receiver (v_z). On the contrary, our survey has both a dipole source as well as dipole receivers. Moreover, wavefield damping and imperfect source signature removal are other causes of erroneous amplitudes in the reflection data. On the one hand, all these factors are mainly linear or time-dependent, and can, therefore, be corrected using a formulation with some linear and some time-dependent scaling factors. On the other hand, erroneous amplitude versus offset effects are not accounted for in our formulation, thus they are likely to cause bigger issues. These changes become especially relevant when considering DAS data, as the helically wound fiber-optic lines measure a combination of vertical and horizontal strain rather than the vertical particle velocity measured by the geophones. While the vertical strain can, in theory, be retrieved using both the helically wound and straight fiber recordings, the exact relation between these two measurements remains uncertain (Al Hasani & Drijkoningen, 2023). Moreover, the resulting strain-rate would still contain a spatial derivative compared to the vertical particle velocity measured by the geophones. Ultimately, future research is required to more carefully study the effects of different scaling errors in the data, and how to properly correct for each one of them.

One of the issues that has not been discussed before is the error in the approximation of the initial focusing function. Specifically, forward-scattering, due to diffractions or other sharp discontinuities, means that estimating the initial focusing function with the direct arrival of the Green's function is no longer accurate. These effects can be seen in the first event of the dynamite source (Figure A.3), which is not continuous everywhere. van der Neut et al. (2022) propose an adaption to the Marchenko equations with transmission data to correct for these deviations. In theory, a similar approach using the direct arrival of the dynamite shot can be used to update the estimated Green's functions in this study. However, the method does not take into account velocities contrasts, hence the application to the current study remains challenging.

Next, the current formulation does not take into account free-surface multiples, because the subsurface is relatively unconsolidated and minimal surface-related multiples are expected. However, in the case of seismic surveys on a more solid underground these multiples will become more relevant. In this case a formulation that includes free-surface multiples might be required (Singh et al., 2017), or alternatively the free-surface multiples have to be removed before applying the method by means of for example surface-related multiple elimination (Verschuur et al., 1992).

A final concern is the fact that the Marchenko method that was used is designed for acoustic wavefields, whereas the data was recorded in an elastic medium. Reinicke et al. (2021) conclude that while elastic effects have a substantial impact on the results of the Marchenko method, their impact is limited and unlikely to alter interpretation of migrated sections. Moreover, current research is aimed at developing elastic adaptations of the Marchenko method (Reinicke & Wapenaar, 2019).

To conclude, we have found that the virtual seismology methodology can be used to redatumed wavefields in the subsurface, and virtually estimate the response to a dynamite source at depth, observed at the surface. This estimation is achieved solely with the reflection response at the surface, and an estimation of the direct Green's function between the focal depth and the surface. It was shown that this was possible using geophone as well as DAS data. Future research should mainly focus on how the data can be scaled in order for the Marchenko scheme to properly converge. Such research should examine how to deal with linear, time-dependent and offset-dependent scaling errors in the reflection data. Additionally, the results can be further improved if the near-surface reflections can be resolved better, as a majority of the internal multiples are oftentimes generated here.

REFERENCES

Al Hasani, M., & Drijkoningen, G. (2023). Experiences with distributed acoustic sensing using both straight and helically wound fibers in surface-deployed cables

- a case history in groningen, the netherlands. *Geophysics*, *just accepted*, 1–53. https://doi.org/10.1190/geo2022-0769.1

Brackenhoff, J. (2016). *Rescaling of incorrect source strength using Marchenko redatuming* [Master's thesis, TU Delft repository, Delft University of Technology] [http://resolver.tudelft.nl/uuid:0f0ce3d0-088f-4306-b884-12054c39d5da, accessed 11 August 2022].

Brackenhoff, J., Thorbecke, J., & Wapenaar, K. (2019a). Monitoring of induced distributed double-couple sources using Marchenko-based virtual receivers. *Solid Earth*, *10*(4), 1301–1319. https://doi.org/10.5194/se-10-1301-2019

Brackenhoff, J., Thorbecke, J., & Wapenaar, K. (2019b). Virtual sources and receivers in the real earth: Considerations for practical applications. *Journal of Geophysical Research: Solid Earth*, *124*(11), 11802–11821. https://doi.org/10.1029/2019JB018485

Brackenhoff, J., Thorbecke, J., & Wapenaar, K. (2022). 3-D virtual seismology. *IEEE Transactions on Geoscience and Remote Sensing*, *60*, 4702015. https://doi.org/10.1109/tgrs.2021.3076292

Broggini, F., Wapenaar, K., van der Neut, J., & Snieder, R. (2014). Data-driven Green's function retrieval and application to imaging with multidimensional deconvolution. *Journal of Geophysical Research: Solid Earth*, *119*(1), 425–441. https://doi.org/10.1002/2013JB010544

Dukalski, M., & Reinicke, C. (2022). Marchenko Multiple Elimination using conventional vs advanced 3-D to 2-D conversion on marine data. *83rd EAGE Annual Conference & Exhibition, 2022*. https://doi.org/10.3997/2214-4609.202210182

Kabir, M. N., & Verschuur, D. (1995). Restoration of missing offsets by parabolic Radon transform. *Geophysical Prospecting*, *43*(3), 347–368. https://doi.org/10.1111/j.1365-2478.1995.tb00257.x

Noorlandt, R., Drijkoningen, G., Dams, J., & Jenneskens, R. (2015). A seismic vertical vibrator driven by linear synchronous motors. *Geophysics*, *80*(2), EN57–EN67. https://doi.org/10.1190/geo2014-0295.1

Reinicke, C., Dukalski, M., & Wapenaar, K. (2021). Internal multiple elimination: Can we trust an acoustic approximation? *Geophysics*, *86*(5), WC41–WC54. https://doi.org/10.1190/geo2020-0850.1

Reinicke, C., & Wapenaar, K. (2019). Elastodynamic single-sided homogeneous Green's function representation: Theory and numerical examples. *Wave Motion*, *89*, 245–264. https://doi.org/10.1016/j.wavemoti.2019.04.001

Singh, S., Snieder, R., van der Neut, J., Thorbecke, J., Slob, E., & Wapenaar, K. (2017). Accounting for free-surface multiples in Marchenko imaging. *Geophysics*, *82*(1), R19–R30. https://doi.org/10.1190/geo2015-0646.1

Thorbecke, J., Slob, E., Brackenhoff, J., van der Neut, J., & Wapenaar, K. (2017). Implementation of the Marchenko method. *Geophysics*, *82*(6), WB29–WB45. https://doi.org/10.1190/GEO2017-0108.1

van der Neut, J., Brackenhoff, J., Meles, G., Zhang, L., Slob, E., & Wapenaar, K. (2022). On the retrieval of forward-scattered waveforms from acoustic reflection and transmission data with the Marchenko equation. *IEEE Transactions on Ultra-*

sonics, Ferroelectrics, and Frequency Control, *69*(5), 1775–1786. https://doi.org/10.1109/TUFFC.2022.3163906

van IJsseldijk, J., Al Hasani, M., Verschuur, E., Drijkoningen, G., & Wapenaar, K. (2023). Application of virtual seismology to DAS data in Groningen. https://doi.org/10.48550/arXiv.2305.13407

Verschuur, D. J., Berkhout, A. J., & Wapenaar, C. P. A. (1992). Adaptive surface-related multiple elimination. *Geophysics*, *57*(9), 1166–1177. https://doi.org/10.1002/2014JB011262

Wapenaar, K., Brackenhoff, J., Thorbecke, J., Van Der Neut, J., Slob, E., & Verschuur, E. (2018). Virtual acoustics in inhomogeneous media with single-sided access. *Scientific reports*, *8*(1), 2497. https://doi.org/10.1038/s41598-018-20924-x

Wapenaar, K., Thorbecke, J., van der Neut, J., Broggini, F., Slob, E., & Snieder, R. (2014). Marchenko imaging. *Geophysics*, *79*(3), WA39–WA57. https://doi.org/10.1190/geo2013-0302.1

B

DERIVATION OF KEY EQUATIONS FROM RECIPROCITY THEOREMS

B.1. INTRODUCTION

In this appendix the fundamental equations used throughout this thesis are derived. First, the one-way reciprocity theorems of the correlation and convolution type are introduced, which will form the basis of the derivations. Next, the Green's function representations of the Marchenko method are derived from two states, one of which is defined in the truncated medium and the other in the full medium. The equations are then convolved with the direct arrival transmission response to find the extrapolated representations. Finally, the regular and extrapolated equations for over- and underburden removal are derived from the focusing- and Green's functions.

B.2. ONE-WAY RECIPROCITY THEOREMS

The principle of the reciprocity theorems is that two acoustic states can be related to one another. A preferential direction along the z-axis can be assumed, due to the layering of the subsurface. If an infinite radius is also introduced, a volume is created that is only bounded on the top ($\partial\mathbb{D}_i$) and bottom ($\partial\mathbb{D}_j$). Let us consider the case where the lossless medium inside these boundaries is the same for both states, and is also absent of any sources or sinks. Hence, only the wavefields propagating through the boundaries need to be considered, $\mathbf{p}_A^\pm$ and $\mathbf{p}_B^\pm$ for state A and B. The superscript − and + denote an upgoing or downgoing wavefield, respectively. The flux-normalized one-way reciprocity theorem of the convolution type then reads (Wapenaar & Grimbergen, 1996):

$$\int_{\partial\mathbb{D}_i}\{(\mathbf{p}_A^+)^t\mathbf{p}_B^- - (\mathbf{p}_A^-)^t\mathbf{p}_B^+\}d\mathbf{x} = \int_{\partial\mathbb{D}_j}\{(\mathbf{p}_A^+)^t\mathbf{p}_B^- - (\mathbf{p}_A^-)^t\mathbf{p}_B^+\}d\mathbf{x}, \tag{B.1}$$

and the reciprocity theorem of the correlation type reads:

$$\int_{\partial\mathbb{D}_i}\{(\mathbf{p}_A^+)^\dagger\mathbf{p}_B^+ - (\mathbf{p}_A^-)^\dagger\mathbf{p}_B^-\}d\mathbf{x} = \int_{\partial\mathbb{D}_j}\{(\mathbf{p}_A^+)^\dagger\mathbf{p}_B^+ - (\mathbf{p}_A^-)^\dagger\mathbf{p}_B^-\}d\mathbf{x}. \tag{B.2}$$

In these equations superscripts t and † denote the transpose and adjoint operations, respectively. Moreover, in the second equation (B.2) evanescent waves are no longer accounted for. Note that both these reciprocity theorems are general for any wave phenomenon, whereas if only the acoustic case is considered, the matrices reduce to scalar functions, making the transpose operation obsolete. The source-receiver reciprocity relations for the one-way Green's functions are then as follows (Wapenaar & Grimbergen, 1996):

$$\mathbf{G}^{-,+}(\mathbf{x}',\mathbf{x},\omega) = \{\mathbf{G}^{-,+}(\mathbf{x},\mathbf{x}',\omega)\}^t, \tag{B.3}$$

$$\mathbf{G}^{+,-}(\mathbf{x}',\mathbf{x},\omega) = \{\mathbf{G}^{+,-}(\mathbf{x},\mathbf{x}',\omega)\}^t, \tag{B.4}$$

$$\mathbf{G}^{-,-}(\mathbf{x}',\mathbf{x},\omega) = -\{\mathbf{G}^{+,+}(\mathbf{x},\mathbf{x}',\omega)\}^t. \tag{B.5}$$

In these equations the first and second coordinates ($\mathbf{x}$) denote the receiver and source coordinates, respectively. The same goes for the superscripts, which also show if the wavefield is upgoing (−) or downgoing (+). Furthermore, ω is the frequency. The reflection response at the surface can be seen as a special case of Equation B.3 (with source and receiver positions on the surface), hence:

$$\mathbf{R}(\mathbf{x}',\mathbf{x},\omega) = \{\mathbf{R}(\mathbf{x},\mathbf{x}',\omega)\}^t. \tag{B.6}$$

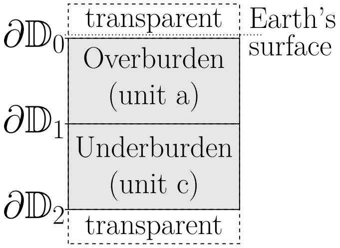

Figure B.1: Schematic overview of the different units and layer boundaries in the model. The top and bottom of the model are transparent, hence they do not reflect any waves back into the either units.

Table B.1: States for deriving the Green's function representations. State A is defined in the actual medium, with a source at $\mathbf{x}_R$ just above $\partial\mathbb{D}_0$. State B is chosen in the truncated medium with focus $\mathbf{x}'$ at $\partial\mathbb{D}_1$.

(a) State A: Full medium *ac*

$\partial\mathbb{D}_0$	$\mathbf{p}_A^+(\mathbf{x},\omega) = \mathbf{I}\delta(\mathbf{x}_H - \mathbf{x}_{H,R})$ $\mathbf{p}_A^-(\mathbf{x},\omega) = \mathbf{R}_{ac}(\mathbf{x},\mathbf{x}_R,\omega)$
$\partial\mathbb{D}_1$	$\mathbf{p}_A^+(\mathbf{x},\omega) = \mathbf{G}^{+,+}(\mathbf{x},\mathbf{x}_R,\omega)$ $\mathbf{p}_A^-(\mathbf{x},\omega) = \mathbf{G}^{-,+}(\mathbf{x},\mathbf{x}_R,\omega)$

(b) State B: Overburden only *a*

$\partial\mathbb{D}_0$	$\mathbf{p}_B^+(\mathbf{x},\omega) = \mathbf{F}^+(\mathbf{x},\mathbf{x}',\omega)$ $\mathbf{p}_B^-(\mathbf{x},\omega) = \mathbf{F}^-(\mathbf{x},\mathbf{x}',\omega)$
$\partial\mathbb{D}_1$	$\mathbf{p}_B^+(\mathbf{x},\omega) = \mathbf{I}\delta(\mathbf{x}_H - \mathbf{x}'_H)$ $\mathbf{p}_B^-(\mathbf{x},\omega) = 0$

These relations will become relevant in the derivations in the upcoming sections, where the model in Figure B.1 is considered. This model has an overburden *a* and an underburden *c*, bounded by $\partial\mathbb{D}_0$ and $\partial\mathbb{D}_2$, and separated by $\partial\mathbb{D}_1$. The layers above the Earth's surface are transparent, implying that there are no free-surface multiples in the model. The layers below $\partial\mathbb{D}_2$ are also transparent, hence no waves are reflected back into the model from either the top or bottom.

B.3. GREEN'S FUNCTION REPRESENTATIONS

To derive the Green's function representations state A is defined in the full medium, and state B is taken in the truncated medium (i.e. only the overburden, with the overburden replaced by a transparent medium). In state A taking a source just above $\partial\mathbb{D}_0$ gives the downgoing wavefield $\mathbf{p}_A^+(\mathbf{x},\omega)$ is represented with $\mathbf{I}\delta(\mathbf{x}_H - \mathbf{x}_{H,R})$, with H denoting the horizontal coordinates, i.e. $\mathbf{x}_H = (x_1, x_2)$. The response to this impulse gives $\mathbf{p}_A^-(\mathbf{x},\omega) = \mathbf{R}_{ac}(\mathbf{x},\mathbf{x}_R,\omega)$, the Green's functions define the wavefields at $\partial\mathbb{D}_1$. Second, state B considers for $\mathbf{p}_B^+(\mathbf{x},\omega)$ at $\partial\mathbb{D}_0$ the downgoing focusing function $\mathbf{F}^+(\mathbf{x},\mathbf{x}',\omega)$, and response $\mathbf{F}^-(\mathbf{x},\mathbf{x}',\omega)$ as $\mathbf{p}_B^-(\mathbf{x},\omega)$. These focusing functions have a focal depth at $\partial\mathbb{D}_1$, hence here $\mathbf{p}_B^+(\mathbf{x},\omega) = \mathbf{I}\delta(\mathbf{x}_H - \mathbf{x}'_H)$. These states are summarized in Table B.1. Using the states in the table together with Equations B.1, with $\partial\mathbb{D}_i = \partial\mathbb{D}_0$ and $\partial\mathbb{D}_j = \partial\mathbb{D}_1$, B.6 and B.3 (Slob et al., 2014; Wapenaar et al., 2014):

$$\mathbf{G}^{-,+}(\mathbf{x}_R,\mathbf{x}',\omega) + \mathbf{F}^-(\mathbf{x}_R,\mathbf{x}',\omega) = \int_{\partial\mathbb{D}_0} \mathbf{R}_{ac}(\mathbf{x}_R,\mathbf{x},\omega)\mathbf{F}^+(\mathbf{x},\mathbf{x}',\omega)\,d\mathbf{x}, \tag{B.7}$$

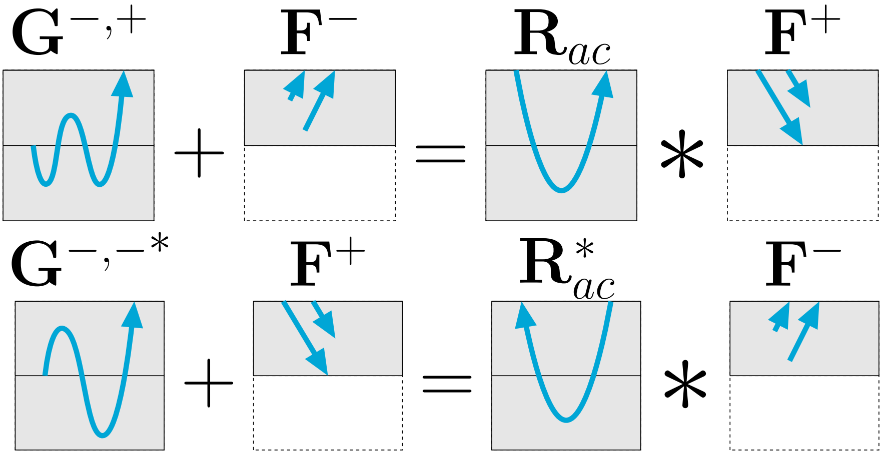

Figure B.2: Cartoon illustration of Equations B.7 and B.8. The different units are elaborated upon in Figure B.1.

where the subscript *ac* describes the reflection response of both units *a* and *c*. Second, using the same states and Equations B.2, B.6 and B.5:

$$\{\mathbf{G}^{-,-}(\mathbf{x}_R,\mathbf{x}',\omega)\}^* + \mathbf{F}^{+}(\mathbf{x}_R,\mathbf{x}',\omega) = \int_{\partial\mathbb{D}_0} \{\mathbf{R}_{ac}(\mathbf{x}_R,\mathbf{x},\omega)\}^* \mathbf{F}^{-}(\mathbf{x},\mathbf{x}',\omega)\,d\mathbf{x}. \tag{B.8}$$

These equations are graphically displayed in Figure B.2. Next, the following relations for the extrapolated focusing- (**V**) and Green's (**U**) functions are given:

$$\mathbf{V}^{\pm}(\mathbf{x}_R,\mathbf{x}'',\omega) = \int_{\partial\mathbb{D}_1} \mathbf{F}^{\pm}(\mathbf{x}_R,\mathbf{x}',\omega)\mathbf{T}_d(\mathbf{x}',\mathbf{x}'',\omega)\,d\mathbf{x}', \tag{B.9}$$

$$\mathbf{U}^{-,+}(\mathbf{x}_R,\mathbf{x}'',\omega) = \int_{\partial\mathbb{D}_1} \mathbf{G}^{-,+}(\mathbf{x}_R,\mathbf{x}',\omega)\mathbf{T}_d(\mathbf{x}',\mathbf{x}'',\omega)\,d\mathbf{x}', \tag{B.10}$$

and

$$\{\mathbf{U}^{-,-}(\mathbf{x}_R,\mathbf{x}'',\omega)\}^* = \int_{\partial\mathbb{D}_1} \{\mathbf{G}^{-,-}(\mathbf{x}_R,\mathbf{x}',\omega)\}^* \mathbf{T}_d(\mathbf{x}',\mathbf{x}'',\omega)\,d\mathbf{x}'. \tag{B.11}$$

Here, $\mathbf{x}''$ is a coordinate on $\partial\mathbb{D}_0$, and $\mathbf{T}_d$ is the direct arrival of the transmission response from $\partial\mathbb{D}_0$ to $\partial\mathbb{D}_1$. If these relations are applied to Equations B.7 and B.8, the extrapolated Green's function representations are found (van der Neut & Wapenaar, 2016):

$$\mathbf{U}^{-,+}(\mathbf{x}_R,\mathbf{x}'',\omega) + \mathbf{V}^{-}(\mathbf{x}_R,\mathbf{x}'',\omega) = \int_{\partial\mathbb{D}_0} \mathbf{R}_{ac}(\mathbf{x}_R,\mathbf{x},\omega)\mathbf{V}^{+}(\mathbf{x},\mathbf{x}'',\omega)\,d\mathbf{x}, \tag{B.12}$$

and

$$\{\mathbf{U}^{-,-}(\mathbf{x}_R,\mathbf{x}'',\omega)\}^* + \mathbf{V}^{+}(\mathbf{x}_R,\mathbf{x}'',\omega) = \int_{\partial\mathbb{D}_0} \{\mathbf{R}_{ac}(\mathbf{x}_R,x,\omega)\}^* \mathbf{V}^{-}(\mathbf{x},\mathbf{x}'',\omega)\,d\mathbf{x}. \tag{B.13}$$

Table B.2: States used in the derivation of underburden removal. State A is defined in the truncated medium, with a source at $\mathbf{x}_R$ just above $\partial\mathbb{D}_0$. State B is chosen in the truncated medium with focus $\mathbf{x}'$ at $\partial\mathbb{D}_1$.

(a) State A: Overburden only *a*

$\partial\mathbb{D}_0$	$\mathbf{p}_A^+(\mathbf{x},\omega) = \mathbf{I}\delta(\mathbf{x}_H - \mathbf{x}_{H,R})$ $\mathbf{p}_A^-(\mathbf{x},\omega) = \mathbf{R}_a(\mathbf{x},\mathbf{x}_R,\omega)$
$\partial\mathbb{D}_1$	$\mathbf{p}_A^+(\mathbf{x},\omega) = \mathbf{T}_a(\mathbf{x},\mathbf{x}_R,\omega)$ $\mathbf{p}_A^-(\mathbf{x},\omega) = 0$

(b) State B: Overburden only *a*

$\partial\mathbb{D}_0$	$\mathbf{p}_B^+(\mathbf{x},\omega) = \mathbf{F}^+(\mathbf{x},\mathbf{x}',\omega)$ $\mathbf{p}_B^-(\mathbf{x},\omega) = \mathbf{F}^-(\mathbf{x},\mathbf{x}',\omega)$
$\partial\mathbb{D}_1$	$\mathbf{p}_B^+(\mathbf{x},\omega) = \mathbf{I}\delta(\mathbf{x}_H - \mathbf{x}'_H)$ $\mathbf{p}_B^-(\mathbf{x},\omega) = 0$

Table B.3: States used in the derivation of overburden removal. State A is defined in the medium without overburden, with a source at $\mathbf{x}'$ just above $\partial\mathbb{D}_1$. State B is chosen in the actual medium with a source at $\mathbf{x}_R$ just above $\partial\mathbb{D}_0$. The states are evaluated between $\partial\mathbb{D}_1$ and $\partial\mathbb{D}_2$.

(a) State A: Underburden only *c*

$\partial\mathbb{D}_1$	$\mathbf{p}_A^+(\mathbf{x},\omega) = \mathbf{I}\delta(\mathbf{x}_H - \mathbf{x}'_H)$ $\mathbf{p}_A^-(\mathbf{x},\omega) = \mathbf{R}_c(\mathbf{x},\mathbf{x}',\omega)$
$\partial\mathbb{D}_2$	$\mathbf{p}_A^+(\mathbf{x},\omega) = \mathbf{T}_c(\mathbf{x},\mathbf{x}',\omega)$ $\mathbf{p}_A^-(\mathbf{x},\omega) = 0$

(b) State B: Full medium *ac*

$\partial\mathbb{D}_1$	$\mathbf{p}_B^+(\mathbf{x},\omega) = \mathbf{G}^{+,+}(\mathbf{x},\mathbf{x}_R,\omega)$ $\mathbf{p}_B^-(\mathbf{x},\omega) = \mathbf{G}^{-,+}(\mathbf{x},\mathbf{x}_R,\omega)$
$\partial\mathbb{D}_2$	$\mathbf{p}_B^+(\mathbf{x},\omega) = \mathbf{T}_{ac}(\mathbf{x},\mathbf{x}_R,\omega)$ $\mathbf{p}_B^-(\mathbf{x},\omega) = 0$

B.4. UNDER- AND OVERBURDEN REMOVAL

To find the representation for underburden removal, the focusing functions are once again considered. These functions are free of underburden interactions, because they are defined in the truncated medium. State B is, therefore, exactly the same as before. On the contrary, state A is now also defined in the truncated medium. Again, a source is chosen right above $\partial\mathbb{D}_0$, resulting in a downgoing wavefields $\mathbf{p}_A^+(\mathbf{x},\omega) = \mathbf{I}\delta(\mathbf{x}_H - \mathbf{x}_{H,R})$. However, the reflection response is only from unit *a*, hence $\mathbf{p}_A^-(\mathbf{x},\omega) = \mathbf{R}_a(\mathbf{x},\mathbf{x}_R,\omega)$. The wavefield at $\partial\mathbb{D}_1$ also differ, because no underburden is present. For this reason, the downgoing wavefield is simply the transmission response of the overburden $\mathbf{p}_A^+(\mathbf{x},\omega) = \mathbf{T}_a(\mathbf{x},\mathbf{x}_R,\omega)$, whereas there is no response from the transparent underburden $\mathbf{p}_A^-(\mathbf{x},\omega) = 0$. These states are shown in Table B.2, when combined with Equations B.1 and B.6, they give (Wapenaar & Staring, 2018):

$$\mathbf{F}^-(\mathbf{x}_R,\mathbf{x}',\omega) = \int_{\partial\mathbb{D}_0} \mathbf{F}^+(\mathbf{x},\mathbf{x}',\omega)\mathbf{R}_a(\mathbf{x}_R,\mathbf{x},\omega)\,d\mathbf{x}. \tag{B.14}$$

Note how $\mathbf{R}_a(\mathbf{x}_R,\mathbf{x},\omega)$ is the reflection response of the overburden only that can be extracted by a multi-dimensional convolution (MDD), hence the underburden has effectively been removed. This can again be rewritten to the extrapolated form using Equation B.9:

$$\mathbf{V}^-(\mathbf{x}_R,\mathbf{x}'',\omega) = \int_{\partial\mathbb{D}_0} \mathbf{V}^+(\mathbf{x},\mathbf{x}'',\omega)\mathbf{R}_a(\mathbf{x}_R,\mathbf{x},\omega)\,d\mathbf{x}. \tag{B.15}$$

Finally, the states in Table B.3 are used to acquire the equation for overburden removal. Note that the boundaries have shifted downwards, hence $\partial\mathbb{D}_i = \partial\mathbb{D}_1$ and $\partial\mathbb{D}_j = \partial\mathbb{D}_2$ are used in Equation B.1. On the one hand, state A only operates in the underburden, with a source just above the boundary $\partial\mathbb{D}_1$, giving $\mathbf{p}_A^+(\mathbf{x},\omega) = \mathbf{I}\delta(\mathbf{x}_H - \mathbf{x}'_H)$ and its reflection

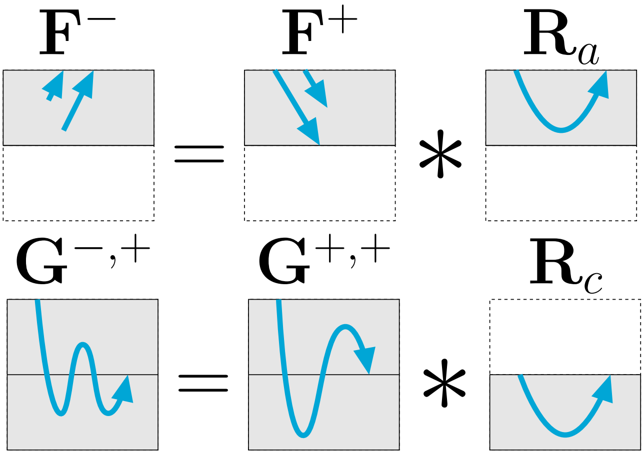

Figure B.3: Cartoon illustration of Equations B.14 and B.16. The different units are elaborated upon in Figure B.1.

response $\mathbf{p}_A^-(\mathbf{x},\omega) = \mathbf{R}_b(\mathbf{x},\mathbf{x}',\omega)$. Moreover, at the bottom boundary $\partial\mathbb{D}_2$ the downgoing field is the transmission response through the underburden $\mathbf{T}_b(\mathbf{x},\mathbf{x}',\omega)$. On the other hand, state B is defined in the full medium ac, with a source at the surface. Hence, at the top boundary $\partial\mathbb{D}_1$ the Green's functions define the up- and downgoing wavefields. The downgoing $\mathbf{p}_B^+(\mathbf{x},\omega)$ at $\partial\mathbb{D}_2$ is then equal to the transmission through the full medium $\mathbf{T}_{ab}(\mathbf{x},\mathbf{x}_R,\omega)$, whereas $\mathbf{p}_B^-(\mathbf{x},\omega) = 0$, because there are no reflections coming back due the transparent layers below $\partial\mathbb{D}_2$. Bringing it all together gives (Wapenaar et al., 2021):

$$\{\mathbf{G}^{-,+}(\mathbf{x}',\mathbf{x}_R,\omega)\}^t = \int_{\partial\mathbb{D}_1} \{\mathbf{G}^{+,+}(\mathbf{x},\mathbf{x}_R,\omega)\}^t \mathbf{R}_c(\mathbf{x},\mathbf{x}',\omega)\, d\mathbf{x}. \tag{B.16}$$

Using Equations B.5 and B.3 the form, that is used throughout the thesis, is found:

$$\mathbf{G}^{-,+}(\mathbf{x}_R,\mathbf{x}',\omega) = -\int_{\partial\mathbb{D}_1} \mathbf{G}^{-,-}(\mathbf{x}_R,\mathbf{x},\omega)\mathbf{R}_c(\mathbf{x},\mathbf{x}',\omega)\, d\mathbf{x}. \tag{B.17}$$

Here, $\mathbf{R}_c(\mathbf{x},\mathbf{x}',\omega)$ is the reflection response measured at $\partial\mathbb{D}_1$ free from overburden interactions. Again, this reflection response can be retrieved using a MDD of Equation B.17. Finally, the equation for the extrapolated Green's functions can be retrieved using Equations B.10 and B.11:

$$\mathbf{U}^{-,+}(\mathbf{x}_R,\mathbf{x}",\omega) = -\int_{\partial\mathbb{D}_0} \mathbf{U}^{-,-}(\mathbf{x}_R,\mathbf{x},\omega)\mathbf{R}_c(\mathbf{x},\mathbf{x}",\omega)\, d\mathbf{x}. \tag{B.18}$$

In this equation the coordinates of the reflection response have now moved to $\partial\mathbb{D}_0$. In Figure B.3, a cartoon representation of Equations B.14 and B.16. This figure shows how "injecting" $\mathbf{F}^+$ into $\mathbf{R}_a$ gives a reflection response $\mathbf{F}^-$ on the top row. On the bottom row, it is shown how $\mathbf{G}^{+,+}$ and $\mathbf{R_c}$ can be combined to retrieve $\mathbf{G}^{-,+}$. If one wants to instead find the reflection response of the over- or underburden, a MDD is required.

REFERENCES

Slob, E., Wapenaar, K., Broggini, F., & Snieder, R. (2014). Seismic reflector imaging using internal multiples with Marchenko-type equations. *Geophysics*, *79*(2), S63–S76. https://doi.org/10.1190/geo2013-0095.1

van der Neut, J., & Wapenaar, K. (2016). Adaptive overburden elimination with the multidimensional marchenko equation. *Geophysics*, *81*(5), T265–T284. https://doi.org/10.1190/geo2016-0024.1

Wapenaar, C., & Grimbergen, J. (1996). Reciprocity theorems for one-way wavefields. *Geophysical Journal International*, *127*(1), 169–177. https://doi.org/10.1111/j.1365-246X.1996.tb01542.x

Wapenaar, K., Brackenhoff, J., Dukalski, M., Meles, G., Reinicke, C., Slob, E., Staring, M., Thorbecke, J., van der Neut, J., & Zhang, L. (2021). Marchenko redatuming, imaging, and multiple elimination and their mutual relations. *Geophysics*, *86*(5), WC117–WC140. https://doi.org/10.1190/geo2020-0854.1

Wapenaar, K., & Staring, M. (2018). Marchenko-based target replacement, accounting for all orders of multiple reflections. *Journal of Geophysical Research: Solid Earth*, *123*(6), 4942–4964. https://doi.org/10.1029/2017JB015208

Wapenaar, K., Thorbecke, J., van der Neut, J., Broggini, F., Slob, E., & Snieder, R. (2014). Marchenko imaging. *Geophysics*, *79*(3), WA39–WA57. https://doi.org/10.1190/geo2013-0302.1

ACKNOWLEDGEMENTS

While this dissertation only bears a single name, without the generous support of many people it would instead have been a disastertation. In this chapter I would like to acknowledge everyone that in some way contributed to this final product.

First and foremost I would like to express my gratitude to my promotors Kees Wapenaar and Evert Slob. Kees, you are not very keen on being buried in praise, as I recently discovered during your valedictory address. It may, therefore, be better for you to not continue reading this paragraph. All joking aside, I am truly privileged to have been able to work with you, which, thanks to your humility, truly felt like I was working with rather than under someone. You never hesitated to let me ponder a problem by myself, but were also always there to steer me in the right direction, if something became too much for my simple mind to handle. This freedom has allowed me to thrive as an independent researcher and to develop essential critical thinking skills. Evert, even though we did not meet as often, you were always able to ask the right questions when we did. Your perspective was extremely valuable as it forced me to keep thinking outside of my isolated box. On top of that, it was always a pleasure to see you at the DOGS and social events to have some more lighthearted discussions.

Another person, who certainly deserves a great deal of gratitude, is Jan Thorbecke. Jan, many former PhD students have, rightfully so, lauded your prowess and assistance with computational problems, but they failed to mention your equally impressive icecream-eating skills. Thank you for always being available to discuss my programming- and Marchenko-related struggles, and making time for me even if there was no actual progress to report.

Hadi, I have to thank you for your endless patience. As someone with minimal experience in reservoir simulations, I managed to make every possible mistake. However, this didn't bother you in the slightest, and you always found time to explain where I went wrong or to refer me to right resource. I was a little worried I would scare you from working with geophysicists in the future, fortunately, I believe you found a new geophysics student already.

This list wouldn't be complete without mentioning the rest of the amazing Marchenko team at TU Delft. Joeri, I may never say it to your face, but it was an honor to work with you. Thank you for never hesitating to part with your knowledge in order to fast-track my PhD project. My taxi-driver and "favorite" German, Chris, who gracefully shared his codes with me, and was always available to discuss anything Marchenko. These discussions even continued when I should have been focusing on bouldering instead... Joost, you are an endless source of ideas, thank you for discussing some of them with me and convincing me of the strength of the extrapolated focusing functions. Thank you, Myrna for helping me with my first steps in the world of MDDs. I'm grateful for Giovanni and Lele, who took the time to explain Marchenko to the ignorant new guy. Last but not least, thanks to Aydin and Faezeh for experiencing the Marchenko struggle with me.

One of the nicest group of people in Delft is the ADMIRE team, who accepted a geophysicist as one of their own. Special thanks to Mousa, for taking the time to show me around the labyrinth that is DARSim code. Kishan, thank you for being a geomechanical genius, and helping me along. And all the other members, who made me feel very welcome and shared valuable insights in our weekly meetings: Fanxiang, Sara, Yuhang, Leila, Maartje, Willemijn, Herminio, Thejas, Debanjan, Artur, Mengjie and Ziliang.

Of course, not everyone can have the joy of working on the beauty that is Marchenko. However, the other staff at the AGP section still made a very positive contribution to my time at TU. First, I would like to express my gratitude to Guy, who introduced me to geophysics during my bachelor study. Next, thanks to Kees Weemstra, who, together with Arie and Elmer, supervised me in creating my first real contribution to the academic world. Erik, thank you for helping me with the Delphi codes and finding suitable field data. For your sake, I'm glad you joined the section when you did, as I would have taken up all your time if you came here earlier. Deyan, thank you for showing everyone chocolate is an acceptable lunch long before I joined. Anne, thank you for being the first to sign up for my pub-quizzes. And thanks to the other staff that make our group so pleasant: Auke, Gerrit, Läslo, Ranajit, Wim, Karl-Heinz, and Femke, as well as the secretary and support staff: Ralf, Marlijn, Lydia, Barbara, Liliana, Jens, Marc, Guus and Joost.

My main outlet for all the PhD stress were the with interactions my colleagues in the department. Florencia, well done on surviving almost 4 years of office-sharing with me. I'm sure we will stay friends for as long as you keep bringing me Argentinian snacks and candy. Thank you for being the second-best DOGS president during my 4 years. The best DOGS treasurer was without doubt Billy, who was always available for a beer. During my time at the DOGS I also had the pleasure of meeting Aukje. Thank you for always keeping me grounded as much as possible, by ridiculing my ice-skating skills and ridiculing Marchenko together with Jingming, Milad and Eddy. I'm also grateful for Musab, for allowing me an outing to Groningen, although I would recommend arranging better weather next time. As well as all the other PhD students and post-docs who made my time at TU not only bearable but even enjoyable: Entela, David, Maria, Menno, Marat, Dong, Sverre, Evgeniia, Camille, Hamed, Iban, Aleksei, Amin, Ilshat, Max, Nicolas, Jan-Willem, Pieter, Jianhuan, Karim, Yusuke, Ranjani, Mahmoud, Olivier, Chris, Dieter, Gil, Lisanne, Wen, Junhai, Shohei, Shahar and Siamak, and everyone else I'm undoubtedly forgetting. Moreover, I'm grateful for all the geology people and their cute, little pseudoscience (honestly, I'm just jealous you always got to be away on fieldwork): Rémi, Quinten, Tim, Stephan, Martha, Santosh, Akeel, Emilio, Andrea, Nazife, Eli, Jasper and Jasper.

Outside of the university hours I had a great group of friends to connect with the world outside of geophysics. My friends in Limburg and from the Rivierenlaan made sure I was able to unwind during this downtime. The most important side-business in life was covered by Squash Delft Heren 9, with whom I have won the third half many a time.

I wouldn't have been able to get where I am today without my family. Pap en mam, thanks for supporting me in whatever way possible and making sure I never had a thing to worry about. Sally, thank you for letting me boast about being supported internationally. Moana, thank you for cooking for me once. Finally, of course Billie, it hasn't always been easy, but I'm glad you stuck by me for all of these years. Thank you for stopping me from doing stupid things, and taking care of me when I inevitably did them anyway.

Curriculum Vitæ

Johno Egbart van IJsseldijk

14-01-1995	Born in Weert, the Netherlands.

Education & Experience

2007–2013	Secondary Education (VWO) Philips van Horne SG, Weert, the Netherlands
2013–2016	B.Sc. Applied Earth Sciences Delft University of Technology, the Netherlands
2015	Exchange Semester, Computer Science Minor University of Technology Sydney, Australia
2016–2018	M.Sc. Applied Geophysics Delft University of Technology, the Netherlands Eidgenössische Technische Hochschule, Zürich, Switzerland Rheinisch-Westfälische Technische Hochschule, Aachen, Germany
2018–2023	Ph.D. Applied Geophysics Delft University of Technology, the Netherlands *Thesis:* Time-lapse monitoring with virtual seismology *Promotors:* Prof. dr. ir. C.P.A. Wapenaar Prof. dr. ir. E.C. Slob
2023–Present	Acoustics & Sonar Scientist Netherlands Organisation for Applied Scientific Research (TNO)

PUBLICATIONS

LIST OF PUBLICATIONS

6. **J. van IJsseldijk**, J. Brackenhoff, J. Thorbecke & K. Wapenaar, *Time-lapse applications of the Marchenko method on the Troll field*, under review, preprint available on arXiv: 10.48550/arXiv.2303.10964 (2023).

5. **J. van IJsseldijk**, H. Hajibeygi & K. Wapenaar, *A framework for subsurface monitoring by integrating reservoir simulation with time-lapse seismic surveys*, Scientific Reports **13**, 13661 (2023).

4. **J. van IJsseldijk**, J. van der Neut, J. Thorbecke & K. Wapenaar, *Extracting small time-lapse traveltime changes in a reservoir using primaries and internal multiples after Marchenko-based target zone isolation*, Geophysics **88**, R135-R143 (2023).

3. **J. van IJsseldijk** & K. Wapenaar, *Adaptation of the iterative Marchenko scheme for imperfectly sampled data*, Geophysical Journal International **224**, 326-336 (2020).

2. K. Wapenaar & **J. van IJsseldijk**, *Discrete representations for Marchenko imaging of imperfectly sampled data*, Geophysics **85**, A1-A5 (2020).

1. **J. van IJsseldijk**, E. Ruigrok, A. Verdel & C. Weemstra, *Shallow crustal imaging using distant, high-magnitude earthquakes*, Geophysical Journal International **219**, 1082-1091 (2019).

LIST OF CONFERENCE ABSTRACTS

10. **J. van IJsseldijk** & K. Wapenaar, *The Marchenko method and its application to time-lapse monitoring*, SEG Workshop: Multiple approaches to time-lapse monitoring for carbonate reservoirs, Abu Dhabi, UAE, 2022.

9. **J. van IJsseldijk** & K. Wapenaar, *Discerning small time-lapse traveltime changes by isolating the seismic response of a reservoir using the Marchenko method*, First International Meeting for Applied Geoscience & Energy, 2021: 3449-3453.

8. M. Almobarak, **J. van IJsseldijk**, K. Wapenaar, *Plane-wave Marchenko imaging method: Field data application*, 82nd EAGE Annual Conference & Exhibition, 2021.

7. K. Wapenaar & **J. van IJsseldijk**, *Employing internal multiples in time-lapse seismic monitoring, using the Marchenko method*, 82nd EAGE Annual Conference & Exhibition, 2021.

6. J. Brackenhoff, **J. van IJsseldijk** & K. Wapenaar, *Data-driven internal multiple elimination applications using imperfectly sampled reflection data*, 82nd EAGE Annual Conference & Exhibition-Workshop Programme, 2021.

5. **J. van IJsseldijk** & K, Wapenaar, *Correcting for imperfectly sampled data in the iterative Marchenko scheme*, 82nd EAGE Annual Conference & Exhibition, 2021.

4. K. Wapenaar & **J. van IJsseldijk**, *Coda-wave interferometry and the Marchenko method*, EGU General Assembly 2020, Online, 4–8 May 2020, EGU2020-20123.
3. **J. van IJsseldijk**, A. Verdel, E. Ruigrok & C. Weemstra, *Shallow crustal imaging using distant, high-magnitude earthquakes*, AGU Fall Meeting Abstracts 2019, S13A-08.
2. **J. van IJsseldijk** & Kees Wapenaar, *Marchenko-based target replacement in laterally varying media*, AGU Fall Meeting 2019, DOI: 10.1002/essoar.10501883.1.
1. Kees Wapenaar & **J. van IJsseldijk**, *Representations for the Marchenko Method for imperfectly sampled data*, SEG Technical Program Expanded Abstracts 2019, 4545-4549.